

Methods for Structural Health Monitoring and Damage Detection of Civil
and Mechanical Systems

Saurabh S. Bisht

Thesis submitted to the faculty of the Virginia Polytechnic Institute and
State University in partial fulfillment of the requirements for the degree of

Master of Science In
Engineering Science and Mechanics

Dr. Mahendra P. Singh
Dr. Scott L. Hendricks
Dr. Muhammad R. Hajj

June, 16th 2005
Blacksburg, Virginia

Keywords: structural health monitoring, damage detection, wavelet
transform, Hilbert-Huang transform, parametric system identification,
flexibility method, rotational flexibility method

Methods for Structural Health Monitoring and Damage Detection of Civil and Mechanical Systems

Saurabh S. Bisht

ABSTRACT

In the field of structural engineering it is of vital importance that the condition of an aging structure is monitored to detect damages that could possibly lead to failure of the structure. Over the past few years various methods for monitoring the condition of structures have been proposed. With respect to civil and mechanical structures several methods make use of modal parameters such as, natural frequency, damping ratio and mode shapes. In the present work four methods for modal parameter estimation and two methods for damage detection have been evaluated for their application to multi degree of freedom structures. The methods evaluated for modal parameter estimation are: Wavelet transform, Hilbert-Huang transform, parametric system identification and peak picking. Through various numerical simulations the effectiveness of these methods is studied. It was found that the simple peak-picking method performed very well compared to the more involved methods as it was able to identify modal parameters accurately in all examples considered in this study. For the identification and locating the damage, herein the flexibility and the rotational flexibility approaches have been evaluated for damage detection. The approach based on the rotational flexibility is found to be more effective.

Acknowledgment

I would like to thank my adviser Dr. M. P. Singh, for his continued guidance, and support. Without his encouragement and material support it would not have been possible for me to explore the new areas that I came to know of during the course of my graduate studies. I would also like to thank Dr. S. L. Hendricks and Dr. M. Hajj for being on my graduate committee.

This research is supported by National Science Foundation through grant no. CMS- 0201475. This support is gratefully acknowledged. Any opinion, finding, and conclusions or recommendation expressed in this study are those of the writer and do not necessarily reflect the views of the National Science Foundation.

Also I would like to extend my thanks to my family and friends who were always there to support me in every possible way, without them this work would not have been a possible.

Contents

Abstract	ii
Acknowledgment	iii
List of Figures	vii
List of Tables	xi
1 Introduction	1
1.1 Structural Health Monitoring	1
1.2 Organization of the work	2
2 Wavelet Transform	5
2.1 Introduction	5
2.2 Wavelet transform	7
2.2.1 Admissibility condition for wavelets	11
2.2.2 Discrete Wavelet Transform and Orthogonal Discrete Wavelet Transform	11
2.3 Applications of wavelet transforms	14
2.3.1 Identifying evolving frequencies	14
2.3.2 Localizing events in time/space	16
2.3.3 Separating frequency components	19
2.4 Modal Parameter Identification	22
2.5 Numerical results for modal parameters	35
2.5.1 No-noise case	38
2.5.2 Noisy Data	39
2.6 Identifying damage instant	49
2.7 Summary and Conclusions	54

3	Empirical Mode Decomposition and Hilbert-Huang Transform	56
3.1	Introduction	56
3.2	EMD and HHT	56
3.2.1	Comparison to the DWT process	58
3.2.2	Advantage of the EMD process	58
3.2.3	The issue of closely spaced frequencies	59
3.2.4	Application to modal parameter estimation	59
3.2.5	Application to damage time detection	60
3.3	Conclusions	62
4	Parametric System Identification	64
4.1	Introduction	64
4.2	Linear Time Invariant Systems - ARMA Model	66
4.3	Parametric System Identification	70
4.3.1	Parametric models	70
4.3.2	Estimation of parameters	72
4.4	Identification of Modal Quantities	73
4.5	Numerical results	74
4.5.1	No-noise	74
4.5.2	Noisy data	76
4.6	Conclusions	84
5	Peak Picking Method	86
5.1	Introduction	86
5.2	Fourier Transform and The Peak Picking Method	87
5.3	Numerical Results	91
5.4	Conclusions	97
6	Damage Detection	102
6.1	Introduction	102
6.2	Flexibility approach	103
6.3	Rotational flexibility approach	106
6.4	Numerical results	108
6.5	Conclusions	114

7	Summary and Concluding Remarks	117
7.1	Summary	117
7.2	Future Studies	120

List of Figures

2.1	Time domain function and its corresponding DFT for different values of scale.	8
2.2	Identifying frequency evolution by wavelet transform	15
2.3	Time/space localization using WT	17
2.4	Plot of absolute value of the CWT coefficients for the sum of two sines	20
2.5	Plots for the sum of two sines, (a) contour value of the CWT coefficients, (b) $\log(\text{abs}(\text{CWT coefficients at } a = 15))$ - time plot (c) $\text{phase}(\text{CWT coefficients at } a = 15)$ -time plot	21
2.6	Floor 1 impulse response acceleration for the 3-DOF structure	23
2.7	Plot of absolute values of the CWT coefficients for the floor 1 impulse response acceleration for the 3-DOF structure	24
2.8	Plot of absolute values of the CWT coefficients for the floor 1 impulse response acceleration for the 3-DOF structure at the three scale values corresponding to the three modes	25
2.9	Real part of the complex Morlet wavelet and its DFT for $f_c=5\text{Hz}$, $f_b= 1\text{Hz}$ and three different scale values	28
2.10	Absolute value of CWT coefficients contour plots for different f_c showing the separation of modal responses for the 3-dof structure.	30
2.11	$\log(\text{Abs}(\text{CWT coeff}))$ - <i>time</i> plot for the three modes of the 3-dof structure for two different f_c	31
2.12	Real part of the complex Morlet wavelet and its DFT for $f_c = 5 \text{ Hz}$ and three different f_b values	32
2.13	$\log(\text{Abs}(\text{CWT coeff}))$ - <i>time</i> plot for the three modes of the 3-dof structure for two different f_b	33
2.14	$\log(\text{Abs}(\text{CWT coeff}))$ - <i>time</i> plot for the three modes of the 3-dof structure for two different f_b	34

2.15	The ASCE-SHM benchmark structure	36
2.16	Actual and identified mode shapes for 3DOF 2% nominal damping	40
2.17	Actual and identified mode shapes for 3DOF 5% nominal damping	41
2.18	Actual and identified mode shapes for 3DOF 10% nominal damping	42
2.19	Actual and identified mode shapes for 6DOF 2% nominal damping	44
2.20	Actual and identified mode shapes for 6DOF 5% nominal damping	45
2.21	Actual and identified mode shapes for 6DOF 10% nominal damping	47
2.22	Actual and identified mode shapes for the benchmark structure	48
2.23	Effect of noise on the phase plot	50
2.24	$\log(Abs(CWT\ coeff))$ - <i>time</i> plot for floor 1 mode 1, 6-dof 2%damping, SNR = 20dB	51
2.25	$\log(Abs(CWT\ coeff))$ - <i>time</i> plot for floor 1 mode 2, 6-dof 2%damping, SNR = 20dB	52
2.26	$\log(Abs(CWT\ coeff))$ - <i>time</i> plot for floor 1 mode 3, 6-dof 2%damping, SNR = 20dB	53
2.27	Floor acceleration data and the level 1 details using the <i>DB3</i> wavelet, for the benchmark structure	54
3.1	A simple signal and its first IMF	61
3.2	Damage detection for the benchmark structure using EMD method.	63
4.1	Actual and identified mode shapes from the 6-DOF system, 10% nominal damping, using ARMA(13,12) model. \circ - actual values	75
4.2	Pole-zero plot for the ARX model fitted to the acceleration response at floor 1. The numbers in the bracket show the natural frequency (in rad/sec) and damping ratio corresponding to each pole.	77
4.3	Pole-zero plot for the ARX model fitted to the noisy acceleration response at floor 1 (model order 13,13), along with the actual poles and zeros as identified from the no-noise case. . .	78

4.4	Pole-zero plot for the ARX model fitted to the noisy acceleration response at floor 1 (model order 40,40), along with the actual poles and zeros as identified from the no-noise case. . .	79
4.5	The identified natural frequencies as a function of model order for the case of 6-DOF, 5% nominal damping, with 20dB noise.	85
5.1	First floor absolute acceleration response and its periodogram for the 6-DOF, 2% nominal damping structure.	89
5.2	First floor impulse response and its periodogram for the 6-DOF, 2% nominal damping structure.	90
5.3	Actual and identified mode shapes for the 6-DOF 2% nominal damping structure, no-noise.	92
5.4	First floor impulse response and its periodogram for the 6-DOF, 10% nominal damping structure, no-noise.	94
5.5	Actual and identified mode shapes for the 6-DOF 10% nominal damping structure, no-noise.	95
5.6	(a) First floor noisy impulse response for the 6-DOF structure, 2% nominal damping, 20dB noise and its (b) periodogram . .	96
5.7	First four actual and identified mode shapes for the 6-DOF structure, 2% nominal damping, 20dB noise	97
5.8	(a) 1024 data points of the first floor acceleration response for the ASCE SHM benchmark structure and its (b) periodogram	99
5.9	(a) First floor acceleration response for the ASCE SHM benchmark structure and its (b) averaged periodogram	100
5.10	Actual and identified mode shapes for the benchmark structure with 10% noise	101
6.1	Frobenius norm for the flexibility matrix estimated using different number of modes for the 12-DOF ASCE SHM benchmark structure	105
6.2	Frobenius norm for the rotational flexibility matrix estimated using different number of modes for the 12-DOF ASCE SHM benchmark structure	109
6.3	Damage detection using the flexibility matrix approach with normalized mode shapes for the 6-DOF structure	110
6.4	Damage detection using the flexibility matrix approach with non-normalized mode shapes for the 6-DOF structure	111

- 6.5 Damage detection using the rotational flexibility matrix approach with normalized mode shapes for the 6-DOF structure 112
- 6.6 Damage detection using the rotational flexibility matrix approach with non-normalized mode shapes for the 6-DOF structure 113
- 6.7 Damage detection using the rotational flexibility matrix approach for the ASCE benchmark structure, damage in one story.114
- 6.8 Damage detection using the rotational flexibility matrix approach for the ASCE benchmark structure, damage in two stories. 115

List of Tables

2.1	Modal properties of the 3-DOF model	35
2.2	Modal properties of the 6-DOF model	35
2.3	Modal properties for the translational y-direction of the benchmark structure	37
2.4	Percent error in natural frequency and damping obtained from the response of different floors for 3-DOF structure 2% nominal damping	39
2.5	Percent error in natural frequency and damping obtained from the response of different floors for 3-DOF structure 5% nominal damping	39
2.6	Percent error in natural frequency and damping obtained from the response of different floors for 3-DOF structure 10% nominal damping	40
2.7	Percent error in natural frequency and damping obtained from the response of different floors for 6-DOF structure 2% nominal damping	43
2.8	Percent error in natural frequency and damping obtained from the response of different floors for 6-DOF structure 5% nominal damping	43
2.9	Percent error in natural frequency and damping obtained from the response of different floors for 6-DOF structure 10% nominal damping	46
2.10	Percent error in natural frequency and damping obtained from the response of different floors for the benchmark structure 2% nominal damping	46
2.11	Percent error in natural frequency and damping obtained from the response of different floors for the benchmark structure 5% nominal damping	48

4.1	Parameters from ARMA(13,12) model for the case of no noisy	81
4.2	Parameters from ARMA(13,12) model for noisy data	81
4.3	Parameters from ARMA(26,25) model for noisy data	81
4.4	Parameters from ARMA(39,38) model for noisy data	81
4.5	Parameters from ARMA(52,51) model for noisy data	82
4.6	Parameters from ARMA(65,64) model for noisy data	82
4.7	Parameters from ARMA(78,77) model for noisy data	83
5.1	Actual mode shapes for the 6-DOF structure	91
5.2	Identified mode shapes for the 6-DOF structure, with 2% nominal damping, no-noise	93
5.3	Identified mode shapes for the 6-DOF structure, with 10% nominal damping, no-noise	93
5.4	Identified mode shapes for the 6-DOF structure, with 2% nominal damping, 20dB noise	98
5.5	Actual translational mode shapes for the ASCE SHM benchmark structure	98
5.6	Identified mode shape for the ASCE SHM benchmark structure	98

Chapter 1

Introduction

1.1 Structural Health Monitoring

In the field of civil engineering all design codes enforce the use of safety factors and various analysis and design procedures to make sure that a built structure is safe and lasts for the desired design period, and during its life serves the purpose it is designed for. During their design life the built structures may experience extreme loading conditions, like earthquakes, strong winds etc. They may be able to withstand them, suffering minor damages or, in the worst case, collapse. Even if a structure manages to withstand the loading it becomes crucial to examine its strength and load carrying capabilities to make sure no substantial damages have occurred. On the other hand, even if a structure is not exposed to extreme loads, it is desirable to monitor its condition as inevitable deterioration can weaken it over the years, which if unnoticed can grow into a major problem. Thus structures, especially important structures, need continuous monitoring and evaluation on a regular basis, with repairs and rehabilitation made as and when they become necessary.

This approach of monitoring the condition of a structure has recently been called structural health monitoring (SHM). SHM is, however, not a new concept, as important structures have always been routinely inspected, usually manually, for damages and their effect on the structural performance. But in recent years several research studies have been performed to improve the accuracy and reliability of this approach. Traditionally structural inspec-

tions, usually consisting of visual inspections, were carried out by trained or experienced individuals. In some special cases more advanced nondestructive methods such as eddy current, ultra sound, and other wave propagation based methods have also been used. The effectiveness of such inspections depends upon the accessibility of the structural location to be examined and to a large extent on the expertise of the individual conducting such inspections. Such approaches tend to be highly labor intensive and costly. Therefore, alternative methods that can automatically collect and analyze structural data to ascertain its condition have been sought by practitioners and the research community. In such approaches one usually collects vibration data of the structure caused by natural forces such wind, traffic, earthquakes, etc. This data is then analyzed to identify the damage in the structure, if any. Among other method that use the vibration data, the modal analysis-based methods have attracted special attention.

A complete SHM approach consists of four basic steps which are required to be resolved sequentially. These four basic steps involve : (1) identification of damage occurrence in the structure, if any, (2) identification of single or multiple damage locations, (3) quantification of the level of damage, and (4) evaluation of structural performance and its useful remaining life. The idea is to do this reliably and continuously, if possible, in a cost efficient manner. This study is concerned with the first three steps of SHM, focusing on damage detection using modal properties.

1.2 Organization of the work

In general all SHM approaches require measurement of certain response quantities which are processed to calculate important parameters which, in turn, are used to predict the present state of the structure. The parameters that are most commonly used in popular SHM and damage detection approaches are the modal frequencies, damping ratios and mode shapes. In this study, the effectiveness of four different methods that can be used to estimate the modal parameters and two related approaches which have been used to detect damage using modal parameters have been evaluated. The mode parameter estimation methods that have been examined are: (1) Wavelet Transform approach, (2) Empirical Mode Decomposition and Hilbert Huang Transform approach, (3) Parametric System Identification approach, and (4) the Peak

Picking approach. These four approaches are described in the next four chapters of this thesis. These chapters are followed by a chapter on damage detection wherein two related approaches one based on system flexibility and the other based on the rotational flexibility matrix formation have been examined. All the methods are tested through simulations on several multi degree of freedom (MDOF) structures. A more detailed description of the contents of the remaining chapters in this thesis is as follows:

Chapter 2: Wavelet Transform

This chapter deals with the method of wavelet transforms (WT), in particular the continuous wavelet transform (CWT) for modal parameter estimation. It is shown that the CWT can indeed be used to estimate natural frequencies, damping ratios and mode shapes for a MDOF system. Parameters of the WT affecting the estimated values are identified and their effect is illustrated. The discrete wavelet transform (DWT) is studied for its use in detecting the time occurrence of damage.

Chapter 3: Hilbert Huang transform:

This is a relatively new technique which has been proposed for non linear and non stationary time series analysis. It has been used for extracting modal parameters and detecting damage instants by several authors. This technique is briefly reviewed in this chapter, however, there were certain issues because of which this technique could not be used effectively for modal parameter estimation.

Chapter 4: Parametric System Identification:

In this chapter the technique of parametric system identification for modal analysis is studied. The use of parametric models had been proposed a long time back. In the chapter the theory of this method is reviewed and its use under various scenarios is examined.

Chapter 5 :Peak Picking Method:

The peak picking method, one of the earliest, and perhaps, simplest approach, is described in Chapter 5. The basic theory behind the method is reviewed and through simulations it is shown that in fact it can be effectively used for all the simulation cases studied in this work.

Chapter 6: Damage Detection:

This chapter is concerned with the detection and location of the damage using the calculated modal parameters. The methods based on flexibility and rotational flexibility matrices are described and evaluated through several numerical examples.

Chapter 7: Summary and Concluding Remarks

In this final chapter the major conclusions drawn from this study are provided and the future areas of research that can be explored are identified.

Chapter 2

Wavelet Transform

2.1 Introduction

The previous decade has seen significant developments in the field of wavelet transform (WT). Today its applications range from signal processing to image compression, from denoising to matrix multiplication etc. In this work we are mainly concerned with the signal analyzing property of WT, and primarily its ability to extract modal parameters (natural frequency, damping ratio and mode shapes) of a multi degree of freedom (MDOF) system. The theoretical background, illustrative examples, and simulation results, presented here are thus mainly related to this particular application of wavelets.

By decomposing the signal in the time-scale plane, WT provides a bridge between the time domain and the frequency domain representation of signals. Scale is a nondimensional parameter inversely proportional to the frequency in the signal. Traditionally, the data that was collected could either be represented in the time (or space etc.) domain, or in the frequency domain by the use of Fourier series, or the discrete Fourier transform (DFT). For many purposes these representations are enough. But there are applications when one would like to go beyond the Fourier analysis. For example, the DFT plot of a signal which comprises of several sinusoidal components would identify the frequencies of the sinusoids correctly but would not give any information of the individual components stretch in time. This information, however, can be obtained using the time-frequency representation of the signal.

Steps towards the time-frequency representation of signals had already been taken before the development of WT, for example through the short time Fourier Transform (STFT). WT allows more flexibility in the analysis and overcomes the limitations of the previously developed methods in various respects.

One main characteristic that sets the WT apart from other time-frequency localization methods is its adaptive nature. It breaks a signal into different frequency bands, the bandwidth of which depends on the frequency. For high frequencies WT provides large bandwidths and good time localization, and for smaller frequencies it uses a smaller bandwidth with better frequency localization. It will be shown later that this type of analysis is desired in many applications.

The subject of WT spreads over many disciplines. This chapter presents a limited overview of the theory of wavelet analysis, which is needed to understand its potential in the field of structural health monitoring (SHM) and damage detection. The overview of WT presented here is a very simplified version of the actual underlying theory. Most of the mathematical concepts behind WT are not mentioned. For continuous wavelet transform (CWT) the emphasis is on the good time-frequency localization issue. Discrete wavelet transform (DWT) is mentioned very briefly just for the sake of completeness.

Currently several well known texts (Daubechies, 1992; Strang and Nguyen, 1996; Poularikas, 1996) are available on the theoretical foundation of wavelets. In particular the handbook by Addison and Addison (2002) provides an overview of the application of WT to the fields of engineering, medicine, finance, etc, and the book by Percival and Walden (2000) its application to time series analysis. For numerical calculations, MATLAB¹ includes the Wavelet toolbox (Misiti). This toolbox has been used for numerical calculations made in this study.

¹MATLAB is a registered trademark of The MathWorks Inc.

2.2 Wavelet transform

The wavelet transform of a signal $x(t)$ is expressed as (Daubechies, 1992)

$$C(a, b) = \int x(t)\psi_{a,b}(t)dt \quad (2.1)$$

where $\psi_{a,b}(t)$ is defined as,

$$\psi_{a,b}(t) = \frac{1}{\sqrt{a}}\psi\left(\frac{t-b}{a}\right) \quad (2.2)$$

In Eq. 2.1 $C(a, b)$ are the wavelet coefficients. $\psi(\cdot)$ is known as the mother wavelet, and $\psi_{a,b}(\cdot)$ is its stretched and translated version with a and b as its scale and translational parameters. The wavelet coefficients are functions of these two parameters, and thus the WT of a one-dimensional signal is a two dimensional function.

To study a signal using the WT one chooses an appropriate mother wavelet for the analysis, say $\psi(t)$. Unlike the *sine* and *cosine* functions, all wavelet functions are non-zero only over a finite interval of time. To analyze the whole duration of the signal the wavelet function is therefore translated by varying the parameter b , resulting in $\psi(t-b)$. On the other hand, changing the parameter a changes the frequency domain (and also the time domain) characteristics of the wavelet function, resulting in the signal being analyzed at different frequencies. Thus, by varying the parameters a and b the signal is analyzed at different frequencies over its entire duration. The parameter b corresponds to time whereas the scale parameter a is inversely related to frequency.

To demonstrate how the scale parameter leads to this adaptive nature of the WT with respect to time-frequency localization, we consider the example of a real wavelet function defined as follows:

$$\psi(t) = \frac{2}{\sqrt{3\pi^{\frac{1}{4}}}} e^{-\frac{t^2}{2}}(1-t^2) \quad (2.3)$$

This wavelet function is commonly known as the Mexican hat wavelet. Using this mother wavelet one can construct other wavelet functions $\psi(t/a)$ using different values of the scale parameter a . Figure 2.1 shows three different time domain signals $\psi(t/a)$ and their corresponding DFT for $a=0.25$,

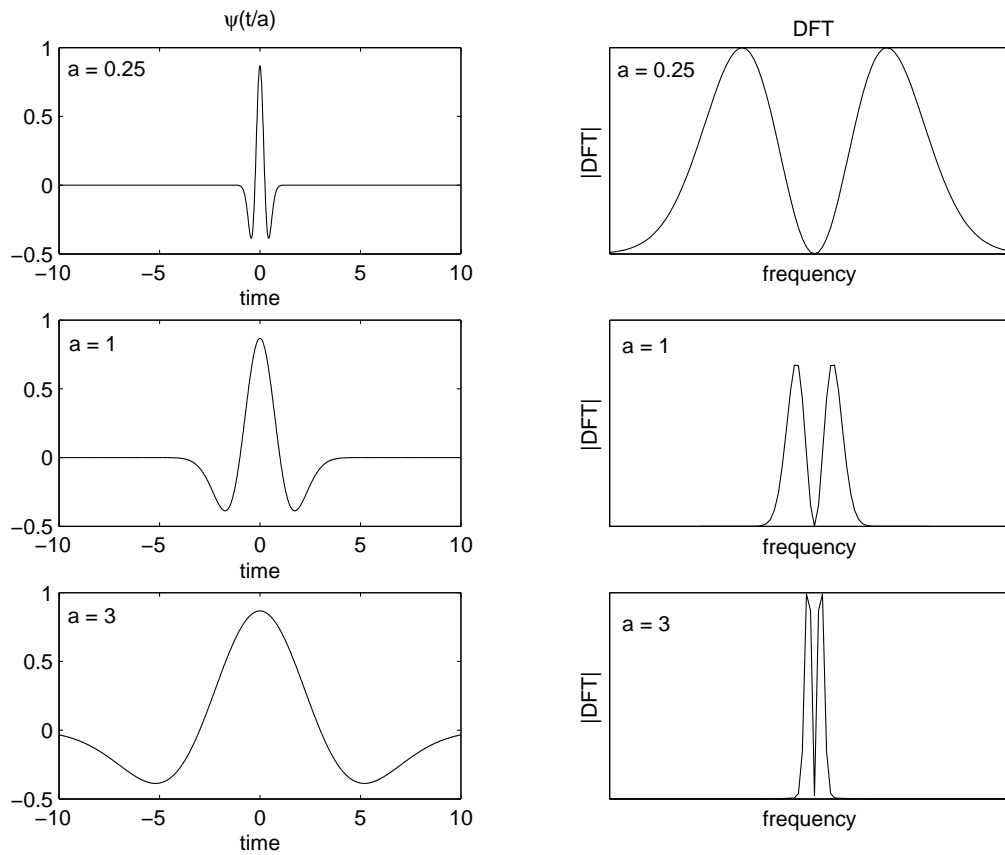


Figure 2.1: Time domain function and its corresponding DFT for different values of scale.

1, and 3. It can be seen that the time domain signals are non-zero only over a finite length of time. The DFT plot in the figure is a two-sided plot. This figure illustrate an important feature related to wavelet analysis.

Thus in a wavelet analysis *dilation in time domain* corresponds to a *contraction in frequency domain*, and this can be controlled by the scale parameter. In the figure it can be seen that as the scale value is increased, $\psi(\cdot)$ is stretched (or dilated) in the time domain and simultaneously its spectrum in the frequency domain moves towards lower frequencies with narrower frequency band.

This feature can also be seen mathematically by examining the Fourier transform of the mother wavelet and its dilated form as follows. Let $\Psi(\omega)$ be the Fourier transform of $\psi(t)$,

$$\Psi(\omega) = \int_{-\infty}^{\infty} \psi(t) e^{j\omega t} dt \quad (2.4)$$

then the Fourier transform of $\psi(\frac{t}{a})$ denoted by $\Psi_a(\omega)$ can be expressed as,

$$\Psi_a(\omega) = \int_{-\infty}^{\infty} \psi(t/a) e^{j\omega t} dt = a \int_{-\infty}^{\infty} \psi(t) e^{ja\omega t} dt = a\Psi(a\omega) \quad (2.5)$$

where a change of variable is used to arrive at the final result.

A good time resolution at low scales and good frequency resolution at large scales can also be expressed in terms of the bandwidths of the band-pass filters that are represented by the wavelets. The Fourier transform of a wavelet function defines this band-pass filter. The bandwidth of this filter defines the level of frequency localization provided by the filter. This bandwidth can be expressed in terms of $\Delta\omega$ as follows:

$$\Delta\omega^2 = \frac{\int_{-\infty}^{\infty} \omega^2 |\Psi(\omega)|^2 d\omega}{\int_{-\infty}^{\infty} |\Psi(\omega)|^2 d\omega} \quad (2.6)$$

Similarly, the bandwidth of a wavelet with scale parameter a can be expressed as,

$$\Delta\omega_a^2 = \frac{\int_{-\infty}^{\infty} \omega^2 |\Psi_a(\omega)|^2 d\omega}{\int_{-\infty}^{\infty} |\Psi_a(\omega)|^2 d\omega} = \frac{\int_{-\infty}^{\infty} \omega^2 |\Psi(a\omega)|^2 d\omega}{\int_{-\infty}^{\infty} |\Psi(a\omega)|^2 d\omega} = \frac{\Delta\omega^2}{a^2} \quad (2.7)$$

where Eq. 2.5 has been used to express $\Psi_a(\omega)$ in terms of $\Psi(\omega)$. This clearly shows that at low scales we get a wider frequency bandwidth (and a narrower time window), whereas at large scales we get narrower frequency bands (with wider time windows).

If the three wavelet functions shown in Figure 2.1 are available, one would use the function with $a=0.25$ to capture the local features of a signal. The reason being this function has the most compact support in the time domain

(non-zero in the smallest region). When the signal is convolved with this function it will be able to pick out local features better than the other two. However if the wavelet function with $a=3$ is convolved with the signal, the wavelet being non-zero over a larger time period will capture global details (relative to the $a=0.25$ function).

This can be understood with the analogy of the scale parameter to the commonly used term ‘scale’ as related to maps. A map drawn with a smaller scale will reveal more details than a map drawn with a larger scale, which will in a way give the global picture. Also, more paper will have to be used to represent a fixed area of land using a smaller scale. Similarly a wavelet function with a smaller scale value will have to be translated more to cover the same signal.

The above discussion shows how the WT approach differs from the Fourier transform approach. In Fourier transform approach, one uses the *sine* and *cosine* functions as the bases which extend throughout the time axis and provide no localization of frequency content (in the time domain) for the signal, whereas in WT approach the bases can be adjusted to capture both the time and frequency localization. Methods like the STFT have also been used to capture the variations of the frequency content of a signal with time, but this approach still uses a constant bandwidth to analyze the signal at all frequencies. In WT approach, the basis functions are at the disposal of the users, that is, a user can select the most appropriate function to suit the application. These features of the WT make them most suited for the analysis of non-stationary signals.

Though wavelet analysis allows for the tuning of time-frequency resolution, the resolution is limited by the Heisenberg uncertainty principle stated mathematically as follows:

$$\Delta t \Delta \omega \geq \frac{1}{2} \quad (2.8)$$

This means that one cannot pin-point the location of a signal in the time-frequency plane. All that one can get is a frequency band.

2.2.1 Admissibility condition for wavelets

Irrespective of the type of WT the wavelet function $\psi(t)$ must satisfy two basic properties,

1. The wavelet must be oscillating with a zero mean,

$$\int \psi(t)dt = 0$$

Put in the frequency domain it means that the zero frequency component of the frequency response $\Psi(\omega)$ of the wavelet must be zero.

$$\Psi(\omega = 0) = 0$$

Hence the wavelets act as band-pass filters in the frequency domain.

2. In order to be able to reconstruct the function from its WT the following condition must also be satisfied,

$$C_\psi = \int \frac{|\Psi(\omega)|^2}{\omega} d\omega < \infty$$

The above two are the basic requirements which any function must satisfy to qualify as a wavelet function. Such functions may be used for the CWT. But the CWT is a redundant representation (wavelet coefficients are calculated at all scales for all translation values). In order to reduce the redundancy more conditions are imposed which then lead to the discrete wavelet transform (DWT) and the orthogonal discrete wavelet transform (ODWT). These two related transforms are briefly discussed in the following.

2.2.2 Discrete Wavelet Transform and Orthogonal Discrete Wavelet Transform

In the previous section some elements of the CWT were described. In the continuous transform, the wavelet coefficients are calculated at scale values that vary continuously. This is desirable in certain situations, but it gives a very redundant representation of the signal. In DWT the coefficients are calculated only at discrete points. The scale parameter is varied as $a = a_0^m$ and the translation parameter as $b = nb_0a_0^m$, where $a_0 > 1$, $b_0 > 0$ and m ,

$n \in \mathbf{Z}$. That is, the translation and scale parameters are assigned discrete values. Substituting in Eq. 2.1, one obtains:

$$C(m, n) = a_0^{-\frac{m}{2}} \int x(t) \psi(a_0^{-m} t - nb_0) dt \quad (2.9)$$

For the particular choice of these parameters $a_0 = 2$ and $b_0 = 1$ one can obtain the orthonormal version of the DWT.

Herein only few basic concepts pertaining to the DWT are presented. Suppose there are two filters, a low-pass filter and a high-pass filter characterized by the filter coefficients $l(n)$ and $h(n)$ respectively. Corresponding to these filters one can define two time domain functions as,

$$\phi(n) = \sum_k l(k) \phi(2n - k) \quad (2.10)$$

and

$$\psi(n) = \sum_k h(k) \phi(2n - k) \quad (2.11)$$

The functions $\phi(n)$ and $\psi(n)$ are called the scaling and the wavelet function respectively. These functions can be translated and dilated to form a set of orthonormal scaling and wavelet basis functions,

$$\phi_{i,k}(n) = 2^{-\frac{i}{2}} \phi(2^{-i}n - k) \quad (2.12)$$

$$\psi_{i,k}(n) = 2^{-\frac{i}{2}} \psi(2^{-i}n - k) \quad (2.13)$$

To ensure that the functions given by Eq. 2.12 and Eq. 2.13 form an orthogonal basis for the set of functions with finite energy, some other criteria must also be satisfied, which can be reduced to certain conditions on the discrete filters (of length $N+1$) (Strang and Nguyen, 1996),

$$\sum_{n=0}^N l(n) l(n - 2k) = \delta(k) \quad (2.14)$$

$$\sum_{n=0}^N h(n) h(n - 2k) = \delta(k) \quad (2.15)$$

$$\sum_{n=0}^N l(n) h(n - 2k) = 0 \quad (2.16)$$

$$k = 0, 1, \dots, \frac{N-1}{2}$$

Any signal $x(n)$ is decomposed using these scaling and wavelet functions as

$$x = A_1 + D_1 = \sum_n a_1(n)\phi_{1,n} + \sum_n d_1(n)\psi_{1,n} \quad (2.17)$$

Using the orthogonality property of the discrete filters Eq. 2.14 (Strang and Nguyen, 1996), it can be shown that

$$a_1(k) = 2^{-\frac{1}{2}} \sum_n l(n - 2k)x(n) \quad (2.18)$$

$$d_1(k) = 2^{-\frac{1}{2}} \sum_n h(n - 2k)x(n) \quad (2.19)$$

Therefore $a_1(\cdot)$ and $d_1(\cdot)$ are obtained by convolving $x(\cdot)$ with $l(\cdot)$ and $h(\cdot)$ respectively and downsampling the obtained sequence.

In Eq. 2.17 the first part A_1 is the projection of the function onto the space spanned by the scaling function orthonormal basis $(\phi_{1,k})$, similarly the second part D_1 is the projection on the space spanned by the wavelet function orthonormal basis $(\psi_{1,k})$. These are respectively called the first level approximation and first level details of the function x .

Using the frequency domain definition of the low pass and the high pass filters corresponding to the scaling and wavelet functions, it is seen that the approximation A_1 is a smoothed version of the given function x and is obtained by passing the function through a low pass filter (with coefficients $l(\cdot)$). The detail D_1 can similarly be seen as either the difference between the original function x and the approximation A_1 or simply as the high frequency content of the function x obtained by filtering the function x through a high pass filter (with coefficients $h(\cdot)$).

Once A_1 is obtained the process of decomposition can be carried out on it to obtain A_2 and D_2 . Where A_2 and D_2 would be the second level approximation and the second level detail. These are obtained from A_1 in a similar fashion as A_1 and D_1 were obtained from x . This process can be repeated again on A_2 and so on. At each level the approximation contains the lower frequencies and is a smoothed version of the previous approximation and the detail contains the higher frequencies. Therefore as the decomposition is carried out higher frequencies are subsequently removed, and smoother

versions of the signal are obtained.

This is a rather simple description of the DWT. More can be found in (Strang and Nguyen, 1996).

2.3 Applications of wavelet transforms

As noted at the beginning of the chapter, WT has numerous applications. In this section few applications of WT that are of direct relevance in structural health monitoring and system identification are presented with the help of simple examples.

2.3.1 Identifying evolving frequencies

A useful application of wavelet analysis is to identify changes in the frequency of a signal as the time evolves. To show this we consider a chirp signal, with frequency increasing from an initial value of 0.5Hz to 20Hz. The signal was generated at 1024 data points. In addition to this evolving frequency, a discontinuity is introduced in the signal by setting its value equal to zero at the data point 512. This signal is shown in the upper left plot of Figure 2.2.

The upper right plot shows the DFT of the signal. It indicates that the signal has frequencies between 0.5 Hz and 20 Hz, but does not give any indication of their evolution and neither the presence of the discontinuity.

The lower left plot is the contour plot of the CWT wavelet coefficients of the signal. The CWT was calculated using the complex Morlet wavelet. This wavelet has been commonly used in modal parameter identification, and is defined as follows,

$$\psi(t) = \frac{1}{\sqrt{\pi f_b}} e^{2j\pi f_c t} e^{-\frac{t^2}{f_b}} \quad (2.20)$$

This wavelet has two adjustable parameters, f_c and f_b known as the central frequency and the bandwidth of the Morlet wavelet.

In this plot and other similar ones, the dark color (black) indicates large coefficient values, whereas light color (white) denotes low or zero coefficient values. In the plot it can be seen that as one moves from left to right i.e.

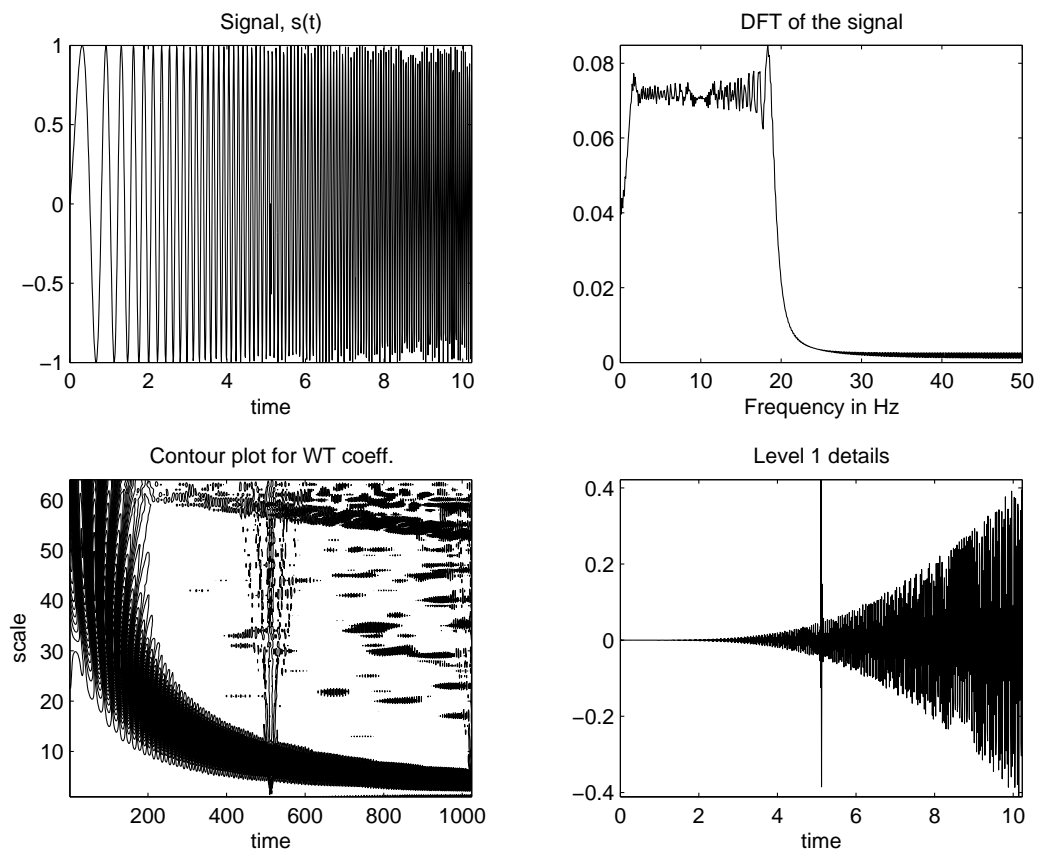


Figure 2.2: Identifying frequency evolution by wavelet transform

as time increases the scale values decrease, thus showing that the signal has increasing frequency. Also the discontinuity round data point 512 can be identified by the presence of large coefficient values round this data point at lower scales. The first level DWT details, obtained using the Daubechies wavelet (DB) filter (Strang and Nguyen, 1996) are shown in the bottom right plot. This plot also emphasizes two characteristics of the signal. First, the signal has higher frequency component towards the end (signal has increasing frequency), and there is some discontinuity round data point 512.

2.3.2 Localizing events in time/space

The time-frequency localization capability of WT has direct application in the time or space localization of events. It can be utilized in identifying sudden changes in a signal, breakdown points, discontinuity in higher derivatives, etc. With respect to structural health monitoring, this property of wavelets can be used in identifying the time of occurrence or the spatial location of a damage.

To show this by an example, a sine wave signal, $s(t)$, with a frequency of 0.5 Hz amplitude 1, with 1024 data points is generated. Another identical signal, $sd(t)$, is formed which is similar to $s(t)$ except that at data point 512 its value is 0.02 less than the corresponding value of $s(t)$. Both the signals are shown in the time domain in the first column of Figure 2.3. The small difference in the two signals at data point 512 is not apparent from these figures. In the second column their respective DFT's are plotted. The DFT plots correctly identify the frequency content of the signals, but there is no indication of any difference in the two signals based on their frequency domain representation. The third column shows the first level (DWT) details of the signals obtained using the DB wavelet. The difference in the two signals is clearly identified in this plot. The plot corresponding to the first level DWT of $sd(t)$ shows a clear spike around data point 512.

Similarly, a difference is noted in the fourth column, where the contour plots of the CWT coefficients obtained using the complex Morlet wavelet, of the two signals are plotted. In these plots dark color (black) indicates non-zero coefficient values. The contour plot corresponding to $sd(t)$ clearly indicates large coefficient values around data point 512, where as for the plot corresponding to $s(t)$ all coefficients are zero. The dark portions near the

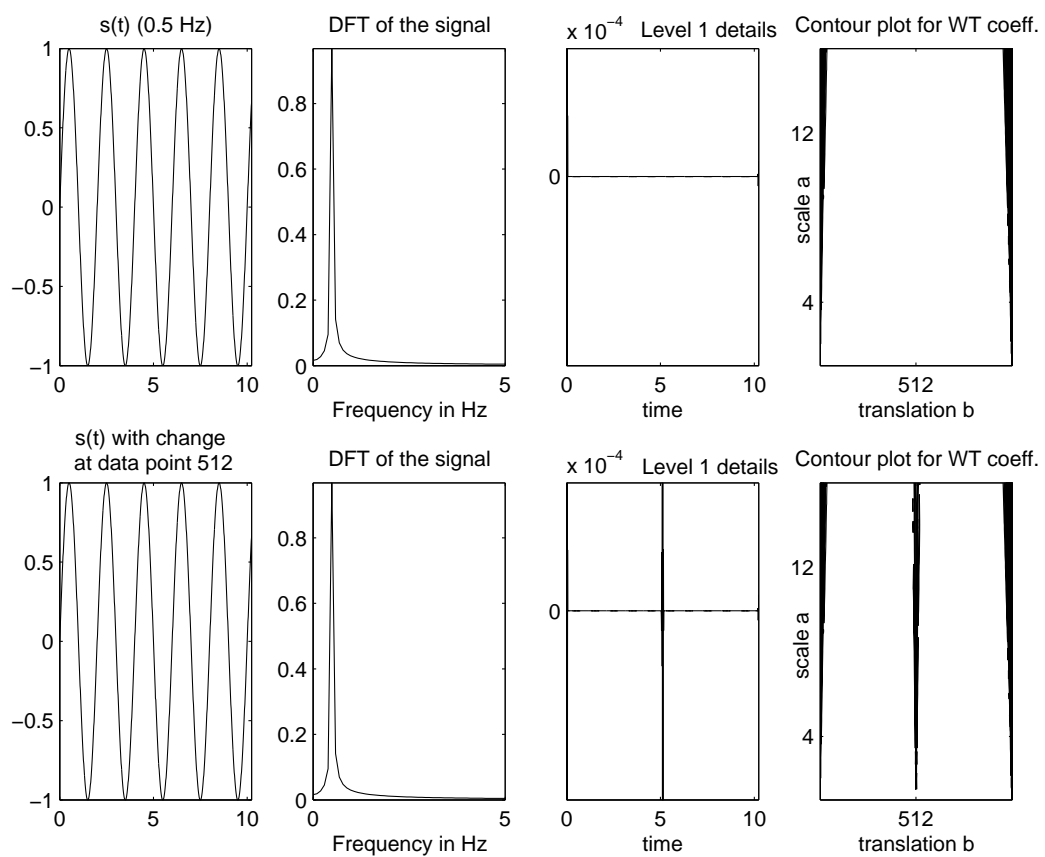


Figure 2.3: Time/space localization using WT

ends of the two graphs can be neglected as they are caused by the so called *end effects*. This simple example shows that both the discrete and continuous wavelet transforms are able to isolate and localize the discontinuity in the signal.

Sudden discontinuities can be thought of as high frequency events. The DWT provides the approximations and details at different levels of a signal. However, the highest frequencies are contained in the lowest level details, as indicated by the first level details shown in Figure 2.3. Similarly in the CWT, the higher frequencies are captured in the coefficients obtained at lower scales. Thus, discontinuities are generally best identified in the lower level details of DWT or by the coefficients at lower scales in the CWT. However, as mentioned earlier the CWT gives a redundant representation of the signal. Thus, if localization, like the one shown in Figure 2.3 is all that is desired, then the DWT is a better alternative. The first level details are simply calculated by passing the signal through a high pass filter. Thus the effort of calculating the wavelet coefficients at other scales is avoided.

The above or similar procedures have been utilized in several studies to locate the position of cracks in beams and plate like structures. The basic idea is to compare the DWT or CWT coefficient plots of the deflection patterns of the structure in damaged and undamaged structure, and identify the distinct differences in these two plots. For example, in Ovanesova and Suarez (2004), the deflected shapes under static and dynamic load was analyzed by CWT to locate a simulated crack in a beam and a frame structure. Similarly, the wavelet transform approach was used in Wang and Deng (1999), and Haase and Widjajakusuma (2003) to identify cracks under static and impact loads in beams with different boundary conditions, and to identify multiple cracks with their dept and locations in, Lu and Hsu (2002), Chang and Chen (2003, 2005). A concrete pavement and a prestressed concrete beam were tested in Melhem and Kim (2003), under repeated loading to identify the development of cracks with the WT approach. In Patsias and Staszewski (2002), the authors use the WT and DWT with the successive recorded images of a vibrating cantilever to extract mode shapes which are again processed by WT to locate the the groove simulating a crack. A similar use of WT is reported in Okafor and Dutta (2000), to detect the presence, location and amplitude of the damage in a cantilever beam using displacement data obtained using a laser vibrometer. In Demetriou and Hou (2002), the damage

detection capability of wavelet transform and an artificial neural network based algorithm are compared for simple spring mass systems with nonlinear system stiffness. Damage is simulated as the sudden breakage of springs. The study shows that wavelet analysis is able to correctly identify the time instances at which the damage occurs. In comparison to the neural network scheme WT approach is shown to be less model dependent, and requires less data for damage detection. The technique for damage detection using DWT have also been applied to randomly excited structures (Masuda, *et. al.* 2002), and to the ASCE benchmark structure (Hera and Hou, 2001; Hera and Hou, 2004).

2.3.3 Separating frequency components

The ability of wavelet transform to separate different frequency components in a signal is of interest in identifying modal parameters. By examining the plot of the coefficients of the CWT of a signal, that contains various frequencies, the different frequency components can be isolated and their stretch in time can be localized.

The CWT of the following function consisting of two frequencies is obtained using the complex Morlet wavelet (defined by Eq. 2.20),

$$s(t) = \sin(2\pi 2t) + 2e^{-0.2t}\sin(2\pi 5t) \quad (2.21)$$

Figure 2.4 is a three-dimensional plot of the absolute values of the wavelet coefficients plotted as a function of scale and translation. Two characteristics of the signal can easily be pointed out based on this plot. First, the signal contains two frequency components. Secondly, the higher frequency component (lower scale correspond to higher frequency) dies off, whereas the lower frequency persists throughout.

Figure 2.5 contains three plots. The first is the contour plot of the absolute value of the wavelet coefficients for the signal $s(t)$. It provides the same information as Figure 2.4.

In the second plot the log of the absolute values of the complex wavelet coefficients at the scale value of $a = 15$, are plotted as a function of time. This plot can be used to evaluate the product of damping ratio and damped

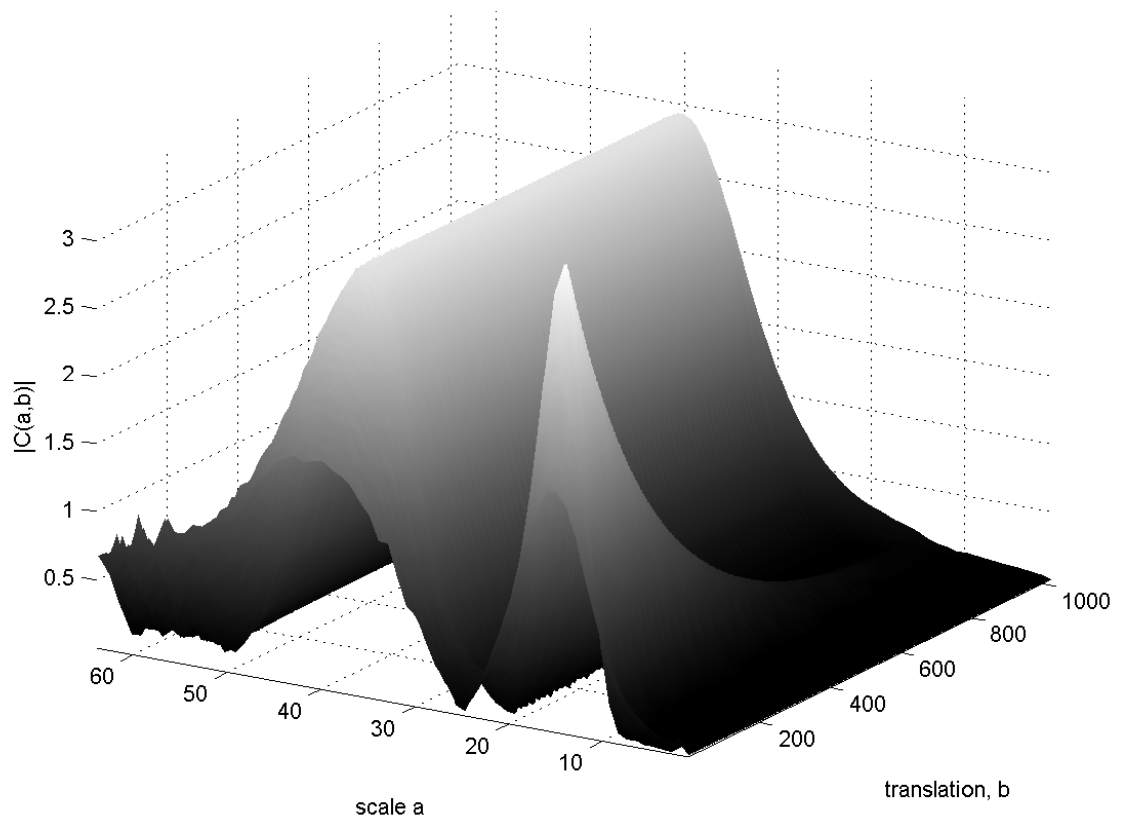


Figure 2.4: Plot of absolute value of the CWT coefficients for the sum of two sines

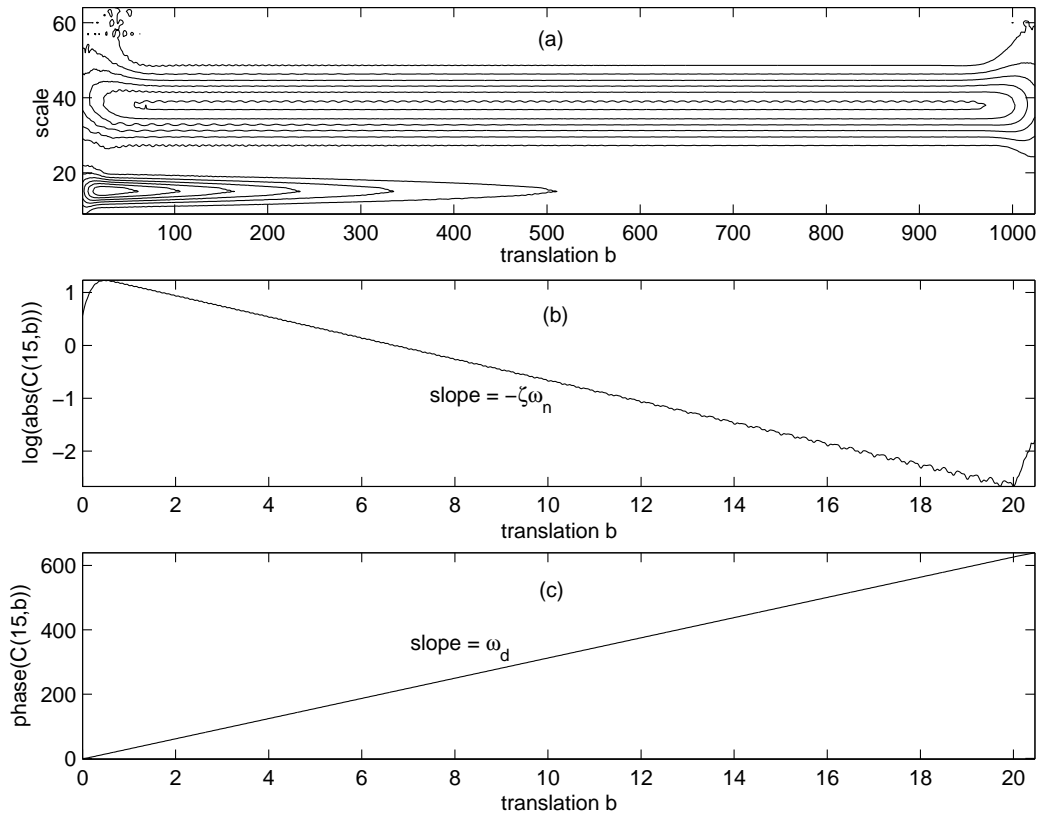


Figure 2.5: Plots for the sum of two sines, (a) contour value of the CWT coefficients, (b) $\log(\text{abs}(\text{CWT coefficients at } a = 15))$ - time plot (c) $\text{phase}(\text{CWT coefficients at } a = 15)$ -time plot

natural frequency of the sinusoidal component corresponding to a scale value of 15, as represented by the second term in Eq. 2.21.

The third plot shows the phase of the complex coefficients at $a = 15$, as a function of the translation parameter. This plot can be utilized to evaluate the damped natural frequency of the component corresponding to a scale value of 15. More of this would be said in later sections.

2.4 Modal Parameter Identification

The modal parameters such as modal frequencies, damping ratios, and mode-shapes are among some of the important characteristics of a dynamic system. The knowledge of these parameters can be specially helpful in structural health monitoring. Thus, the identification of these parameters from the measured dynamic response has been of significant interest in the engineering community recently. The last subsection showed that the wavelet transform can be used to separate different frequencies that exist in a signal. In this section we will focus more on the use of this capability in identifying the modal properties of a structural or mechanical system from recorded dynamic response quantities.

As shown in Figure 2.4, various frequency components of a signal display themselves in the CWT plot at different scale values. If such a plot is created for a dynamic response quantity of a structural systems, it will show the contributions of the frequencies in the input as well as the contributions of different modes that appear in the response quantity. To extract parameters of system modes from such plots, one should first remove the contribution from the input frequencies. This can be done if one uses the free vibration response caused by some initial disturbance or the impulse response function of the system. The impulse response function for a response quantity can be calculated if the measured response and input time histories are available. Figure 2.6 shows the impulse response function for the absolute floor acceleration of the first floor of a three story shear building excited at its base by an earthquake induced ground motion. The mechanical properties of this shear building model are provided later in section 2.5. To obtain this impulse response function, first the frequency response function of the response quantity was obtained using the Fourier transforms of the acceleration response and base input time histories as follows:

$$H_k(\omega) = \frac{FFT(\ddot{x}_k(t))}{FFT(\ddot{x}_g(t))} \quad (2.22)$$

where $\ddot{x}_k(t)$ is the k^{th} floor acceleration, and $\ddot{x}_g(t)$ is the ground acceleration, and $FFT(\cdot)$ denotes the DFT calculated using the FFT algorithm. The inverse Fourier transfer function of this frequency response function provided the impulse response function for the acceleration response.

$$h_k(t) = IFFT(H_k(\omega)) \quad (2.23)$$

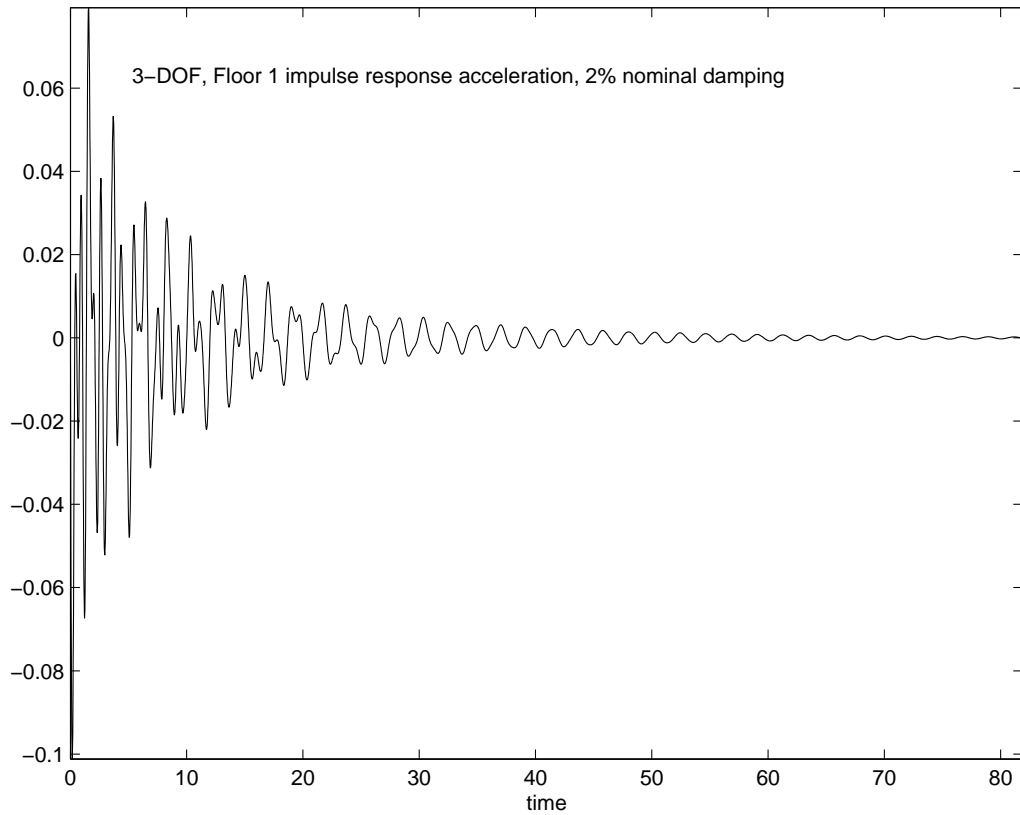


Figure 2.6: Floor 1 impulse response acceleration for the 3-DOF structure

In Figure 2.7 the CWT plot for this impulse response function of the absolute acceleration is shown. The CWT coefficients for this plot were obtained using Morlet wavelet with appropriate parameters. More will be said about the section of these parameters to get desired resolution in the CWT plot. This plot clearly shows three ridges at values of the scale parameter which corresponded to the three modal frequency values. In Figure 2.8 the profiles of these ridges at these three scale values are shown. Each ridge corresponds to a system mode. The formulas that can be used to calculate the modal frequencies and damping ratio values from the CWT coefficients calculated along these ridges using the Morlet wavelet are provided below.

$$\frac{d}{dt} \ln[C(a_k, b)] = -\zeta_k \omega_k \quad (2.24)$$

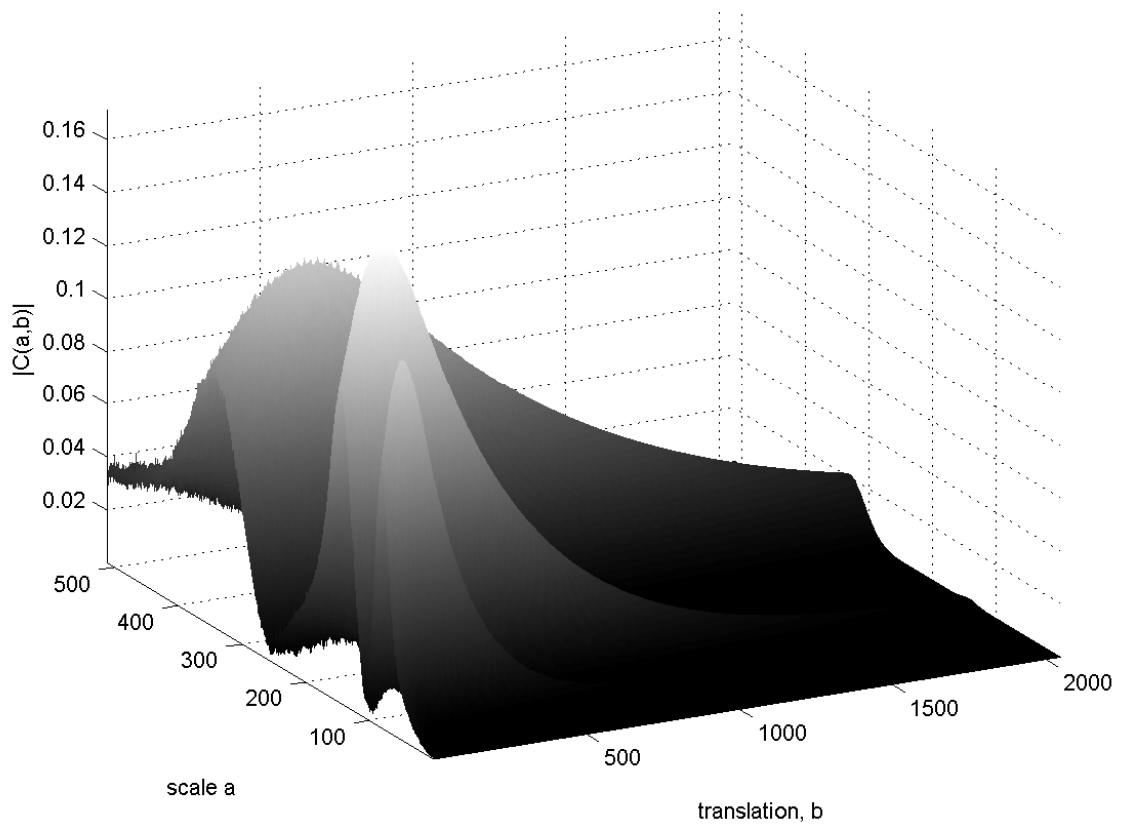


Figure 2.7: Plot of absolute values of the CWT coefficients for the floor 1 impulse response acceleration for the 3-DOF structure

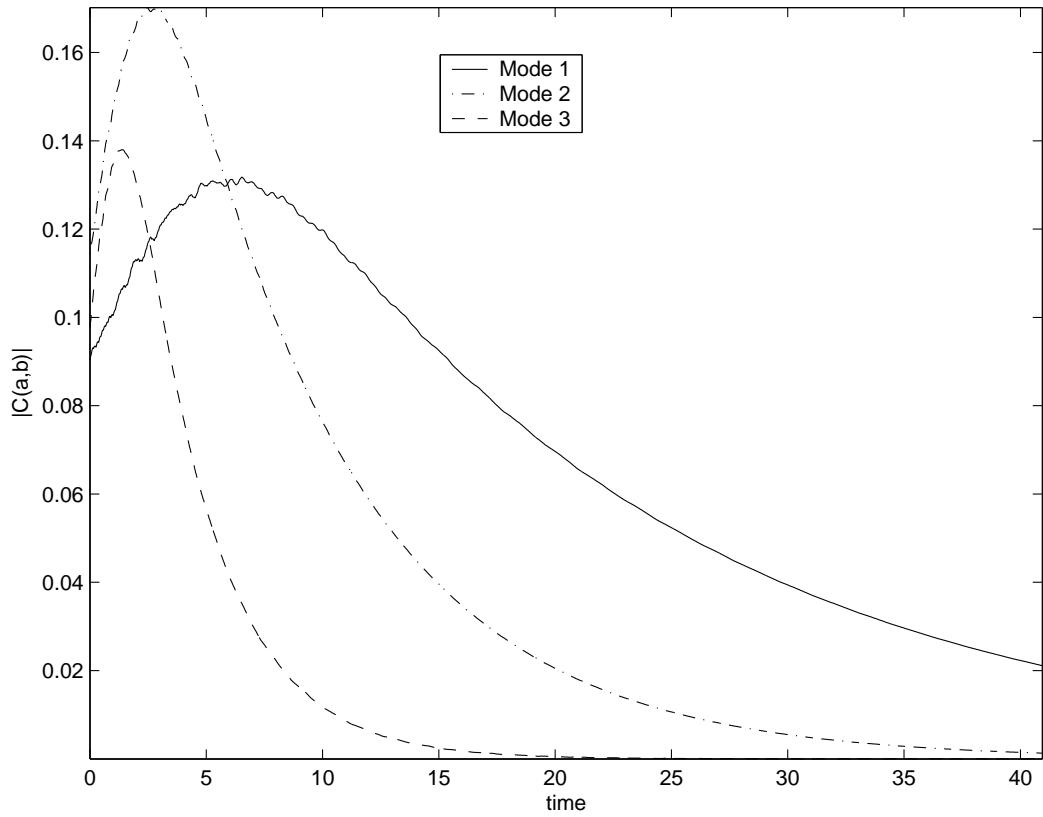


Figure 2.8: Plot of absolute values of the CWT coefficients for the floor 1 impulse response acceleration for the 3-DOF structure at the three scale values corresponding to the three modes

$$\frac{d}{dt}Phase[C(a_k, b)] = \omega_{dk} \quad (2.25)$$

where $C(a_k, b)$ are the CWT coefficients for the scale corresponding to the k^{th} mode, and ζ_k , ω_k and ω_{dk} are respectively the damping ratio, natural frequency and damped natural frequency for the k^{th} mode. The theoretical basis for these formulas relating the frequencies and damping ration with the wavelet coefficients is provided in Ruzzene (1997) and Craig and Demarchi (2003).

To obtain the modeshape values at different degrees of freedom, one needs to have the response recorded at these degrees of freedom. These measured responses are then used to obtain the impulse response functions at these degrees of freedom using Eq. 2.23. The wavelet analysis of these impulse response functions provides the necessary wavelet coefficients which can then be used to calculate the relative mode shape values as follows. The ratio of the k^{th} mode shape values at the p^{th} and q^{th} degree of freedom is obtained from,

$$\frac{|\Phi_{pk}|}{|\Phi_{qk}|} = exp[A_{pk}(t_0) - A_{qk}(t_0)] \quad (2.26)$$

where Φ_{pk} and Φ_{qk} are the k^{th} mode shape values at the p^{th} and q^{th} degree of freedom, and $A_{pk}(t_0)$ ($A_{qk}(t_0)$) are the ordinates at any time t_0 of the least square fit straight line to the plot of $\log |C(a_k, b)|$ versus time at the p^{th} (q^{th}) DOF. The relative sign of the mode shape values are obtained from,

$$\frac{\Phi_{pk}}{\Phi_{qk}} > 0 \quad \text{if} \quad \theta'_{pk}(t_0) - \theta'_{qk}(t_0) = \pm 2m\pi \quad (2.27)$$

$$\frac{\Phi_{pk}}{\Phi_{qk}} < 0 \quad \text{if} \quad \theta'_{pk}(t_0) - \theta'_{qk}(t_0) = \pm(2m + 1)\pi \quad (2.28)$$

where $\theta'_{pk}(t_0)$ and $\theta'_{qk}(t_0)$ are the values of the least square fit straight line to the plot of $Phase[C(a_k, b)]$ versus time, at any t_0 at the p^{th} and q^{th} DOF respectively. The theoretical basis of this is well explained in (Le and Argoul, 2004)

From Eq. 2.24 it can be seen that a linear relationship exists between $\ln[C(a_k, b)]$ and t . If $\ln[C(a_k, b)]$ is plotted as a function of time t , the slope of the line would equal $-\zeta_k\omega_k$. Similarly, from Eq. 2.25 it can be seen that if $Phase[C(a_k, b)]$ is plotted as a function of time, the slope of the line would

equal ω_{dk} . However, the range over which a straight line can be fitted depends on certain parameters of the chosen wavelet. In the case of Morlet wavelet which has been commonly used, these parameters are the bandwidth and the central frequency of the Morlet wavelet. These characteristics of this wavelet which is defined by Eq. 2.20 are discussed in the following paragraph.

In Figure 2.9 the real part of the complex Morlet wavelet is shown for $f_c=10\text{Hz}$, $f_b=1\text{Hz}$ and three different scale values ($a=0.5, 1$ and 2). Corresponding to each of these, on the right side of the plot the absolute value of the discrete Fourier transform (DFT) is shown. The horizontal axis for the DFT represents the frequency in Hz. The well known fact of *dilation in time domain* corresponds to *contraction in frequency domain* can be seen from the figure. As we increase the scale parameter, a , the wavelet is stretched in time domain and correspondingly its DFT shifts towards lower frequencies and the spread of the DFT decreases. The figure illustrates the fact that wavelets have a good time resolution at high frequencies (lower scales) and a good frequency resolution at low frequencies (higher scales).

For the Morlet wavelet a simple relationship between the scale parameter a and the signal frequency f_x exists (Staszewski, 1997),

$$a = \frac{f_c f_s}{f_w f_x} \quad (2.29)$$

where f_s and f_w are the sampling frequencies of the signal and the wavelet respectively.

Modifying the traditional Morlet wavelet has also been suggested (Lardies and Gouttebroze, 2002). Here it is shown that by modifying the definition of the Morlet wavelet better frequency resolution can be achieved which enhances the capability of the Morlet wavelet for modal parameter estimation. However in the present study the traditional Morlet wavelet is used.

By changing the two adjustable parameters of the Morlet wavelet, i.e. the central frequency, f_c and the bandwidth f_b , closely spaced modes can be separated. These parameters also influence the shape of the $\ln[C(a_k, b)]$ -time graph. These effects of the central frequency and the bandwidth parameters are studied next.

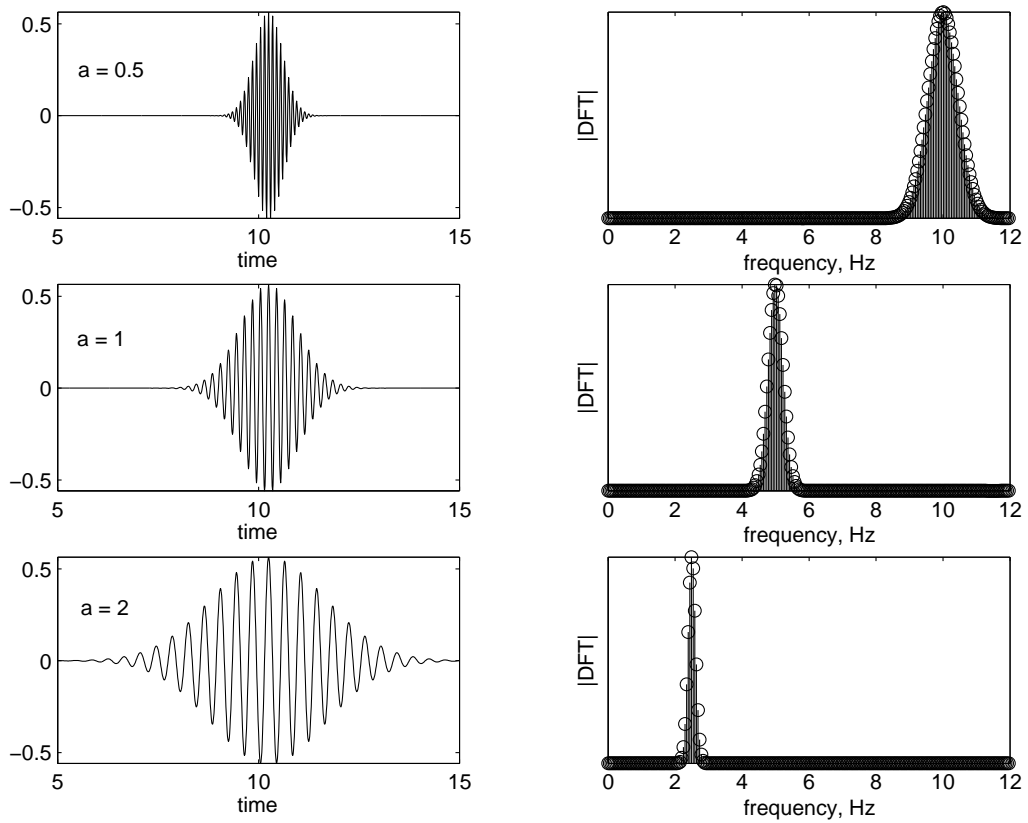


Figure 2.9: Real part of the complex Morlet wavelet and its DFT for $f_c=5\text{Hz}$, $f_b=1\text{Hz}$ and three different scale values

Central frequency, f_c

When extracting the modal parameters one needs to have some idea about the value of the scale parameter at which the modal responses should be extracted. This is illustrated in Figure 2.4 and Figure 2.5(a). It can be seen that the decaying sinusoidal signal (Eq. 2.21) is basically represented by the values of a near 15 in the time-scale plane. If one knows the signal frequency, in this case 5 Hz, and decides on some central frequency of the Morlet wavelet ($f_c=1.5$ Hz for the plots) then the scale value can be calculated from Eq. 2.29.

When the impulse response of a multi-dof system is decomposed in the time-scale plane, contributions from individual modes can be obtained at scale values corresponding to the modal frequencies. An estimate of the scale parameter at which the wavelet transform coefficients are to be calculated can be obtained either from the DFT plot or by looking at the CWT contour plots.

It is important that f_c for the Morlet wavelet is chosen such that all the modes are well separated and identifiable when the response of a MDOF system is represented in the time-scale plane. If a very low value of f_c is chosen the modal responses might not be well separated and one might be led to the conclusion that there are less number of modes than actually present in the response data. This feature is represented in Figure 2.10 where the impulse response at the first floor of the 3-dof system is decomposed in the time-scale plane using three different values of f_c . In the first two plots (for $f_c = 1$ Hz and 2 Hz) one can see just a hint of two close modes. This is separated out for $f_c = 3$ Hz and three distinct modal responses can be seen in the third plot. If higher values of f_c are chosen the second and third modes can be put further apart.

Increasing the central frequency although leads to a better separation of modal responses, but has the disadvantage of larger group delays. This becomes an obvious problem when a straight line plot has to be fit in the $\log(Abs(CWT\ coeff))$ -time plot. This can be seen in Figure 2.11 where the plots used in the calculation of the product of the natural frequency and damping ratio ($\zeta_k\omega_k$) for the different modes are shown for the 3-dof structure. Two different central frequencies, 10Hz and 5Hz, have been used to extract the modal parameters. For the case of $f_c = 10$ Hz it can be seen that

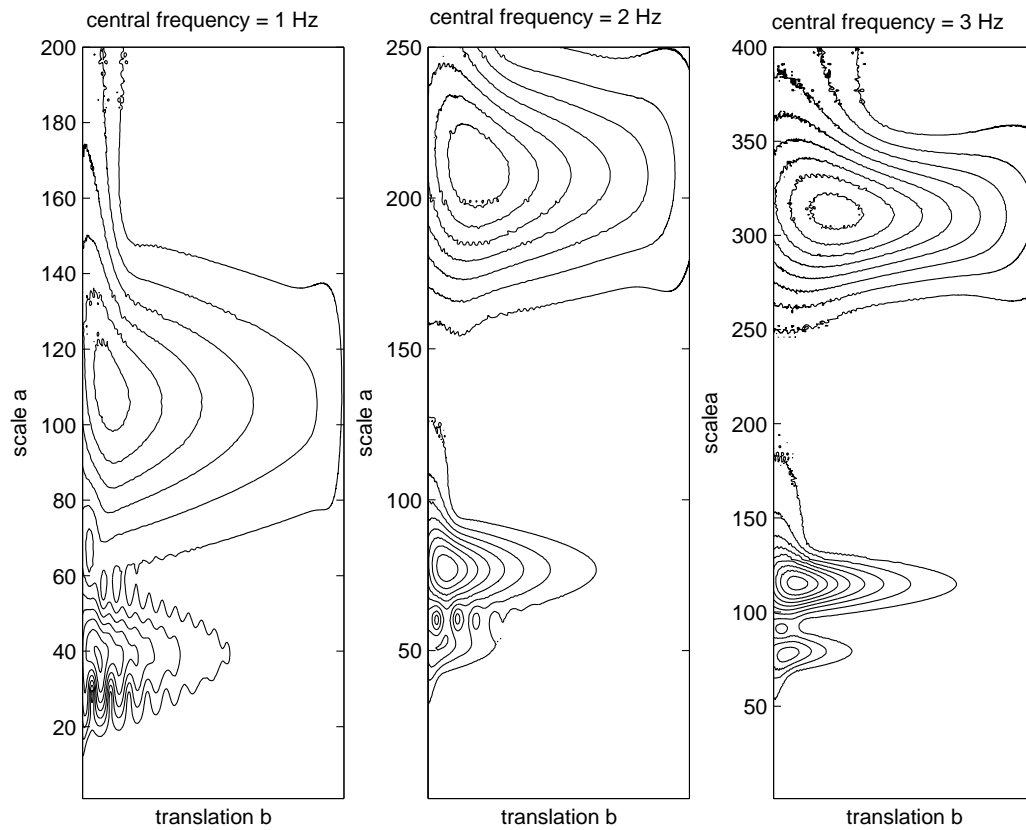


Figure 2.10: Absolute value of CWT coefficients contour plots for different f_c showing the separation of modal responses for the 3-dof structure.

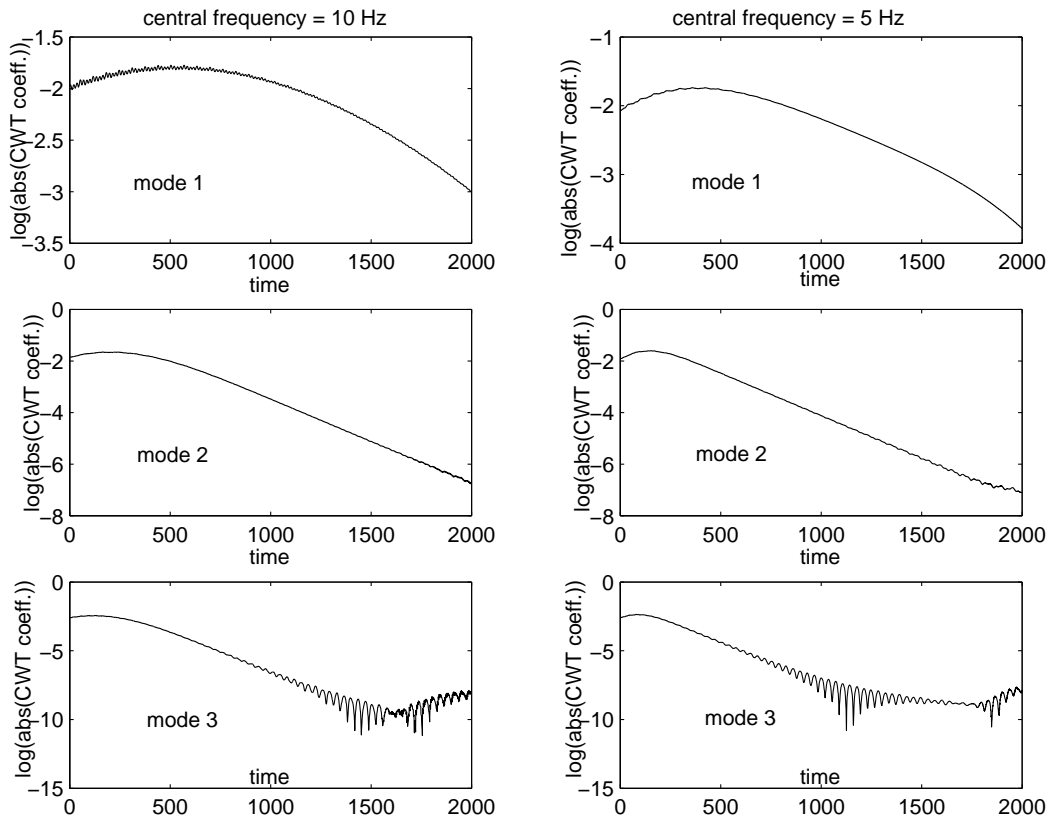


Figure 2.11: $\log(Abs(CWT\ coeff))$ - $time$ plot for the three modes of the 3-dof structure for two different f_c

the portion of the plot where a straight line can be fitted for the first mode is smaller than that for $f_c = 5\text{Hz}$.

Therefore, larger values of f_c will separate closely spaced modes but will induce larger errors in modal parameters specially for the lower modes.

Bandwidth, f_b

The second adjustable parameter in Eq. 2.20 is the bandwidth parameter, f_b . The bandwidth parameter dictates how fast or how slowly the mother wavelet decays in time (or the spread of the mother wavelet in time domain). Also since the increase in f_b lowers the decay rate of the mother wavelet in

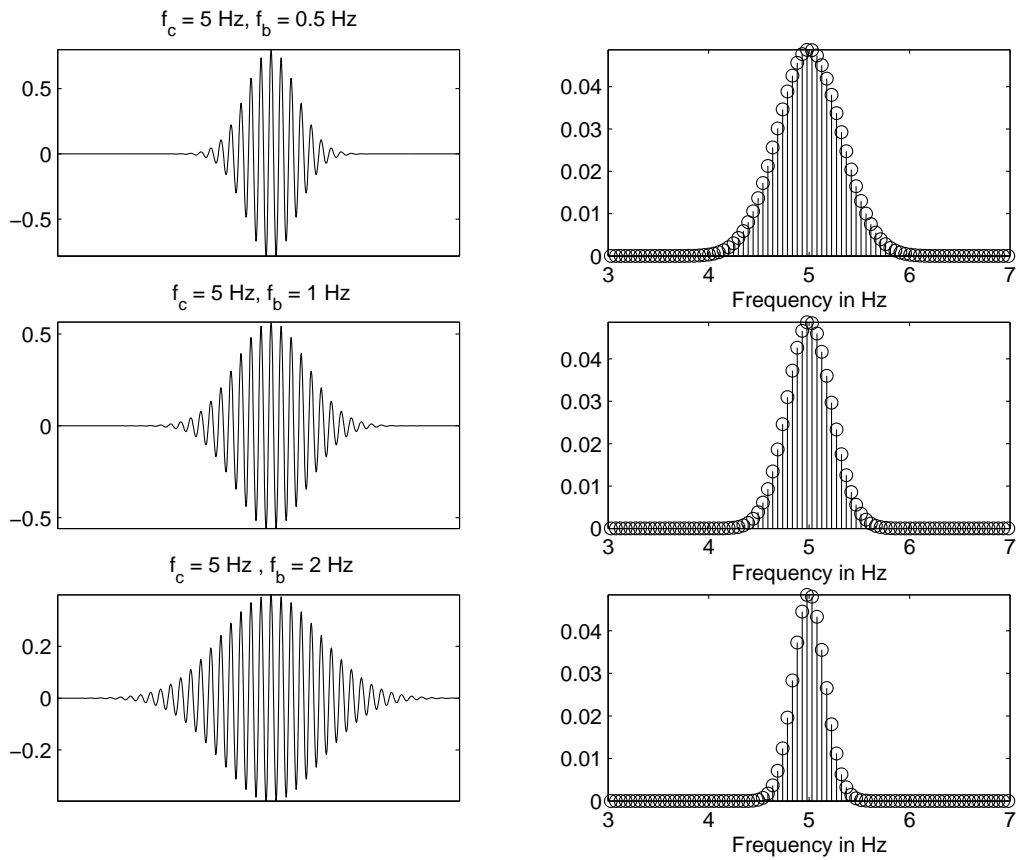


Figure 2.12: Real part of the complex Morlet wavelet and its DFT for $f_c = 5$ Hz and three different f_b values

time domain, it results in a more concentrated plot in the frequency domain. This is shown in Figure 2.12

Wavelet transform is a constant- Q analysis. Which means that the factor Q (or the relative bandwidth) of the wavelet transform filters are constant, independent of the scale parameter (Q , the fidelity factor is defined as the ratio of the central frequency and the bandwidth of a filter). The bandwidth parameter of the Morlet wavelet provides a way of tuning the value of Q .

The effect of f_b in the identification of modal parameters is shown in Figures 2.13 and 2.14. These are the plots of the same quantities as in

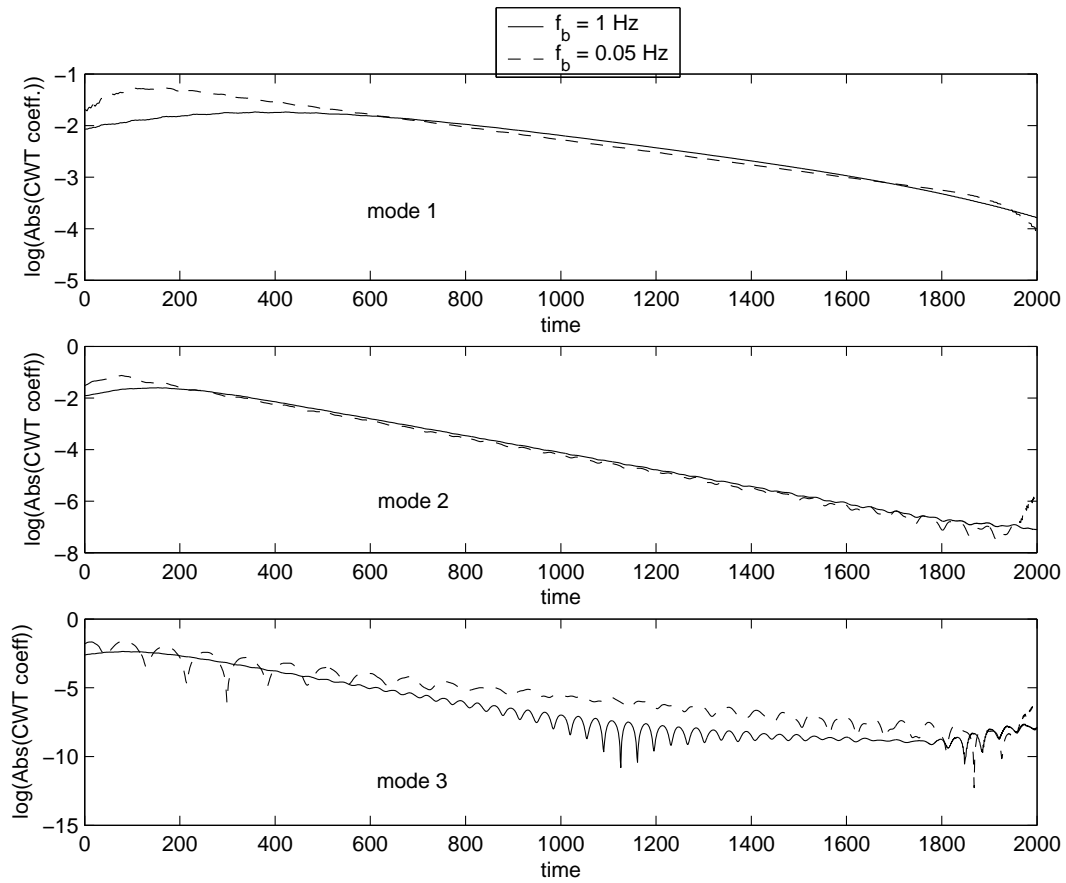


Figure 2.13: $\log(\text{Abs}(\text{CWT coeff.}))$ - time plot for the three modes of the 3-dof structure for two different f_b

Figure 2.11. From Figure 2.13 it can be seen that choosing a very low value of f_b would create problem for the higher modes when a straight line is to be fitted to the plot. Similarly, Figure 2.14 illustrates the fact that using a very high value for f_b makes the plot for lower frequency much like a smooth curve. In the present study a constant value of 1Hz was used for f_b for all the cases.

In all the simulation cases presented in the study, for a given system, fixed values of the central frequency and the bandwidth parameter were used for modal identification from all the floor data, for all the modes. Since the

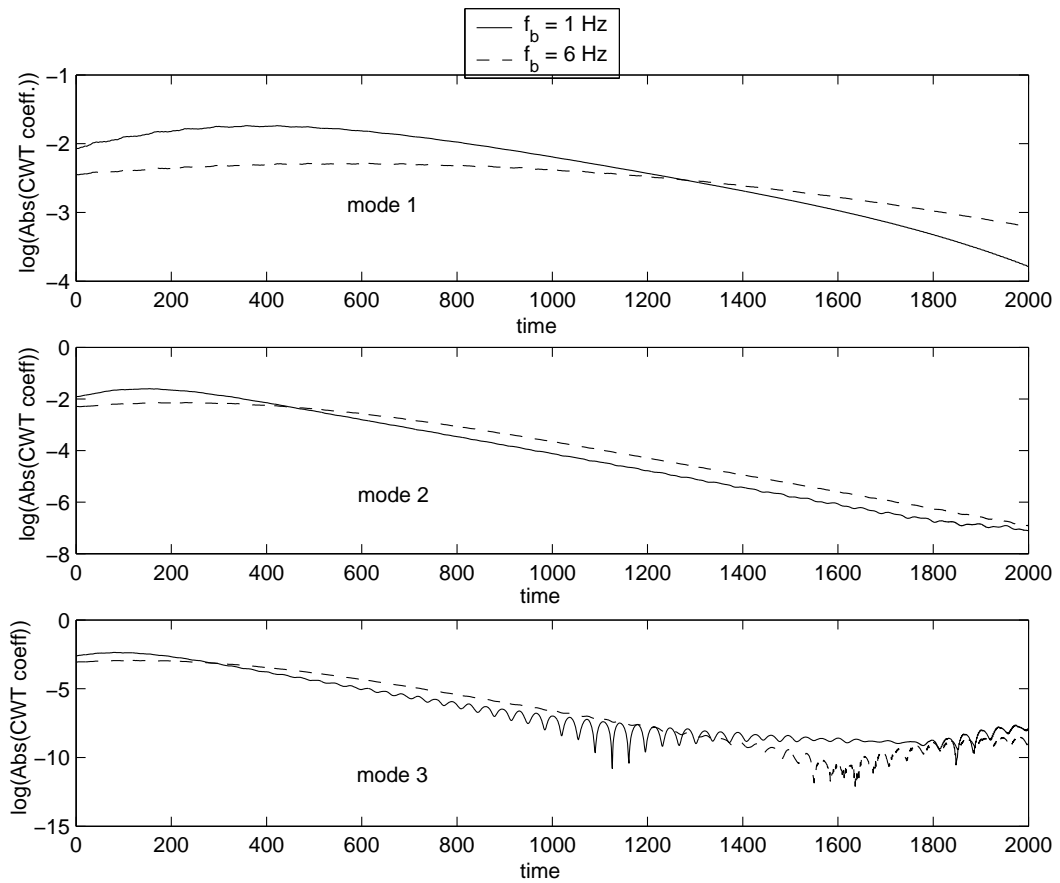


Figure 2.14: $\log(\text{Abs}(\text{CWT coeff}))$ - time plot for the three modes of the 3-dof structure for two different f_b

Table 2.1: Modal properties of the 3-DOF model

Mode no.	ω_n	ζ_n	ζ_n	ζ_n
1	2.8457	0.0200	0.0500	0.1000
2	6.5711	0.0200	0.0500	0.1000
3	11.3475	0.0276	0.0690	0.1380

Table 2.2: Modal properties of the 6-DOF model

Mode no.	ω_n	ζ_n	ζ_n	ζ_n
1	9.4994	0.0200	0.0500	0.1000
2	23.8988	0.0200	0.0500	0.1000
3	38.2365	0.0265	0.0661	0.1323
4	49.4017	0.0323	0.0808	0.1617
5	60.3579	0.0384	0.0960	0.1920
6	72.1722	0.0451	0.1128	0.2255

spread of the modal frequencies may be large, the use of fixed values will affect different modal responses to a different extent. This was illustrated in Figures 2.11 2.13 and 2.14. The greater error observed in the identified modal parameters for the first mode in various cases can be explained because of this effect. Also, the use of different central frequencies for the identification of modal parameters of different modes can decrease the subjectiveness in fitting a straight line to the plot of $\log(Abs(CWT\ coeff))$. But for that a close estimate of the modal frequencies should be known before hand.

2.5 Numerical results for modal parameters

In this section the numerical results of the modal parameters obtained by the wavelet approach for three structural models are presented. The first two models were simple lumped mass models with 3 and 6 DOF respectively. In each case three different levels of damping were considered. The properties of these models are listed in Table 2.1 and Table 2.2.

The third model was the benchmark structure specified by the American Society of Civil Engineers (ASCE), SHM committee. This structure is shown

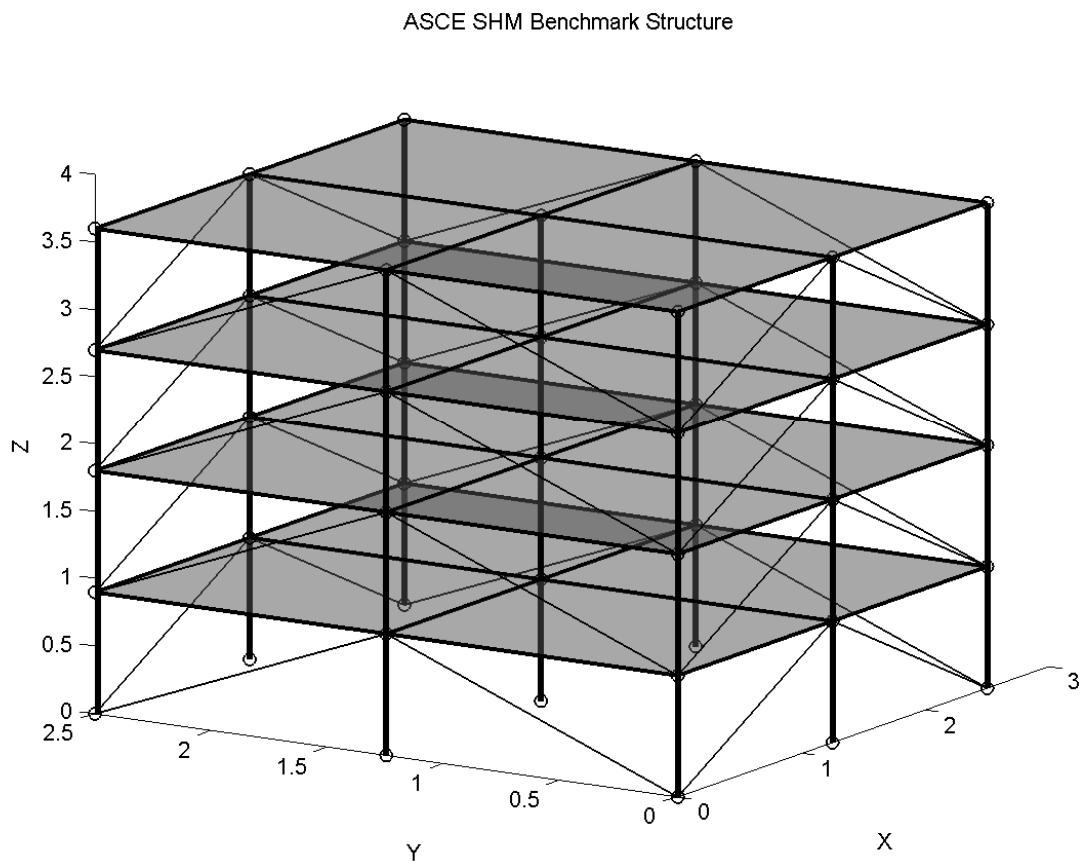


Figure 2.15: The ASCE-SHM benchmark structure

Table 2.3: Modal properties for the translational y-direction of the benchmark structure

Mode	ω_n	ζ_n	ζ_n
y-1	59.1542	0.0200	0.0500
x-1	71.1149	0.0200	0.0500
y-2	160.5286	0.0282	0.0701
x-2	201.1806	0.0335	0.0837
y-3	243.0246	0.0392	0.0979
y-4	301.7583	0.0475	0.1187
x-3	304.4989	0.0479	0.1196
x-4	378.0857	0.0585	0.1462

in Figure 2.15. It is a 4-story, 2 bay by 2 bay framed structure, with bracings on all sides on all floors. The details of the model and the various damage cases to be studied for this benchmark structures can be found in (Johnson, *et. al.*, 2000). For the purpose of numerical study the ASCE-SHM committee provides MATLAB codes to carry out the simulations and generate floor acceleration responses at defined locations. These being, four responses at each floor, two in each horizontal direction.

Structural models with 2% and 5% modal damping were considered. Table 2.3 lists the translational modal parameters of this structure obtained with the analytical models. To demonstrate the ability of WT for calculating these actual values of the modal parameters from recorded data, each structure was analyzed to calculate the absolute accelerations at different floor levels for simulated base motions representing earthquake induced ground motions. To calculate these floor motions for the benchmark structure, the original code provided by the benchmark committee was modified. These floor accelerations and corresponding base motions were then used to calculate the impulse response function for these response quantities from Eq.2.22 and 2.23. These impulse response functions were then used in calculating the wavelet coefficients followed by the calculation of modal frequencies, damping ratios, and mode shapes using Eq. 2.24 through Eq.2.26.

For all the models two separate scenarios were considered. One in which the simulated acceleration response was used to calculate the impulse re-

sponse. This being the case of no-noise. For the second scenario, random numbers were generated and added to the acceleration response. This simulates the case of measurement being corrupted by noise. The noise corrupted acceleration response was then used to calculate the impulse response. In what follows, first results for the case of no-noise are presented. Later, results for the case of noisy data are summarized. In all cases impulse responses were used for identification purposes, which were generated using Eq.2.23 and 2.22.

2.5.1 No-noise case

The percentage error in the identified parameters (natural frequencies and damping ratios) using the wavelet approach are presented in Tables 2.4-2.6 for the 3-dof for 2%, 5% and 10% damping respectively, and Figures 2.16-2.18 show the identified mode shapes for the different damping ratio cases. It can be seen that for the case of higher damping (10%) larger errors are observed specially in the estimated damping. Also the mode shapes seem to be departing from actual values for the case of 10% damping.

For the 6-dof, Tables 2.7-2.9 lists the percentage error in the identified parameters and Figures 2.19-2.21 show the identified mode shapes for the three different damping ratio cases. In this case it must be noted that large errors in damping values are present for higher modes even for the case of 2% damping. The identified mode shapes are accurate for the case of 2% and 5% damping only for the first three modes, and these too depart from actual values for the case of 10% damping.

The numerical results obtained for these two models lead to the conclusion that for higher modes, or higher damping, or for a large system, identification of all the modes may not be possible using the WT approach. This can be explained as follows, the modal parameters are estimated by first fitting a straight line to two plots similar to Figure 2.5(b) and (c) and then calculating the slope. For the case of higher damping or for a system with large DOF the modes die off quickly. As a result the straight line portions of these plots become less and fitting a straight line becomes difficult.

These observations are also confirmed by the numerical results obtained for the benchmark structure. Tables 2.10-2.11 list the percentage errors for

Table 2.4: Percent error in natural frequency and damping obtained from the response of different floors for 3-DOF structure 2% nominal damping

Floor no.	ω_1	ω_2	ω_3
1	-0.3638	-0.0298	0.0235
2	-0.0816	0.0673	-0.0276
3	0.0004	-0.0176	-0.0375
Floor no.	ζ_1	ζ_2	ζ_3
1	0.6286	0.0625	-0.0240
2	0.3445	-0.0345	-0.0401
3	0.2621	0.0504	0.1379

Table 2.5: Percent error in natural frequency and damping obtained from the response of different floors for 3-DOF structure 5% nominal damping

Floor no.	ω_1	ω_2	ω_3
1	-0.5438	-0.0099	0.0663
2	-0.0915	0.0262	-0.0623
3	0.0429	-0.0051	-0.0434
Floor no.	ζ_1	ζ_2	ζ_3
1	0.5138	-0.0787	-0.8254
2	0.0587	-0.2119	-0.4827
3	-0.0757	-0.1078	0.7083

the case of 2% and 5% damping for the benchmark structure, and Figure 2.22 shows the identified mode shapes. Only the first three y-direction mode shapes, and only the first two x-direction mode shapes could be calculated.

2.5.2 Noisy Data

To simulate the real life situation of noise corrupted data, noise was added to the simulated floor accelerations and the corrupted acceleration data was used to estimate the impulse response function. The noisy impulse response function was in turn used for modal identification using the WT approach. It was observed that in the case of the data with noise the identification of modal parameters became almost impossible primarily because fitting straight lines

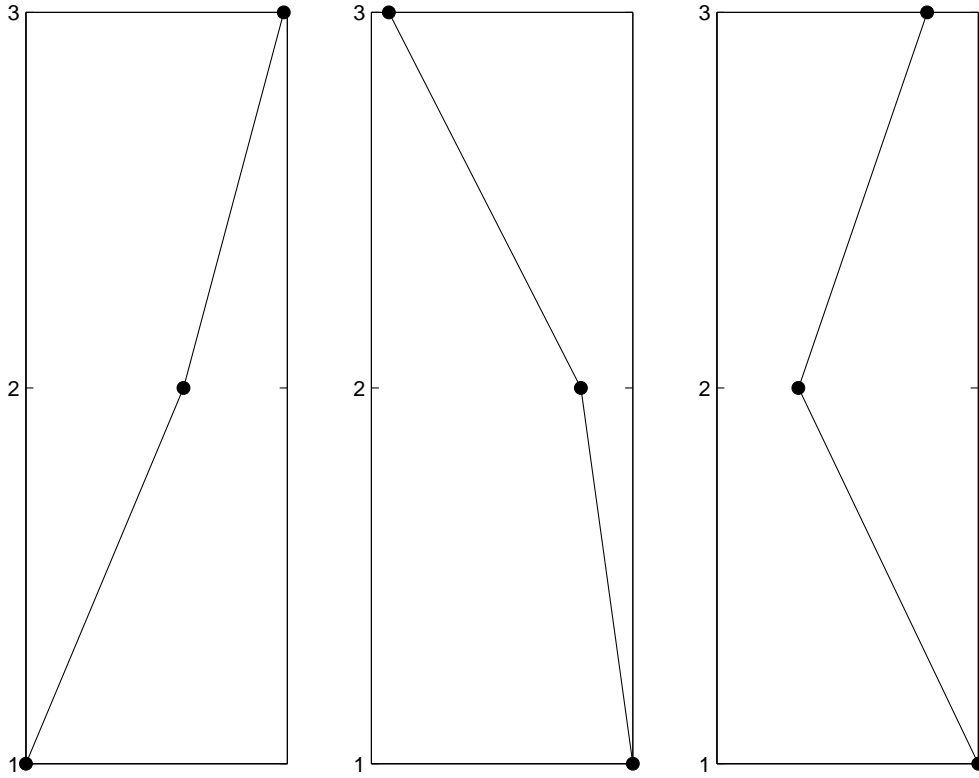


Figure 2.16: Actual and identified mode shapes for 3DOF 2% nominal damping

Table 2.6: Percent error in natural frequency and damping obtained from the response of different floors for 3-DOF structure 10% nominal damping

Floor no.	ω_1	ω_2	ω_3
1	-0.2732	1.5183	1.0429
2	0.0435	1.0072	-0.6302
3	0.1350	1.3792	-0.8965
Floor no.	ζ_1	ζ_2	ζ_3
1	0.1423	-5.4454	-8.9647
2	-0.1747	-6.3492	-6.4516
3	-0.2659	-4.5733	-2.6074

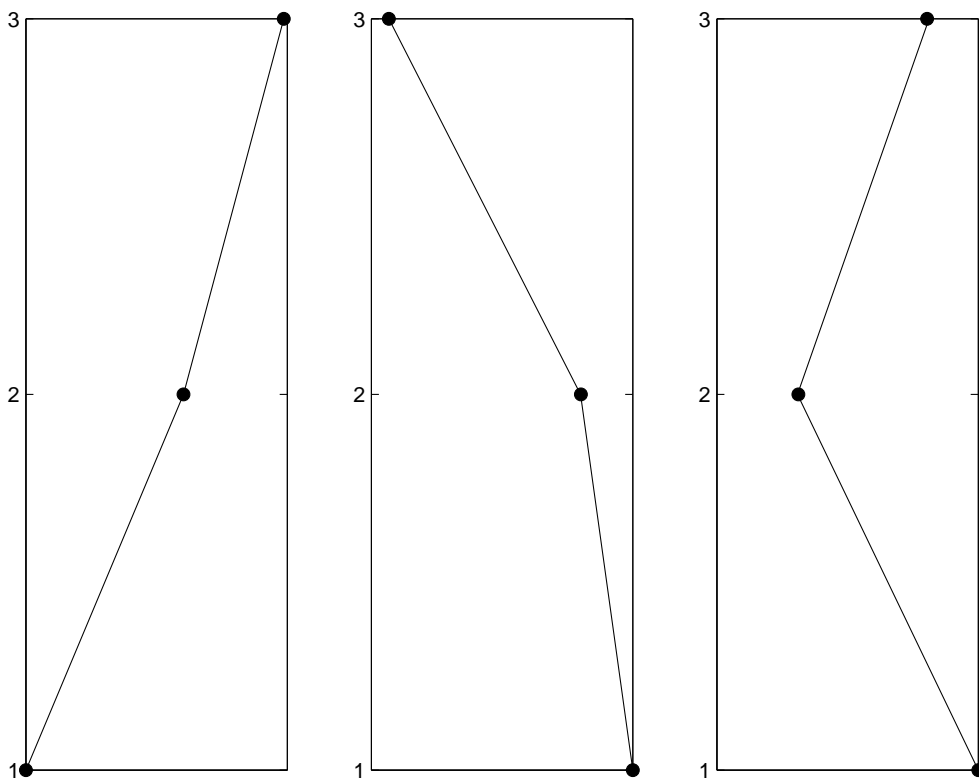


Figure 2.17: Actual and identified mode shapes for 3DOF 5% nominal damping

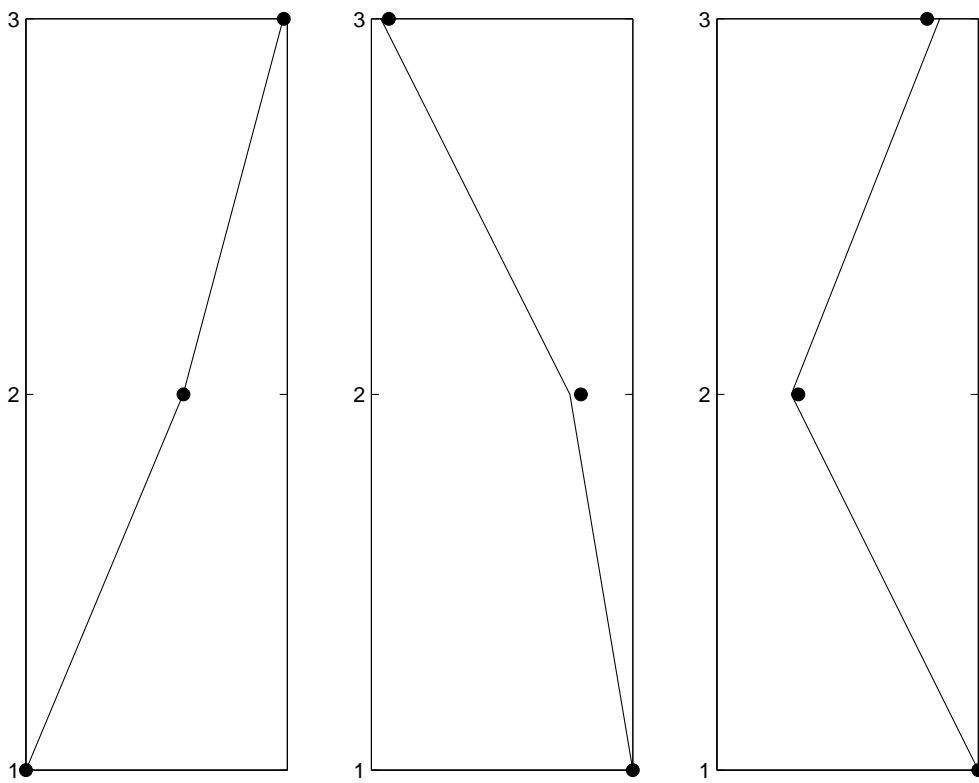


Figure 2.18: Actual and identified mode shapes for 3DOF 10% nominal damping

Table 2.7: Percent error in natural frequency and damping obtained from the response of different floors for 6-DOF structure 2% nominal damping

Floor no.	ω_1	ω_2	ω_3	ω_4	ω_5	ω_6
1	-0.1592	-0.0371	-0.0267	-0.1536	0.0291	0.2478
2	-0.0476	-0.0082	0.033	0.4104	0.0132	-0.0464
3	-0.0171	0.0102	-0.4172	-0.2019	0.2517	-0.2758
4	-0.0034	0.0266	-0.0098	0.3377	-0.0611	-0.4853
5	0.0103	-0.0235	0.0537	-0.1317	-0.2564	-42.969
6	0.0145	0.0005	-0.0012	-0.1795	-59.343	-43.171
Floor no.	ζ_1	ζ_2	ζ_3	ζ_4	ζ_5	ζ_6
1	-0.4142	-0.3982	-0.8598	-3.6425	-9.3737	-9.9056
2	-0.5253	-0.427	-1.2051	-12.266	17.853	-10.692
3	-0.5557	-0.4244	0.4308	-3.5456	-8.9208	-8.9951
4	-0.5693	-0.3361	-0.2844	-14.251	-6.2353	-26.984
5	-0.5829	-0.914	0.2935	-2.9483	-11.277	-90.002
6	-0.5871	-0.6658	-1.8621	-6.4113	20.18	-45.75

Table 2.8: Percent error in natural frequency and damping obtained from the response of different floors for 6-DOF structure 5% nominal damping

Floor no.	ω_1	ω_2	ω_3	ω_4	ω_5	ω_6
1	-0.247	-0.1395	-0.0947	0.047	0.2289	0.3266
2	-0.0905	-0.0148	0.2672	0.418	0.1563	-0.1481
3	-0.0097	0.0673	-0.9821	-0.3219	0.3731	-0.8787
4	0.0239	0.1441	0.0047	0.6677	-0.1738	-34.89
5	0.0491	-0.0966	0.3797	-0.1854	-0.6085	-80.662
6	0.0586	0.018	0.0627	-0.4318	-24.573	-52.328
Floor no.	ζ_1	ζ_2	ζ_3	ζ_4	ζ_5	ζ_6
1	0.3595	0.8395	-10.343	-27.347	-42.24	-46.225
2	0.118	0.4542	-10.868	-36.538	-36.998	-51.535
3	-0.005	0.1376	-2.698	-44.492	-48.182	-65.099
4	-0.0597	-0.3319	-10.523	-63.937	-49.41	-69.168
5	-0.0849	1.5919	-10.444	-44.367	-51.37	-65.687
6	-0.0943	0.848	-11.18	-60.018	-79.717	-79.39

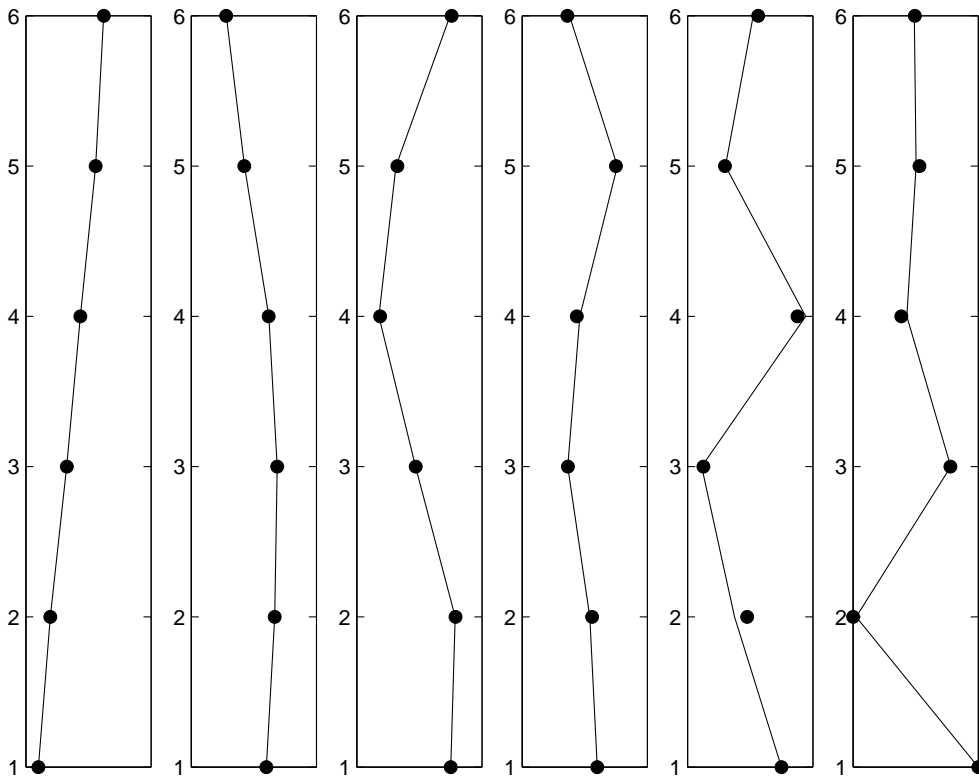


Figure 2.19: Actual and identified mode shapes for 6DOF 2% nominal damping

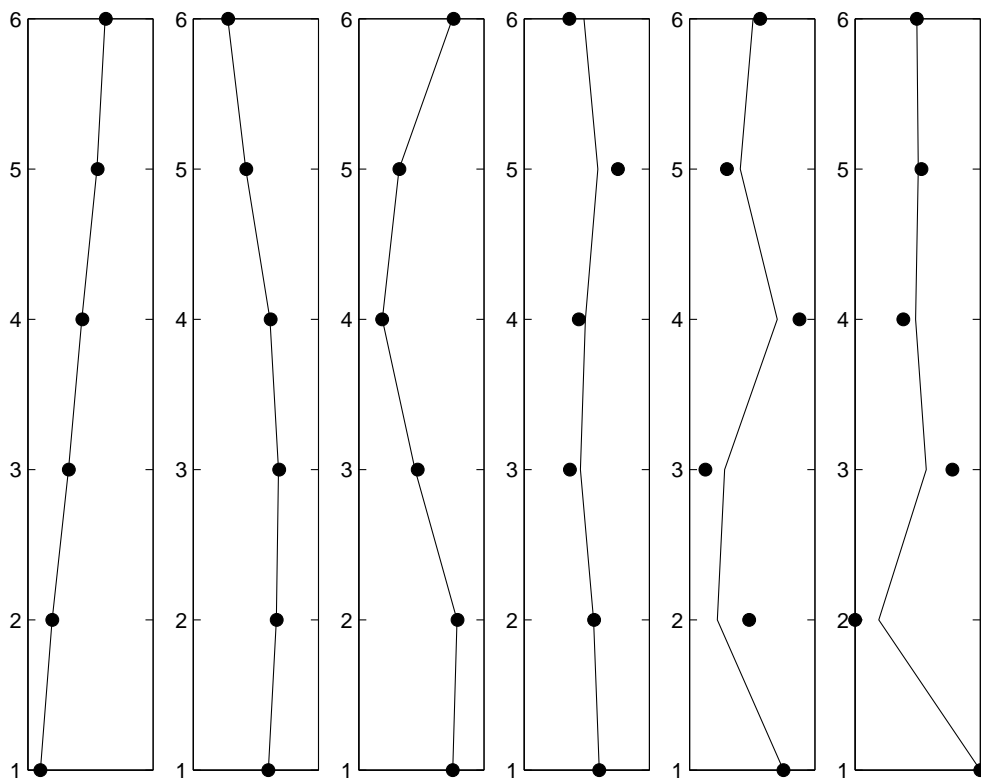


Figure 2.20: Actual and identified mode shapes for 6DOF 5% nominal damping

Table 2.9: Percent error in natural frequency and damping obtained from the response of different floors for 6-DOF structure 10% nominal damping

Floor no.	ω_1	ω_2	ω_3
1	-0.1335	-0.1141	0.1468
2	0.0519	0.1438	0.5217
3	0.1866	0.3488	-0.0744
4	0.2474	0.5433	0.1049
5	0.2927	-0.0718	0.5368
6	0.3109	0.2161	0.2375
Floor no.	ζ_1	ζ_2	ζ_3
1	-8.588	-9.6505	-31.818
2	-9.9357	-10.823	-31.777
3	-10.225	-11.189	-23.702
4	-10.29	-10.87	-35.692
5	-10.299	-12.863	-38.484
6	-10.273	-12.462	-32.021

Table 2.10: Percent error in natural frequency and damping obtained from the response of different floors for the benchmark structure 2% nominal damping

Floor no.	ω_{1y}	ω_{2y}	ω_{3y}	ω_{1x}	ω_{2x}
1	0.0938	0.0411	0.0459	0.1185	0.0422
2	0.0938	0.0411	0.0448	0.1185	0.0422
3	0.0937	0.0411	0.0453	0.1185	0.0424
4	0.0937	0.0411	0.0445	0.1185	0.0423
Floor no.	ζ_{1y}	ζ_{2y}	ζ_{3y}	ζ_{1x}	ζ_{2x}
1	4.1731	0.0643	0.8320	1.1657	0.0990
2	4.2746	0.0489	0.0609	1.0982	0.2801
3	4.3676	0.0908	0.3987	1.0982	0.2801
4	4.4184	0.0643	0.0902	1.0847	0.1777

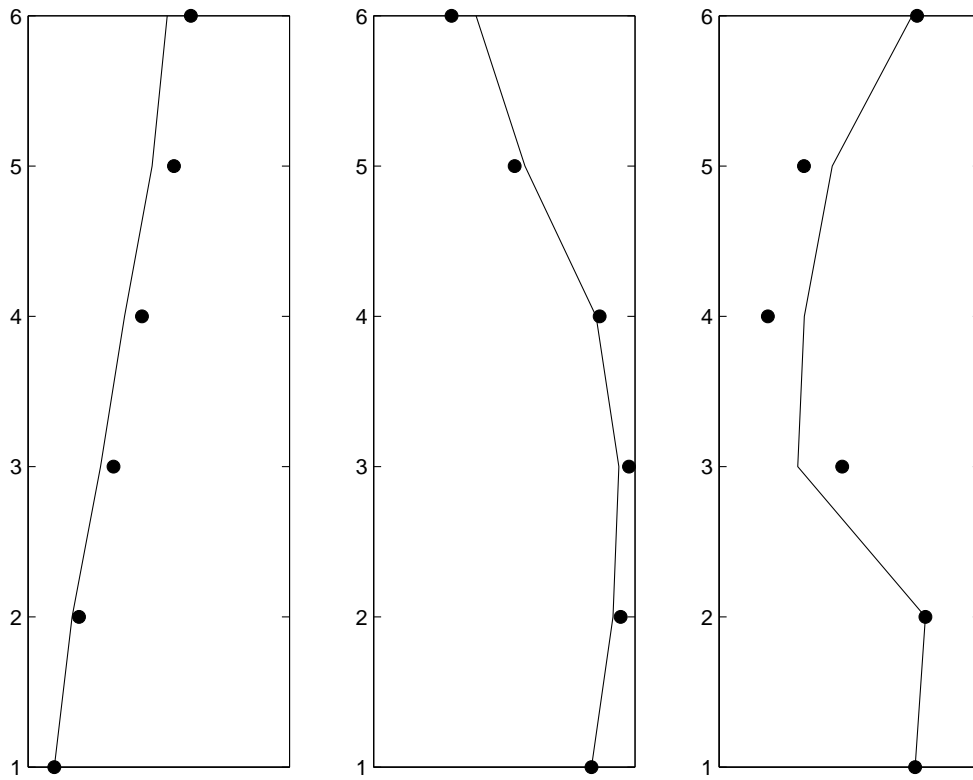


Figure 2.21: Actual and identified mode shapes for 6DOF 10% nominal damping

Table 2.11: Percent error in natural frequency and damping obtained from the response of different floors for the benchmark structure 5% nominal damping

Floor no.	ω_{1y}	ω_{2y}	ω_{3y}	ω_{1x}	ω_{2x}
1	0.3940	0.0517	0.8938	0.2451	0.1484
2	0.3941	0.0516	0.8829	0.2451	0.1485
3	0.3940	0.0500	0.8940	0.2451	0.1414
4	0.3940	0.0505	0.9024	0.2451	0.1448
Floor no.	ζ_{1y}	ζ_{2y}	ζ_{3y}	ζ_{1x}	ζ_{2x}
1	0.7827	1.1244	3.4383	0.8618	4.2320
2	0.7962	1.1033	4.6035	0.8672	4.2450
3	0.7827	0.7919	3.4259	0.8618	3.1921
4	0.7759	0.9001	2.5363	0.8591	3.6934

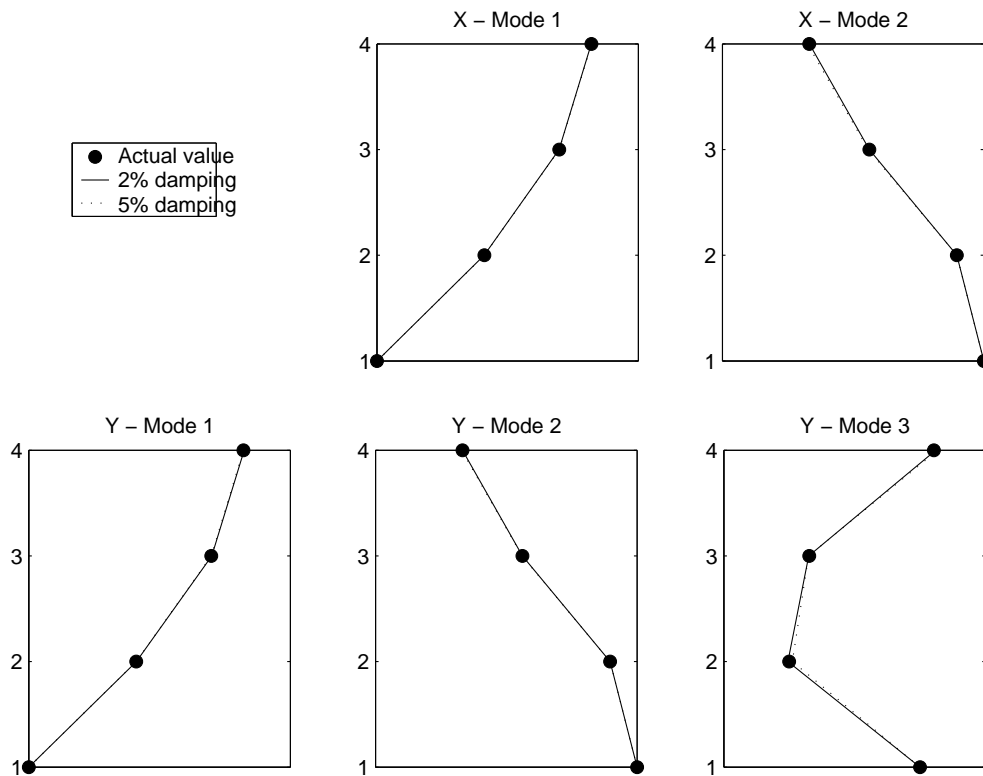


Figure 2.22: Actual and identified mode shapes for the benchmark structure

through the wavelet coefficient and phase plot data was very difficult. This effect of noise on the identification procedure is illustrated through Figures 2.23 to 2.26.

Figure 2.23 shows the plot of the phase of the CWT coefficients as a function of time for the first mode of the 6-DOF structure, extracted from the first floor. As can be seen from the figure the plot for the case of noisy data can be said to be (approximately) as informative as the plot for the case of no noise. Thus the damped natural frequency may be estimated well enough for this case.

For the 6-DOF structure, for the case of signal to noise ratio 20dB Figure 2.24-2.26 show the plot of $\log(Abs(CWT\ coeff)) - time$, for the first three modes using the response of floor 1. For comparison, plots for the case of no noise are also shown. For the first mode (Figure 2.24) the plot for the case of noisy-data oscillates randomly about the actual noise-free plot. For higher modes (Figure 2.25 and 2.26) the plot not only oscillates randomly but it flattens out much before the mode actually dies (represented by the plot for the noise free case). In each of these plots a straight line is to be fitted for the estimation of the product $\zeta_k \omega_k$. It can be seen that fitting a straight line to the plots for the case when noise is added is quite difficult.

2.6 Identifying damage instant

The capability of the DWT in localizing events, in particular discontinuities in time, was illustrated through a simple example in Figure 2.3. Its application in structural health monitoring is shown next where we try to predict the time instant at which a sudden occurrence of damage happens. To illustrate this, the ASCE-SHM benchmark structure was chosen where some braces in the structure were suddenly removed during the motion. To demonstrate this the benchmark structure was excited by random input in the y direction at all the floors (a case outlined for the benchmark problem), and the outputs were collected for 40 second at a sampling frequency of 1000 Hz. The outputs were the floor accelerations in the two horizontal directions at sensor locations as specified in the benchmark problem. At time $t = 20$ sec all braces of the first floor were removed. This simulates the sudden occurrence of damage pattern 1 specified for the benchmark problem. To capture the

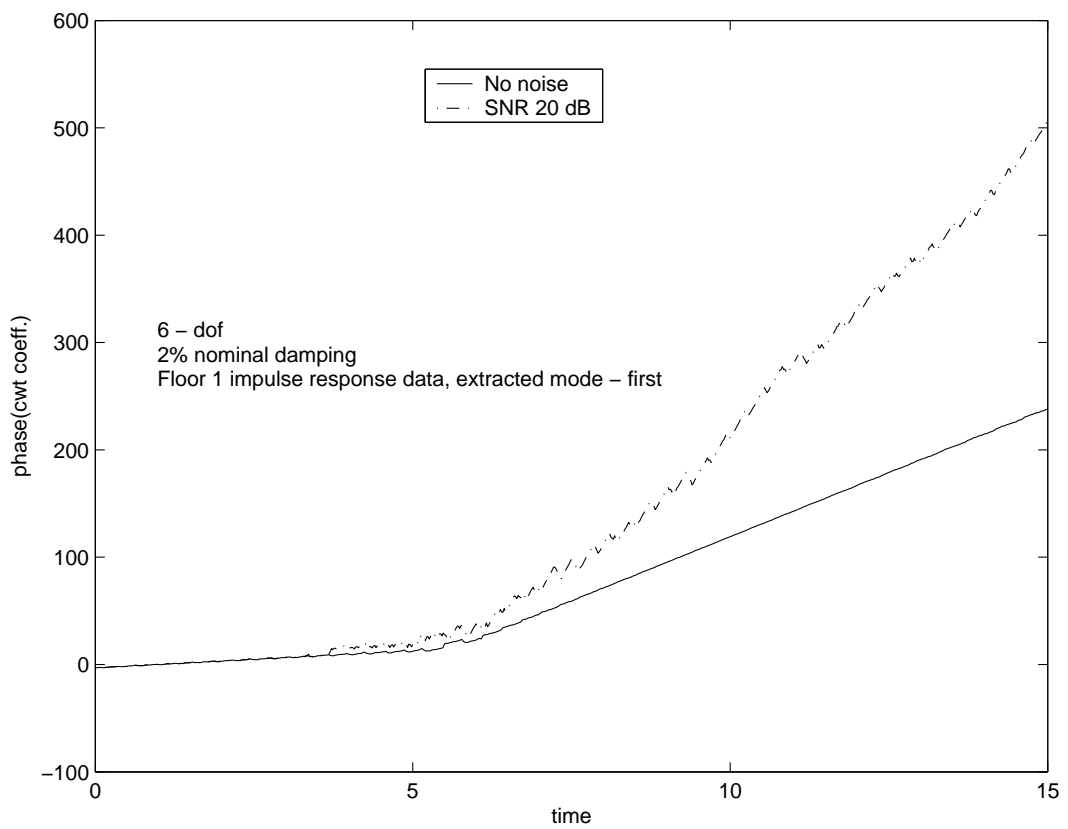


Figure 2.23: Effect of noise on the phase plot

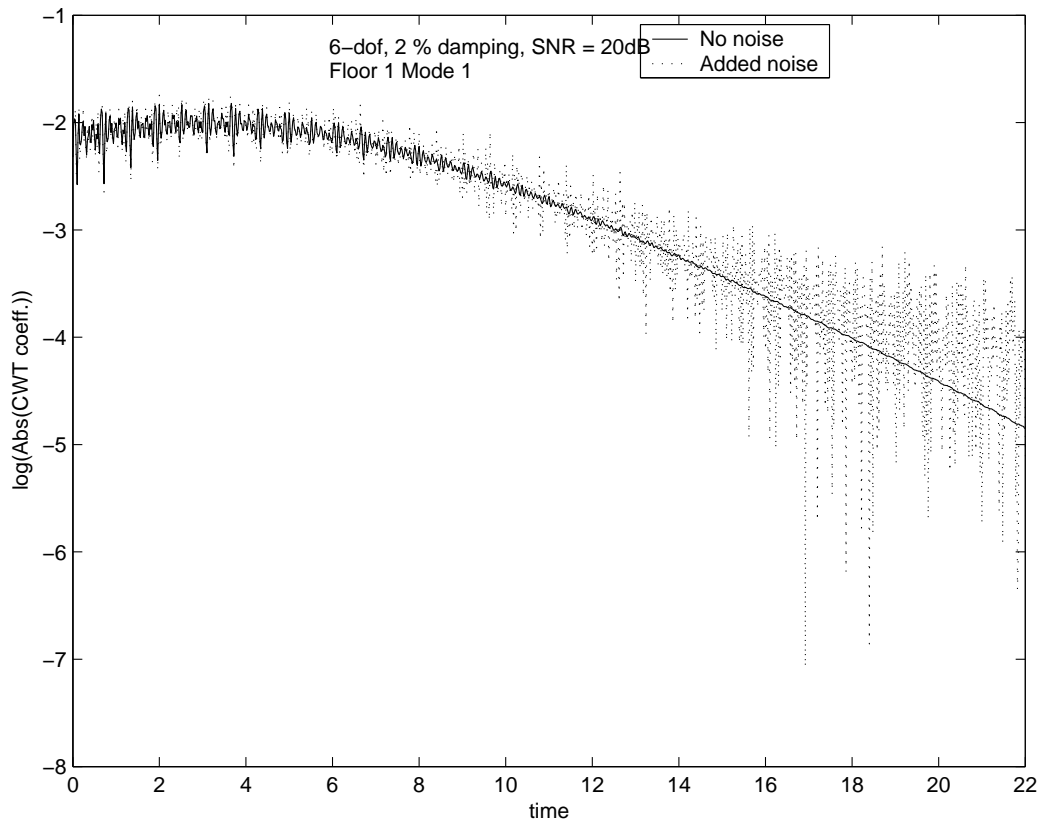


Figure 2.24: $\log(\text{Abs}(CWT \text{ coeff}))$ - $time$ plot for floor 1 mode 1, 6-dof 2%damping, SNR = 20dB

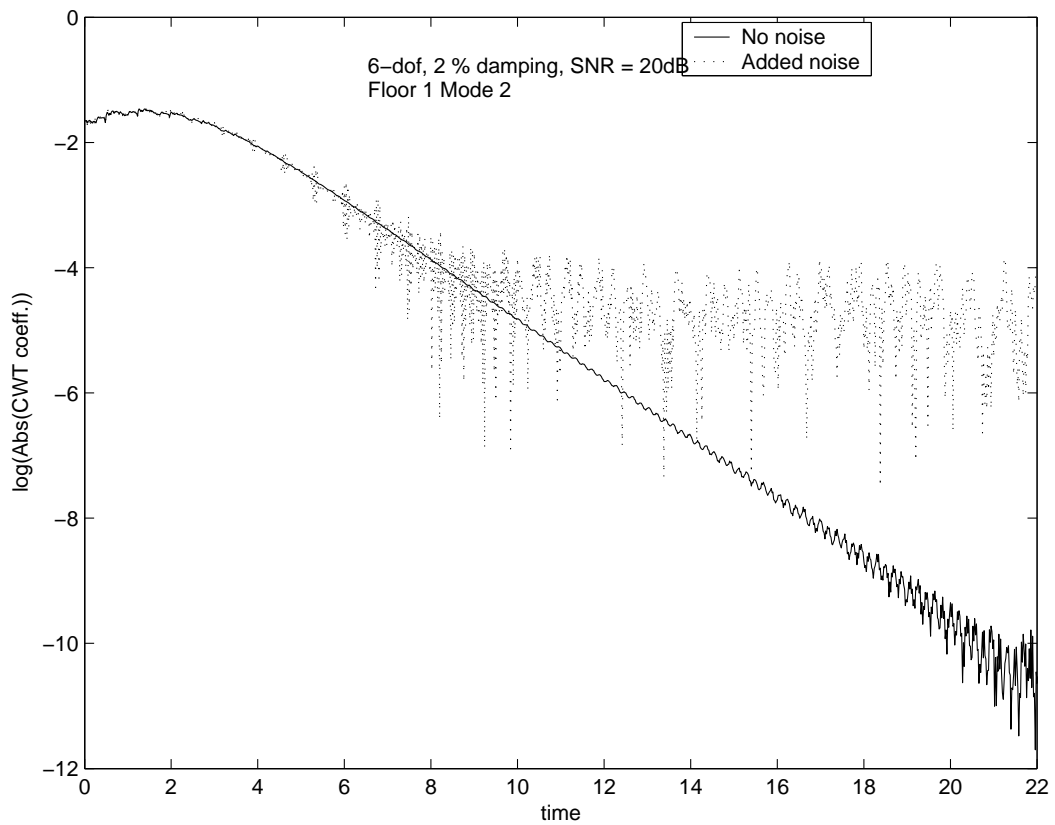


Figure 2.25: $\log(\text{Abs}(\text{CWT coeff}))$ - *time* plot for floor 1 mode 2, 6-dof 2%damping, SNR = 20dB

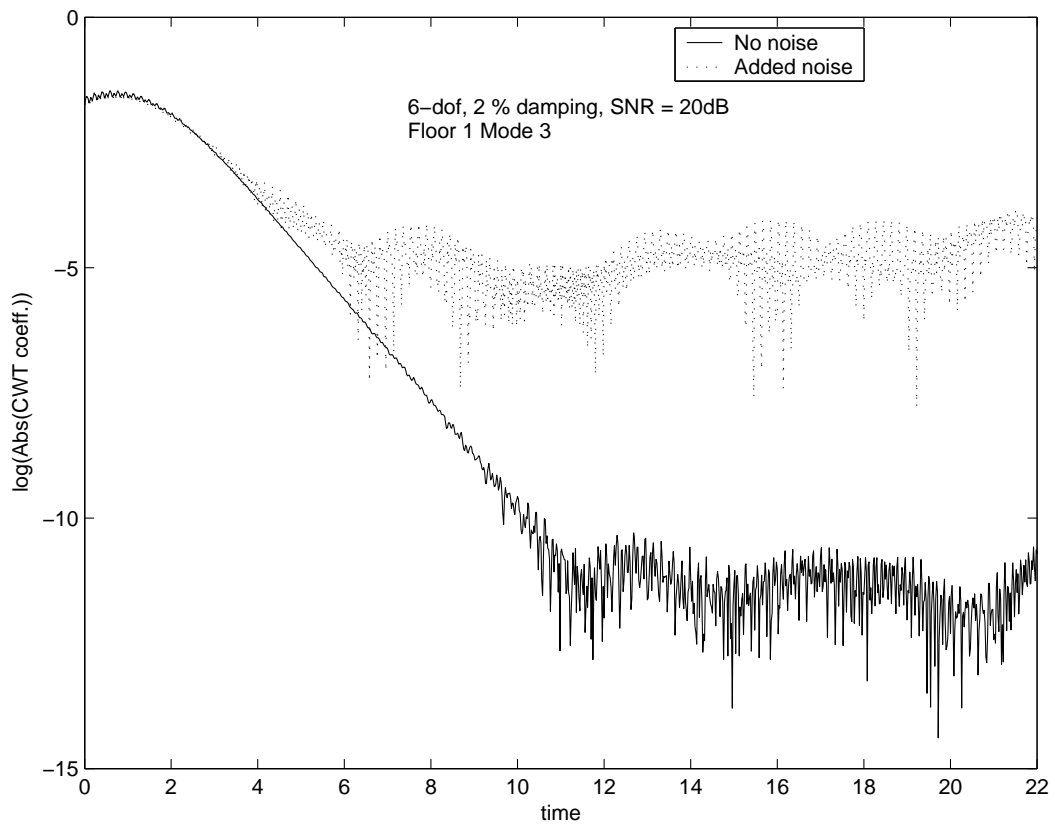


Figure 2.26: $\log(\text{Abs}(\text{CWT coeff}))$ - time plot for floor 1 mode 3, 6-dof 2%damping, SNR = 20dB

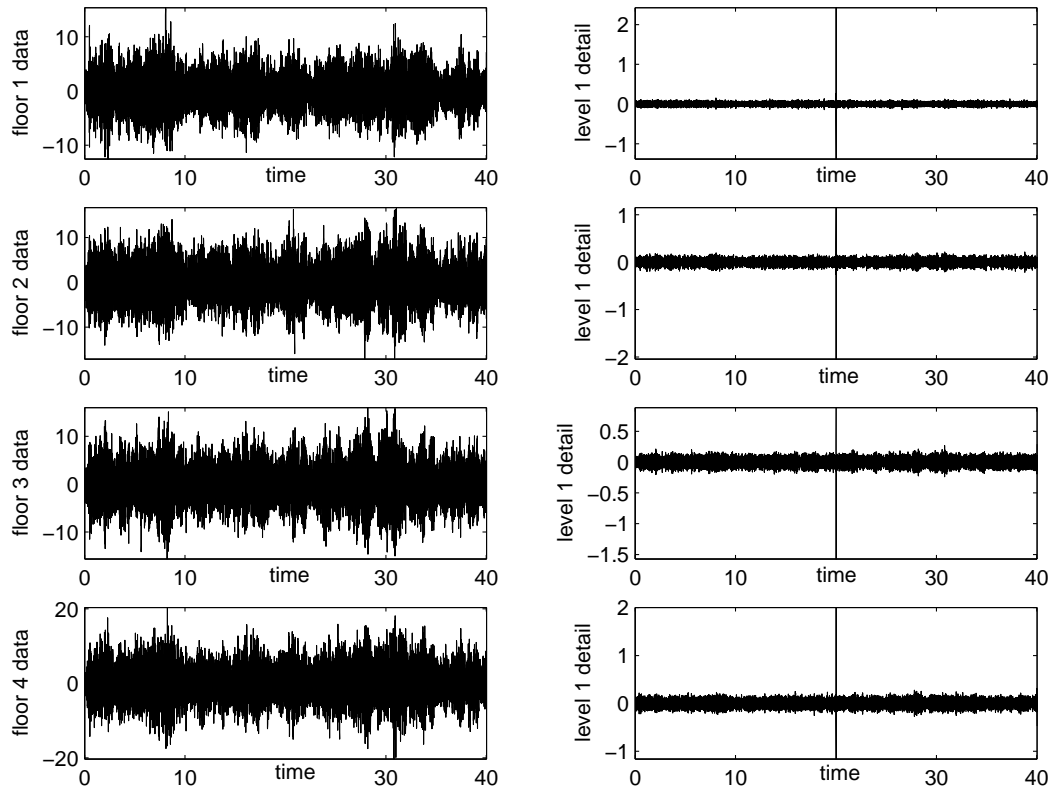


Figure 2.27: Floor acceleration data and the level 1 details using the $DB3$ wavelet, for the benchmark structure

time of this sudden occurrence, the floor accelerations in the y direction were processed by the DWT. The floor accelerations and their respective first level details using the $DB3$ wavelet are shown in Figure 2.27. The time instant of occurrence of the damage can clearly be indicated by the vertical line at $t = 20$ in the level-1 detail plots of the DWT.

2.7 Summary and Conclusions

In this chapter the basic theory of the CWT and the DWT was discussed. Both these transforms have numerous applications. The ability of wavelet transform to separate different frequency components, localize discontinuities and identify evolving frequencies was illustrated through several exam-

ple problems. These abilities of the wavelet transform are of interest in the field of structural health monitoring and damage detection. These applications lead to the use of WT in modal parameter identification which was the main concentration of this chapter.

Through a series of numerical simulations it was shown that the WT can be used for the extraction of modal parameters of a MDOF system. This requires the calculation of the wavelet coefficients at certain scale values and fitting a straight line to the plots of $phase(CWT\ coeff)$ and $log(Abs(CWT\ coeff))$ vs time. The slopes of these straight lines provide the information required for the calculation of modal parameters.

However it was observed that as the damping or the order of the system is increased the identification of higher modes becomes difficult. This can be attributed to the fact that higher modes are many a times not present in the response data and if present they die off quickly. If a mode is not present it can obviously not be detected. Also, if the mode dies off quickly the estimation of the parameters using the two plots mentioned above becomes almost impossible because of the difficulty in fitting a straight line. The Morlet wavelet, which was used for modal parameter estimation in this study, has two adjustable parameters, the central frequency and the bandwidth. It was observed that a proper selection of these parameters is crucial and a proper choice of the parameter value can in better fitting of a straight line in the plots.

In all real applications the data collected has some level of noise. The presence of noise was found to degrades the performance especially because of its effect on the plot of $log(Abs(CWT\ coeff))$. It was observed that in the presence of noise the possible straight line portion is greatly reduced.

The use of DWT to detect the time of occurrence of a damage has been of interest in the field of damage detection. For the ASCE SHM benchmark structure it was shown that the DWT can be used to identify the time instant of damage by looking at the first level details of the floor acceleration records.

Chapter 3

Empirical Mode Decomposition and Hilbert-Huang Transform

3.1 Introduction

In the field of data analysis and signal processing, the Fourier transform in its various forms, is by far the most popular and important method ever developed. However for the time-frequency analysis and the analysis of non-stationary and non-linear time series the first method to gain much popularity was the method of wavelet transform. This method today has found many practical applications. More recently, another method known as the method of *empirical mode decomposition* (EMD) and *Hilbert-Huang transform* (HHT) has been proposed by Huang et. al. (Huang, *et. al.*, 1998) for non-stationary and non-linear time series analysis. This method has gained much popularity and has been explored for its use in various fields. In this chapter a brief introduction to this method is presented and its use in the field of structural health monitoring (SHM) through modal parameter estimation and detecting damage time instances is examined.

3.2 EMD and HHT

The Hilbert transform has been a popular method for estimating natural frequency and damping ratio for various signals. This method can provide good results if the signal being analyzed contains one dominant frequency. For a signal containing several frequencies the method of EMD can be used

to separate different frequency components, and then the method of Hilbert transform can be used to estimate the natural frequency and damping ratio for each separated component.

The EMD method involves the extraction of intrinsic mode functions (IMF's) from a given time series. An IMF is a function which satisfies two conditions (Huang, *et. al.*, 1998) (a) in the whole data set, the number of extrema and the number of zeros crossings must either be equal or differ at most by one, and (b) at any point, the mean value of the envelope defined by the local maxima and the envelope defined by the local minima is zero. It is noted that a harmonic function satisfies these two conditions.

The given time series is processed by a shifting process repeatedly till an IMF is obtained. A new series is then formed by removing this extracted IMF from the original series. This new series again undergoes the shifting process. This process is carried out till all the IMF's have been extracted or till the values of the components become insignificant.

In what follows the basic steps involved in the EMD method for the extraction of IMF's are listed. For the details of the theory and the method involved one can refer to Huang *et. al.*, (1998).

1. Let the given time series be denoted by $x(t)$, and let $i = 1$.
2. Say $X_i(t) = x(t)$.
3. Form an envelope of maximas $max(t)$ and minimas $min(t)$ for $X_i(t)$.
4. Calculate the mean value $m_i(t) = [max(t) - min(t)]/2$.
5. Form the series $h_i(t) = X_i(t) - m_i(t)$.
6. If $h_i(t)$ is an IMF, store it, and set $X_{i+1}(t) = X_i(t) - h_i(t)$, increment i , $i = i + 1$ goto step 3.
Else if $h_i(t)$ is not an IMF use $X_i(t) = h_i(t)$, and goto step 3.

Once all the IMF's have been extracted the process of Hilbert transform may be applied to the IMF's individually, to form analytic signals and to extract instantaneous frequencies and damping ratios. The steps 4 and 5 are referred to as the shifting process.

3.2.1 Comparison to the DWT process

Certain parallels can be drawn between the EMD process used to extract the IMF's and the discrete wavelet transform (DWT) method to form approximations and details of a signal. In the DWT a signal is passed through a high pass and a low pass filter and the results are downsampled by two. The coefficients obtained at the high-pass end form the first level detail, and those at the low-pass end form the first level approximation. This can be said to be the first level of decomposition. This process of filtering can be carried out again on the approximation and be repeated till at the highest level of decomposition just a constant trend is left. The approximations obtained in this process are subsequently smoother versions of the signal, and the details contain the high frequency information.

The process of EMD can be seen as filtering. The original signal undergoes a shifting process till the first IMF is obtained. The first IMF contains the highest frequency component of the signal. Likewise, the first level details in DWT contain the highest frequencies. In EMD a new signal is formed by subtracting the first IMF from the original signal. A similar process is followed in the DWT where the DWT approximation may be defined as the difference of the original signal and its detail. The shifting process in the EMD method is then carried out on the new signal, to obtain the second IMF and so on.

Therefore the process of EMD may be thought of as processing a signal through a filter bank, parallel to DWT, but with its own advantages.

3.2.2 Advantage of the EMD process

One obvious advantage of the EMD process is that it manipulates data only in the time domain, no transformation, and no parameter estimation is involved. Also, since there is no filtering involved in the frequency domain, one is not to be concerned about the issues involving digital filters and is saved the trouble of designing them. By the way it is defined, the EMD process does not require the data to be zero-mean or stationary, it is meant to deal with non-stationary and non-linear time series. In their original work (Huang, *et. al.*, 1998) the authors have also pointed out the advantages of this method over wavelet analysis for time-frequency localization.

3.2.3 The issue of closely spaced frequencies

When modal responses are decomposed using the EMD, ideally the IMF's should contain just single frequencies, corresponding to each mode an IMF would be extracted. But often the EMD process is not able to extract only one mode. This issue has been pointed out by the authors in their original work (Huang, *et. al.*, 1998). To overcome this the use of an '*intermittency criteria*' is suggested (Huang, *et. al.*, 1998).

The intermittency criteria involves filtering the IMF through a digital filter and retaining only those frequency components which are greater than the specified intermittency frequency f_{int} . Another option is to first filter the response around the known modal frequencies and then apply the EMD method on the filtered result. This process however, was not found to be very reliable in several cases examined in our earlier studies (Bisht and Singh, 2004) (Singh and Bisht, 2004). It seems that this requires proper filtering involves the design of optimum filters. The need of using the filters also lessens the the advantages mentioned earlier.

3.2.4 Application to modal parameter estimation

Traditionally the Hilbert transform has been used to form analytic signals and to define the instantaneous frequency (Feldman, 1997; Feldman, 1994a; Feldman, 1994b; Braun and Feldman, 1997). The theoretical basis behind the use of the Hilbert transform and the EMD in modal parameter estimation for MDOF systems can be found in Yang *et. al.*, (2003a, 2003b).

In brief, the method involves separating the modal responses from the available impulse responses and forming the IMF's. The analytic signals are then formed by the application of the Hilbert transform to the individual IMF's. Finally (parallel to the wavelet analysis method) the slope of the *phase-time* plot of the analytic signal provides the damped natural frequency, and the slope of the $\log(Abs(analytic-signal))-time$ plot gives the negative of the product of the natural frequency and damping ratio. The equations needed for calculating the modal parameters are exactly the same as the equations used in the wavelet transform approach (Eq. 2.24 through 2.28), except the Hilbert transform coefficients of the analytical signal are used in place of the wavelet coefficients.

This method was applied to the three and six degrees of freedom structure in the study reported in Bisht and Singh (2004), and Singh and Bisht (2004). It was observed that one could use this method for smaller damping systems. For larger damping system, the extraction of IMF gave problems, and simple filtering of the data as mentioned earlier did not improve the results. The fitting of straight lines to the phase-time and absolute coefficient value-time plots was very difficult as no such trend was clear from the plotted data. In absence of the details about implementing the intermittency criteria, reliable results using this approach could not be obtained. The methods was thus found to be ineffective in determining the modal parameters from the recorded data.

3.2.5 Application to damage time detection

Much like the first level details in the DWT show a sudden spike corresponding to localized discontinuities, the first IMF also shows similar behavior. Thus the IMF can be utilized in identifying damage time instances. In fact, some studies (Xu and Chen, 2004; Yang, *et. al.*, 2004b) have used this approach to detect the occurrence of damage in the ASCE benchmark structure. Herein we show this application by a simple example of a sine wave with frequency 0.5Hz with a small discontinuity in the signal at its midpoint. The signal consisted of 1024 data point and a discontinuity of 0.02 in the amplitude was introduced at the 512th data point. The same example was considered in Chapter to show the effectiveness of the DWT approach in detecting this discontinuity. Figure 3.1 shows four plots. Part (a) of this figure shows the original signal, and Part (b) shows it first IMF obtained by the EMD approach. The first IMF, however, doesn't show any sign of discontinuity, but if this is passed through a high pass filter with cutoff frequency $f_{int} = 5$ Hz the resulting signal shown in (d) clearly shows this discontinuity in the middle of the time axis of this plot. However, the same result could have been obtained by simple filtering of the original signal through a high pass filter with a cutoff frequency of 5Hz. The resulting signal is shown in Part (c) of the figure, which clearly shows the presence of the discontinuity.

Next the damage detection capability of EMD was tested on the ASCE benchmark structure. The structure was excited in one direction with random force, and acceleration response at specified sensor locations were simulated. This simulation was carried out for 40 seconds, and in between the

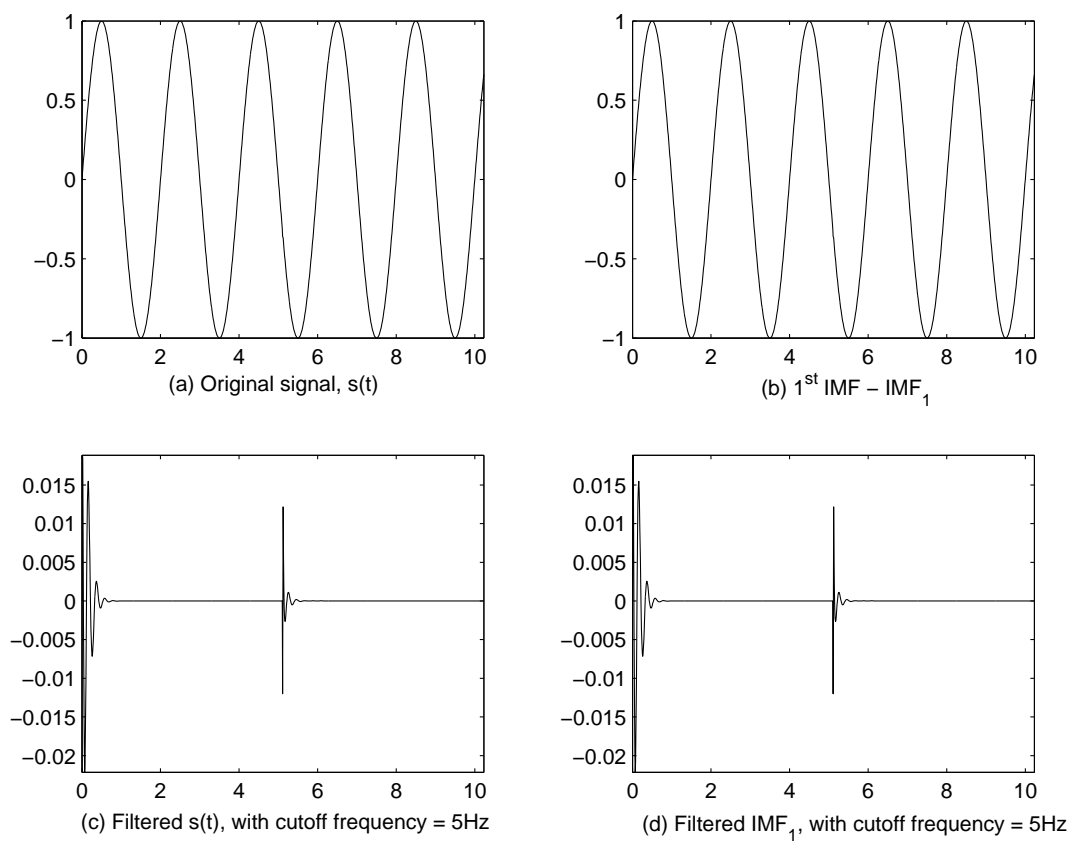


Figure 3.1: A simple signal and its first IMF

structural parameters were changed to simulate the damage pattern 1 as outlined by the ASCE-SHM committee. The result is shown in Figure 3.2. The acceleration response is plotted in (a), and its first IMF in (b). The first IMF itself doesn't indicate any occurrence of damage. However, when this IMF is passed through a high pass filter with a cutoff frequency $f_{int} = 250\text{Hz}$ (value used as in (Yang, *et. al.*, 2004b)) the result is shown in (d). The time of occurrence of the damage now becomes quite evident. However, the same result is obtained again if the acceleration response signal is passed through a high pass filter of the same cutoff frequency $f_{int} = 250\text{Hz}$, as shown in Part (c) of this figure. The use of the EMD-IMF approach for detecting the instant of damage thus seems quite unnecessary when it can be done more simply by the well-established Fourier transform approach.

3.3 Conclusions

The EMD and HHT methods has recently been used in several studies for problems of modal parameter estimation and damage detection in structural systems. The method consists of extracting the modal responses called the intrinsic mode function from the measured input-free response by a numerical filtering procedure known as empirical mode decomposition. Each intrinsic mode function is then used to form an analytic function using the Hilbert transform. The calculated Hilbert transform values for each intrinsic mode function are then used to calculate the corresponding frequencies, damping ratios and relative mode shapes. There are strong similarities in the EMD-HHT method and the wavelet transform method for calculating the modal parameters inasmuch as the same formulas are used to calculate the modal frequencies, damping ratios and mode shapes in the two approach. The extraction of the IMF from the data, however, is sensitive to the filtering process used. In our study, it was found to be difficult to calculate reliable values of the modal parameters because of this filtering problem. The use of this approach has also been suggested for identifying the time instant of occurrence of a damage or sudden changes in a system from a recorded data using the first IMF which contains the highest frequency component. However, it becomes necessary to use high pass filtering with the first IMF to capture the instant of the sudden change. It is observed that a direct high pass filtering of the measured response without any IMF separation is as effective as any other approach for detecting sudden changes in the system

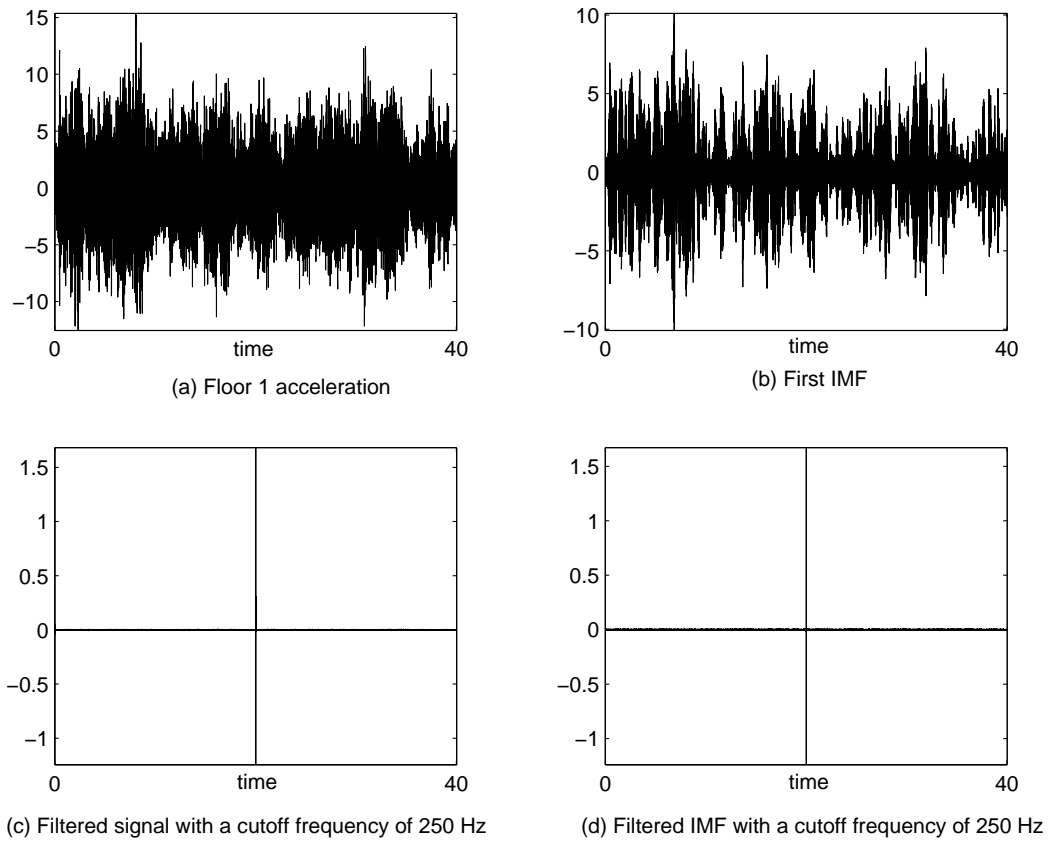


Figure 3.2: Damage detection for the benchmark structure using EMD method.

characteristics.

Chapter 4

Parametric System Identification

4.1 Introduction

In this chapter the method of parametric system identification is used for the estimation of modal parameters of a multi degree of freedom (MDOF) system. The modal parameters of interest are the natural frequency, damping ratio, and mode shapes. Assuming that the acceleration response, and in some cases the input excitation also, are measured and available, certain models are fitted to the data from which the modal parameters are estimated.

The field of system identification deals with the problem of identifying a system. Where “identifying” generally means coming up with a model for the system under consideration. The model might be a mathematical one, describing the input-output relationship of the system, or simply an estimate of the systems step response or the frequency response function. Which type of model to use largely depends on the intended use of the model.

Development of such models is a common practice in several fields of engineering and sciences. Depending on which field it is being used in, having an adequate model for a system can have several advantages. In the field of control engineering it might help in the proper designing of a control mechanism. In the field of finance it can help in predicting future values of some financial index. With respect to the current study such models can be used

to estimate the structural parameters of a MDOF system.

The techniques of system identification can be classified under two broad categories, namely the *parametric system identification* techniques and the *non-parametric system identification* techniques. A common assumption for the methods that fall under either of these categories is that of linearity and time invariance property of the system. Such a system is commonly referred to as a linear time invariant (LTI) system. Any LTI system can be fully described either in the time domain by its impulse response function or in the frequency domain by its frequency response function.

In parametric system identification, the system is described by an assumed linear difference or a differential equation. These equations, or the models for the system, have certain unknown parameters which are to be estimated from the available input-output, or just the output data. A common example is the state-space model where the system is described by a set of differential equations. Such techniques therefore involves the assumption of a model for the system, characterized by certain unknown parameters therefore the name - parametric system identification.

In the non-parametric system identification approach, starting from the LTI assumption and the available input-output data, estimates of the impulse response, step response, frequency response function are formed. No explicit mathematical model describing the system is assumed. Techniques of correlation analysis and Fourier analysis fall under this category.

The general steps of any system identification approach can be outlined as follows

1. Identification of the variables of interest: Understanding which input and output variables are of interest that should be incorporated in the model.
2. Building a model: Development of a mathematical model in terms of a difference equation, differential equation, or simply a block diagram.
3. Estimating the parameters of the model based on practical insight, actual or experimentally collected data.

4. Validation of the model: Making sure that the model captures all the required features.

Once a model is validated it can be used to understand the system behavior especially how changes in certain parameters influence the output, etc.

In the present study, related to structural health monitoring and damage detection (SHM-DD), we are primarily concerned with ways of estimating modal parameters like the natural frequency, damping ratio, and mode shapes for a MDOF systems and detecting structural damage.

The response of a MDOF LTI system can be expressed as a linear difference equation, and the transfer function of a LTI system has the form of a rational function. The modal parameters of a MDOF system can be extracted from the transfer function. With respect to the present study those models that relate the output to the input through some linear difference equation and those that allow the parameterization of the transfer function expressed in a rational form are best suited. Therefore in this study the technique of parametric system identification is used.

In what follows, first some general results related to LTI systems are reviewed, followed by a brief discussion of models used in parametric system identification. The relationship between the modal parameters for a MDOF system and the transfer function is reviewed next. Finally, the results from the numerical study are presented.

4.2 Linear Time Invariant Systems - ARMA Model

LTI systems are those linear systems whose parameter values do not change with time. In this section a general overview of the LTI systems and their response is presented. Further details on this are provided by Ljung (1994, 1987), and Pi and, Pi and Mickleborough (1989c).

An LTI system can be completely described by its impulse response function $g(t)$. If the impulse response function of a LTI system is known, its response to any arbitrary input can be calculated. In the continuous domain

this is represented as,

$$y(t) = \int_{\tau=0}^{\infty} g(\tau)u(t - \tau)d\tau \quad (4.1)$$

where $y(t)$ is the response and $u(t)$ the input to the LTI system. Similarly the response can be represented in the discrete domain as

$$y(t) = \sum_{k=1}^{\infty} g(k)u(t - k) \quad (4.2)$$

where $t = 0,1,2 \dots$

Parallel to the impulse response function in the time domain, a system can be characterized by its transfer function in various forms, for example in the frequency domain, the s -plane or in the z -plane. For the discrete case using the shift operator q , (defined as $x(t - k) = q^{-k}x(t)$), Eq. 4.2 can be written as,

$$y(t) = \sum_{k=1}^{\infty} g(k)u(t)q^{-k} = G(q)u(t) \quad (4.3)$$

where,

$$G(q) = \sum_{k=1}^{\infty} g(k)q^{-k} \quad (4.4)$$

$G(q)$ is called the transfer function of the system. In particular when $q = e^{i\omega}$ the complex valued function $G(e^{i\omega})$ for $-\pi \leq \omega \leq \pi$, is called the frequency response function.

Of special interest in this study are the multi-degree of freedom dynamic systems. For such a dynamic system with n degree of freedom (DOF) the equation of motion can be written as

$$\mathbf{M}\ddot{\eta}(t) + \mathbf{D}\dot{\eta}(t) + \mathbf{K}\eta(t) = \mathbf{f}(t) \quad (4.5)$$

where \mathbf{M} , \mathbf{D} , \mathbf{K} are the $n \times n$ mass damping and stiffness matrix, and η and \mathbf{f} are the $n \times 1$ output and input vectors respectively. The above equation can be represented in the state space form as

$$\dot{\mathbf{x}}(t) = \mathbf{A}\mathbf{x}(t) + \mathbf{B}\mathbf{f}(t) \quad (4.6)$$

$$\mathbf{y}(t) = \mathbf{C}\mathbf{x}(t) \quad (4.7)$$

where \mathbf{A} is called the system matrix, \mathbf{x} the state vector and \mathbf{y} the measurement vector. These matrices can be defined in terms of the \mathbf{M} , \mathbf{D} , and \mathbf{K} matrices as follows,

$$\mathbf{x}(t) = \begin{Bmatrix} \eta(t) \\ \dot{\eta}(t) \end{Bmatrix}$$

$$\mathbf{A} = \begin{bmatrix} \mathbf{0} & \mathbf{I} \\ -\mathbf{M}^{-1}\mathbf{K} & -\mathbf{M}^{-1}\mathbf{D} \end{bmatrix}$$

$$\mathbf{B} = \begin{bmatrix} \mathbf{0} \\ -\mathbf{M}^{-1} \end{bmatrix}$$

Using the concept of transition matrix Φ the response of such a system at any time can be expressed as

$$\mathbf{x}(t) = \Phi(t)\mathbf{x}(0) + \int_0^t \Phi(t-\tau)\mathbf{B}\mathbf{f}(\tau)d\tau \quad (4.8)$$

In the discrete domain, for a sampling time step of T setting

$$\Delta = \int_0^T \Phi(t-\tau)\mathbf{B}d\tau \quad (4.9)$$

the equation in the discrete domain for time $t = kT$, becomes

$$\mathbf{x}(k+1) = \Phi\mathbf{x}(k) + \Delta\mathbf{f}(k) \quad (4.10)$$

Taking the z -transform of the above equation

$$z\hat{\mathbf{x}}(z) - z\mathbf{x}(0) = \Phi\hat{\mathbf{x}}(z) + \Delta\hat{\mathbf{f}}(z)$$

$$[z\mathbf{I} - \Phi]\hat{\mathbf{x}}(z) = z\mathbf{x}(0) + \Delta\hat{\mathbf{f}}(z)$$

$$\hat{\mathbf{x}}(z) = [z\mathbf{I} - \Phi]^{-1}\{z\mathbf{x}(0) + \Delta\hat{\mathbf{f}}(z)\} \quad (4.11)$$

Similarly taking the z -transform of the measurement equation

$$\hat{\mathbf{y}}(z) = \mathbf{C}\hat{\mathbf{x}}(z) \quad (4.12)$$

Assuming zero initial condition and using the expression for the z -transform of \mathbf{x}

$$\hat{\mathbf{y}}(z) = \mathbf{C}[z\mathbf{I} - \Phi]^{-1}\Delta\hat{\mathbf{f}}(z) \quad (4.13)$$

or

$$\hat{\mathbf{y}}(z) = \mathbf{H}(z)\hat{\mathbf{f}}(z) \quad (4.14)$$

where $\mathbf{H}(z)$ is the z -transfer function of the system defined as,

$$\mathbf{H}(z) = \mathbf{C}[z\mathbf{I} - \mathbf{\Phi}]^{-1}\mathbf{\Delta} \quad (4.15)$$

expressing the inverse of the matrix in equation 4.15 as

$$[z\mathbf{I} - \mathbf{\Phi}]^{-1} = \frac{adj[z\mathbf{I} - \mathbf{\Phi}]}{det[z\mathbf{I} - \mathbf{\Phi}]}$$

where

$$adj[z\mathbf{I} - \mathbf{\Phi}] = \mathbf{G}_1 z^{2n-1} + \mathbf{G}_2 z^{2n-2} + \dots + \mathbf{G}_{2n}$$

and

$$det[z\mathbf{I} - \mathbf{\Phi}] = z^{2n} + a_1 z^{2n-1} + \dots + a_{2n}$$

the z -transfer function in equation 4.15 can be expressed as

$$\mathbf{H}(z) = \frac{\mathbf{H}_1 z^{2n-1} + \mathbf{H}_2 z^{2n-2} + \dots + \mathbf{H}_{2n}}{z^{2n} + a_1 z^{2n-1} + \dots + a_{2n}} \quad (4.16)$$

where

$$\mathbf{H}_i = \mathbf{C}\mathbf{G}_i\mathbf{\Delta} \quad (4.17)$$

From eq. 4.14

$$\hat{\mathbf{y}}(z) = \frac{\mathbf{H}_1 z^{2n-1} + \mathbf{H}_2 z^{2n-2} + \dots + \mathbf{H}_{2n}}{z^{2n} + a_1 z^{2n-1} + \dots + a_{2n}} \hat{\mathbf{f}}(z) \quad (4.18)$$

using the shift property of the z operator, we obtain

$$\mathbf{y}(k) + a_1 \mathbf{y}(k-1) + \dots + a_{2n} \mathbf{y}(k-2n) = \mathbf{H}_1 \mathbf{f}(k-1) + \dots + \mathbf{H}_{2n} \mathbf{f}(k-2n) \quad (4.19)$$

From the above equation it can be seen that the response of a LTI system at time t can be written as a linear difference equation involving previous response and input values. Therefore the response of a LTI system can be represented as an auto-regression moving-average (ARMA) model. For the case of a single output or measured response the above equation simplifies to,

$$y(k) + a_1 y(k-1) + \dots + a_{2n} y(k-2n) = b_1 f(k-1) + \dots + b_{2n} f(k-2n) \quad (4.20)$$

using the notation

$$A(q) = 1 + a_1q^{-1} + \dots + a_{2n}q^{-2n} \quad (4.21)$$

$$B(q) = b_1q^{-1} + \dots + b_{2n}q^{-2n} \quad (4.22)$$

involving the shift operator q , the equation can be further written in a compact form as

$$A(q)y(t) = B(q)f(t) \quad (4.23)$$

Which is the more commonly known form of the ARMA model. Strictly speaking, Eq.4.23 represents an ARMA model only when $f(t)$ is white noise. If $f(t)$ is not white noise this model is referred to as the auto-regression exogenous input (ARX) model. This is further clarified in the following section.

4.3 Parametric System Identification

The Equations 4.20 and 4.23 provide the basis for considering various regression models under parametric system identification, to describe the LTI system. In all practical situations the measurements that are available are corrupted with some level of noise. Alternatively, when a model is fitted to the input-output data, exact representation may not be possible. The part which is not reproduced by the model can be considered as the error or the noise term. This can be incorporated in the model as,

$$A(q)y(t) = B(q)f(t) + e(t) \quad (4.24)$$

where $e(t)$ represents the error or noise term. In this section various parametric models, and methods for their parameter estimation are introduced. Detail information on these topics may be found in Ljung (1987).

4.3.1 Parametric models

Using the system identification terminology, let the output be $y(t)$, input be $u(t)$ and the error or noise term be $e(t)$. Using the notations as defined in 4.21, 4.22 and further defining

$$C(q) = 1 + c_1 + q^{-1} + \dots + c_{n_c}q^{-n_c} \quad (4.25)$$

$$F(q) = 1 + f_1 + q^{-1} + \dots + f_{n_f}q^{-n_f} \quad (4.26)$$

$$D(q) = 1 + d_1 + q^{-1} + \dots + d_{n_d}q^{-n_d} \quad (4.27)$$

some of the commonly used transfer function models (models where the transfer function is parameterized) in parametric system identification are,

1. AR model: An auto-regression (AR) model is represented by

$$y(k) + a_1y(k-1) + \dots + a_py(k-p) = e(t) \quad (4.28)$$

$$A(q)y(k) = e(t)$$

In this representation the output at any time is represented as a linear combination of previous outputs and the noise term.

2. MA model: A moving-average (MA) model is represented by

$$y(k) = e(k) + c_1e(k-1) + \dots + c_pe(k-p) \quad (4.29)$$

$$y(k) = C(q)e(k)$$

where the output at anytime is a linear combination of the noise terms.

3. ARMA model: An ARMA model is represented as

$$y(k) + a_1y(k-1) + \dots + a_{n_a}y(k-n_a) = e(k) + c_1e(k-1) + \dots + c_{n_c}e(k-n_c) \quad (4.30)$$

$$A(q)y(t) = C(q)e(t)$$

where the output at anytime is a linear combination of previous output and noise terms.

4. ARX model: An auto-regression exogenous input (ARX) model is represented by

$$y(k) + a_1y(k-1) + \dots + a_{n_a}y(k-n_a) = b_1u(k-1) + \dots + b_{n_b}u(k-n_b) + e(t) \quad (4.31)$$

$$A(q)y(t) = B(q)u(t) + e(t)$$

where the output at anytime is a linear combination of previous outputs, previous inputs, and the noise terms.

5. Output error model: Suppose the input and no-noise corrupted output are related by,

$$w(t) + f_1w(t-1) + \dots + f_{n_f}w(t-n_f) = b_1u(k-1) + \dots + b_{n_b}u(k-n_b) \quad (4.32)$$

Because of the noise the observed output would be

$$y(t) = w(t) + e(t) \quad (4.33)$$

$$y(t) = \frac{B(q)}{F(q)}u(t) + e(t) \quad (4.34)$$

the above equations represent the output-error (OE) model.

6. Box-Jenkins model: Its a further generalization of the OE model and is represented as

$$y(t) = \frac{B(q)}{F(q)}u(t) + \frac{C(q)}{D(q)}e(t) \quad (4.35)$$

The above mentioned models, and several other models, can be represented in the following general form,

$$A(q)y(t) = \frac{B(q)}{F(q)}u(t) + \frac{C(q)}{D(q)}e(t) \quad (4.36)$$

Different models can be realized based on the polynomials used. These models are also referred to as the transfer function models since it is the transfer functions which is being defined in their identification.

4.3.2 Estimation of parameters

Once a particular model has been selected, the next important step involves the estimation of its parameters, that is, the coefficients of $A(q)$, $B(q)$ etc. The approaches that are commonly used for parameter estimation are the: *Prediction Error Minimization* (PEM) approach and the *Correlation Approach*, in particular the *Instrumental-Variable* (IV) method.

In the PEM method a good model is one which minimizes a norm (usually mean square norm) of the error between the measured response and the response predicted from the model. Methods that are commonly used under the PEM are those of linear regressions, least square and maximum likelihood. For details see Ljung, (1987).

In the correlation approach (and the IV method) the requirement of a good model is that the error or the noise term at any time be uncorrelated with the past measurements (Ljung, 1987). In this study the PEM method was used in estimating the parameters of the models.

4.4 Identification of Modal Quantities

Once the parameters of the auto regressive models are calculated, the modal quantities like frequencies, damping ratios, and mode shapes can be identified as follows. As shown previously the response of a n-DOF LTI system can be represented in the form of a ARX model. Including the error or noise term the equation can be written as,

$$A(z)y(t) = B(z)u(t) + C(z)e(t) \quad (4.37)$$

The transfer function of this model is given by,

$$H(z) = \frac{B(z)}{A(z)} = \frac{b_1z^{-1} + b_2z^{-2} + b_3z^{-3} + \dots + b_{2n}z^{-2n}}{1 + a_1z^{-1} + a_2z^{-1} + \dots + a_{2n}z^{-2n}} \quad (4.38)$$

The poles of the transfer function are the roots of the polynomial $A(z)$, and the zeros of the transfer function are the roots of $B(z)$. As shown previously $A(z)$ is obtained from $\det[z\mathbf{I} - \mathbf{\Phi}]$. Thus the roots of $A(z)$ are the solutions of $\det[z\mathbf{I} - \mathbf{\Phi}] = 0$, which is precisely the equation for calculating the eigen values of the transition matrix, $\mathbf{\Phi}$, of the LTI system. The eigen values of the transition matrix $\mathbf{\Phi}$ are, however, known to be equal to $e^{(-\zeta_k\omega_k + i\omega_{dk})T}$. Therefore the roots of $A(z)$ herein denoted by α_k 's or the poles of $H(z)$ and the modal parameters are related as follows:

$$\alpha_i = e^{(-\zeta_k\omega_k + i\omega_{dk})T} \quad (4.39)$$

where ζ_k , ω_k , and ω_{dk} are the damping ratio, natural frequency and the damped natural frequency of the k^{th} mode. From this equation, the modal frequencies and damping ratios can be calculated as follows:

$$\ln(\alpha_i) = -\zeta_k\omega_kT + i\omega_{dk}T \quad \ln(\alpha_i^*) = -\zeta_k\omega_kT - i\omega_{dk}T$$

$$\omega_k = \frac{\sqrt{\ln(\alpha_i)\ln(\alpha_i^*)}}{T} \quad (4.40)$$

$$\zeta_k = \frac{-(\ln(\alpha_i) + \ln(\alpha_i^*))}{2\omega_kT} \quad (4.41)$$

To calculate the modeshape values, one needs to express the transfer function in the following partial fraction form,

$$H(z) = \sum_{k=1}^n \frac{A}{1 - \alpha_k z^{-1}} + \frac{A^*}{1 - \alpha_k^* z^{-1}} \quad (4.42)$$

Knowing the complex numbers A , one can calculate the mode shape values for each mode. The ratio of the absolute value of the complex number A evaluated at two different DOF gives the ratio of the mode shape. The relative sign of the mode shape values can be evaluated based on the phase of A at the two DOF.

4.5 Numerical results

In this section we now present some numerical results obtained by the approach described above for the model parameters of the three structures considered in the previous chapters. First, the results for the case of no-noise are presented, followed by the results for the case when the measured floor accelerations are corrupted with noise. In both the cases the measurements were assumed to be the ground acceleration, and the simulated floor acceleration.

4.5.1 No-noise

From the discussion of sections 4.2 and 4.4 it can be seen that if natural frequency and damping ratio are the only parameters of concern, then for a n -DOF system, an $AR(2n)$ model fitted to the response data is sufficient. The transfer function of the AR model is an all-poles function and the natural frequency and damping ratio can be obtained from Eq. 4.39. To obtain any information about the mode shapes however, an $ARMA(2n, 2n - 1)$, or a model structure which allow for the pole-zero representation of the transfer function must be used.

For all the cases of simulation in which the structure was assumed to be exposed to earthquake excitation, the ARX model was used. Unlike the case of wavelet analysis, all the modal parameters were accurately identified for all the modes. The issue of higher damping and higher modes dying off quickly was not a problem in the identification of modal parameters, as was found in the case of wavelet analysis. Figure 4.1 shows the identified mode shapes for the 6-DOF system with 10% nominal damping. Since all the results were found to be exact, the results for other damping ratios are thus not presented.

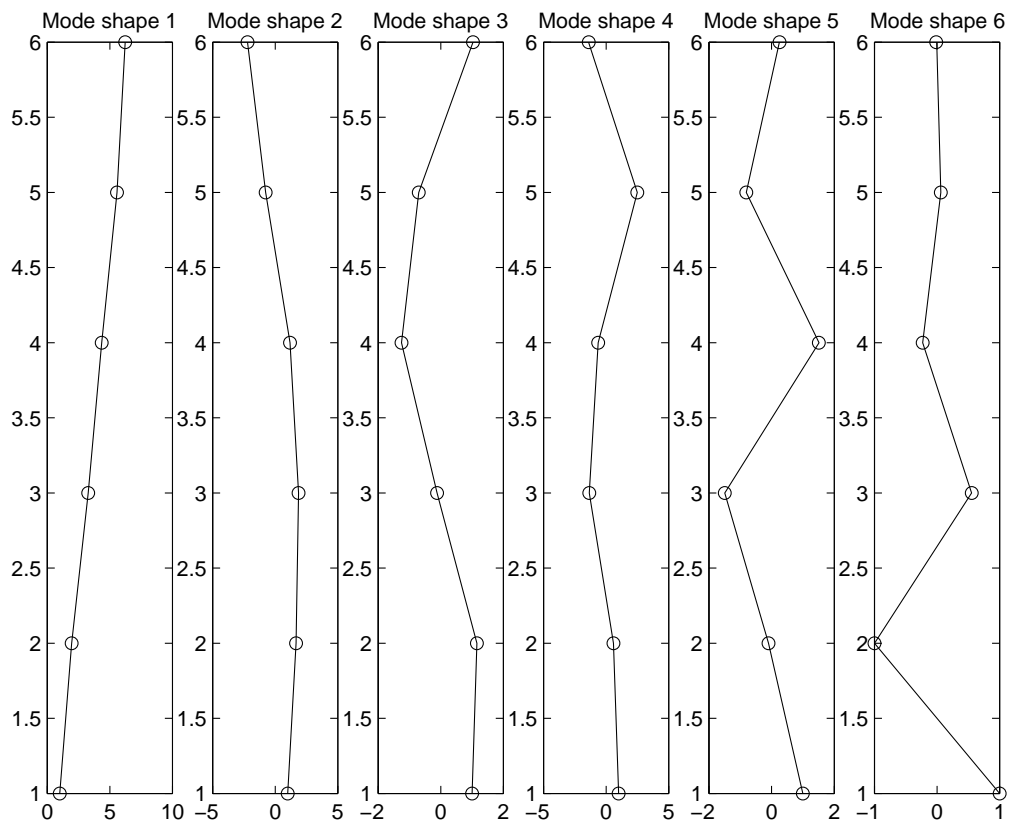


Figure 4.1: Actual and identified mode shapes from the 6-DOF system, 10% nominal damping, using ARMA(13,12) model. \circ - actual values

4.5.2 Noisy data

Having obtained exact results for the case of no-noise, the efficiency of these models are next tested for the case when the floor accelerations are corrupted with noise. Like in the case of wavelet analysis, the efficiency of this method was found to degrade. Even for small signal-to-noise ratios, model orders much larger than $2n$ had to be used to allow for the convergence of the modal values. This is illustrated for the case of the 6-DOF system.

For the 6-DOF system, Figure 4.2 shows the pole-zero plot for the ARX(13,13) model fitted to the first floor acceleration for the case of no-noise. In this figure, all six poles can be identified and they correspond to the exact modal parameters. However, when the data is corrupted by noise and the same order model is used, then the poles obtained from the noisy data do not correspond to those from the no-noise case. This is shown in pole-zero plot in Figure 4.3 Therefore the minimum order ARX(13,13) model which was adequate for the no-noise case would not now be adequate to give the correct structural natural frequencies and damping ratios. A large model is needed to get more averaging point to reduce the effect of the noise in the data.

To show the effect of using a large order model, we present Figure 4.4 giving a quarter of the pole-zero plot for an ARX(40,40) model fitted to the same noisy data. Here the convergence to some of the actual poles can now be seen, specially for the lower modes. However, increasing the model order has its own disadvantage. When the model order is increased spurious poles and zeros are also introduced which makes it difficult to identify the true poles and zeros of the system. In the following we examine an approach that can be used to identify the correct poles and zeros, and discard those that are introduced by the use of a higher order model.

To examine the characteristics of the spurious poles that are added in the model, here we conduct a study with increasing order model used for the 6-DOF structure with 5% nominal damping and its floor acceleration data corrupted by an addition of noise (SNR 20dB). Since we are only interested in examining the convergence to the modal frequencies and damping ratios which can be obtained from the poles, here we only work with the ARMA model as the use of ARMA model is adequate for this purpose, and also

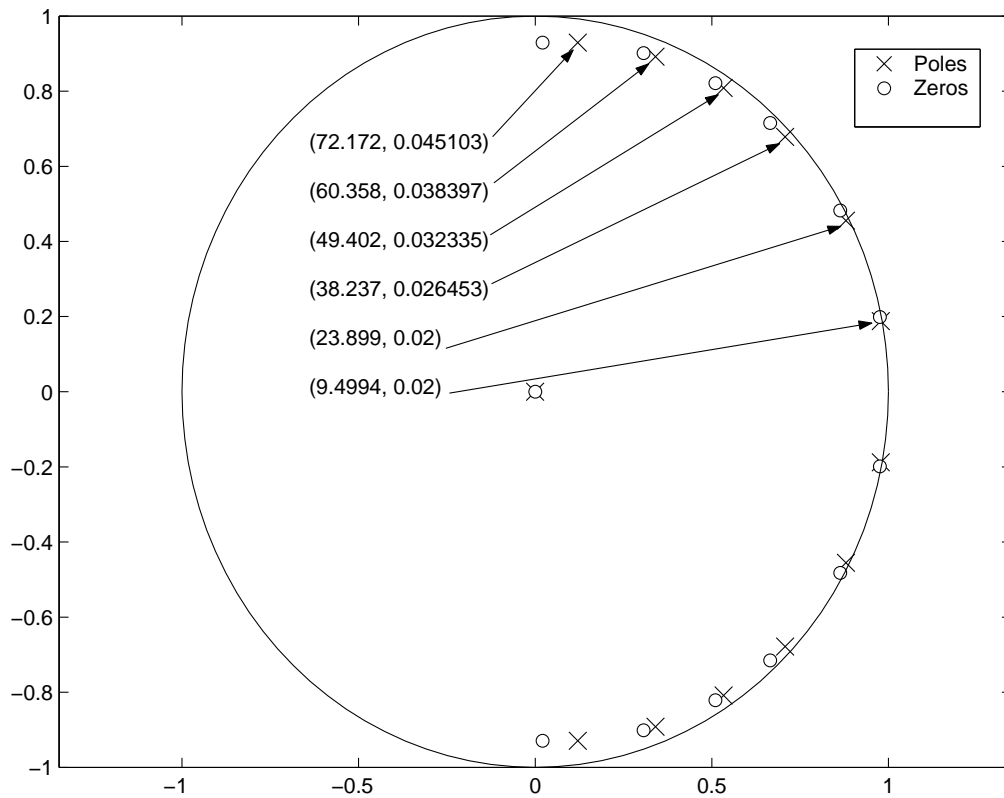


Figure 4.2: Pole-zero plot for the ARX model fitted to the acceleration response at floor 1. The numbers in the bracket show the natural frequency (in rad/sec) and damping ratio corresponding to each pole.

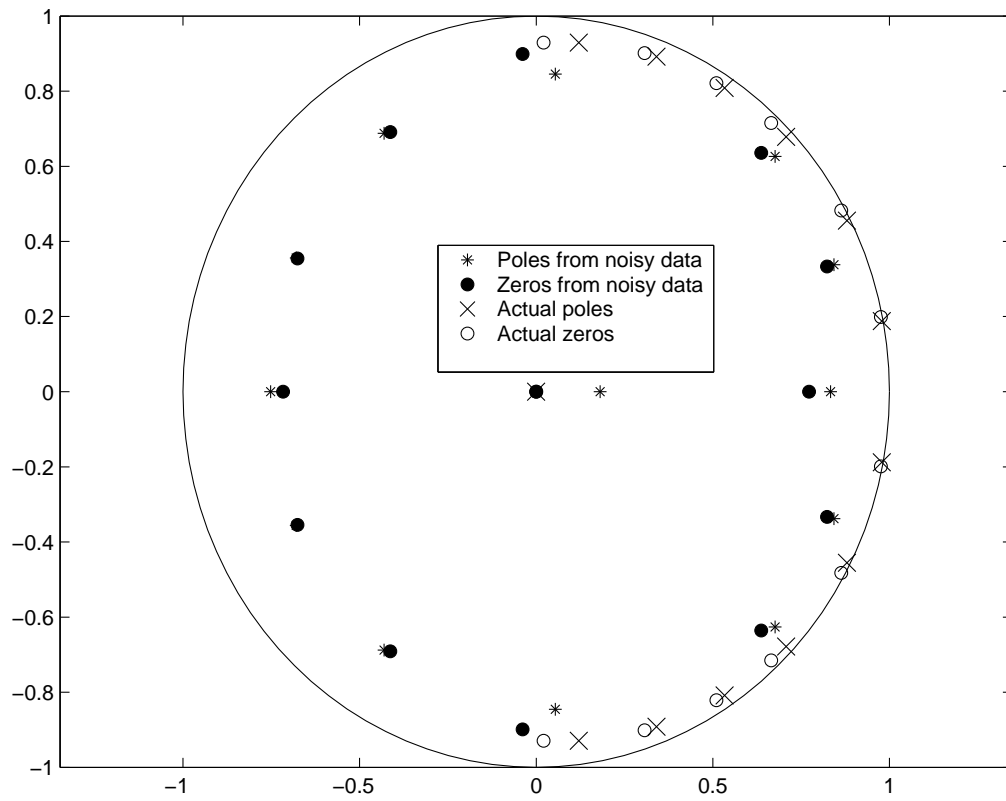


Figure 4.3: Pole-zero plot for the ARX model fitted to the noisy acceleration response at floor 1 (model order 13,13), along with the actual poles and zeros as identified from the no-noise case.

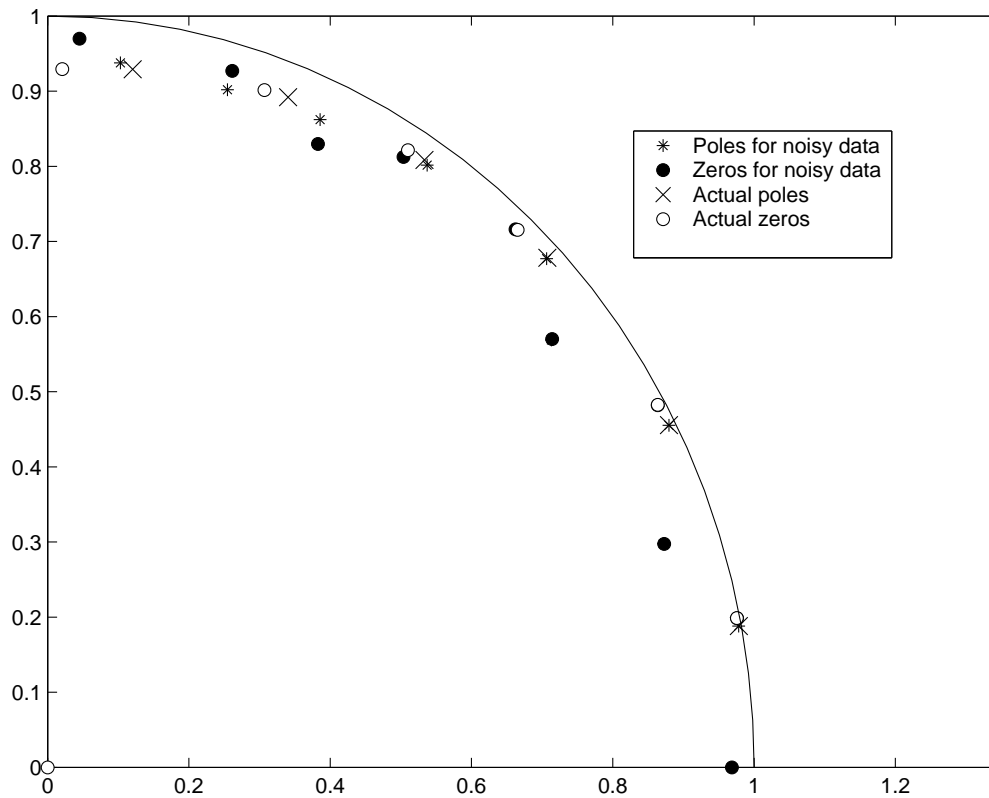


Figure 4.4: Pole-zero plot for the ARX model fitted to the noisy acceleration response at floor 1 (model order 40,40), along with the actual poles and zeros as identified from the no-noise case.

because a computationally efficient approach known as Steiglitz McBride algorithm (Steiglitz and McBride, 1965) is available to carry out the computations. To work with this model, first the impulse response function from the acceleration response and the input is generated. This impulse response function when generated with no-noise data will give the exact nodal parameters even with the smallest permissible ARMA model. In Table 4.1 these modal parameters calculated with the smallest permissible model, ARMA(13,12) are shown.

Next we use this ARMA algorithm to calculate the poles from the data corrupted by the noise. The ARMA(n,n-1) models for increasing $n = 13, 26, 39, 52, 65$ and 78 , were used to examine the convergence to the true system poles. These results are presented in in Tables 4.2-4.7. They show the admissible poles, and corresponding natural frequencies and damping ratios. Admissible poles refers to those poles that occur in complex conjugate pairs, and correspond to $\omega \leq 100$ rad/sec. The limit on ω can easily be estimated from the discrete Fourier transform plot. Knowing the exact values of the frequencies and damping ratios, we also indicate the damping values that are either very low or very high in the table columns entitled "Damping". The term "Very low" and "Very high" refer to values of damping ratios that are less than 1% and greater than 20% respectively. Again knowing the correct values of the frequencies, we note that as the model order is increased the poles do seem to converge and the modal values tend to approach the actual ones. Based on these certain observations can be made as the model order is increased.

1. If the identified natural frequencies are arranged in an ascending order the structural frequencies are most likely to be a first few ones. For large models, we can also get some values lower than the structural frequencies, but that are invariably associated with very high damping values. (Table 4.5 4.6 and 4.7).
2. The true modes or the structural frequencies tend to appear repeatedly in subsequent higher order models, for example the modes with frequencies around 9.5 and 23.9 appear in all the tables.

The convergence to the true frequencies is not immediately apparent from the tables. This observation, however, can be improved by using a stabilization diagram (Peeters, 2000) where one compares the changes in frequencies,

Table 4.1: Parameters from ARMA(13,12) model for the case of no noisy

Poles	ω_n (rad/sec)	ζ
0.97277 - 0.18683i	9.4994	0.05
0.86723 - 0.4486i	23.899	0.05
0.68709 - 0.65705i	38.237	0.066132
0.51058 - 0.7692i	49.402	0.080838
0.32139 - 0.83057i	60.358	0.095992
0.11569 - 0.84189i	72.172	0.11276

Table 4.2: Parameters from ARMA(13,12) model for noisy data

Poles	ω_n (rad/sec)	ζ	Damping
0.86169 - 0.44989i	24.1	0.058781	
0.63648 - 0.54547i	36.509	0.24165	Very high
0.018195 - 0.81635i	78.086	0.12977	

Table 4.3: Parameters from ARMA(26,25) model for noisy data

Poles	ω_n (rad/sec)	ζ	Damping
0.97033 - 0.18585i	9.4813	0.06383	
0.85961 - 0.44525i	23.951	0.067729	
0.67006 - 0.6155i	37.448	0.12615	
0.40967 - 0.91123i	57.415	0.00079493	Very low
0.22904 - 0.95192i	66.742	0.015833	
0.042147 - 0.99892i	76.431	0.00012753	Very low

Table 4.4: Parameters from ARMA(39,38) model for noisy data

Poles	ω_n (rad/sec)	ζ	Damping
0.97251 - 0.1867i	9.4962	0.051499	
0.86564 - 0.4484i	23.931	0.053133	
0.67754 - 0.66343i	38.835	0.068394	
0.57455 - 0.6683i	43.496	0.14521	
0.41066 - 0.91149i	57.375	0.00023753	Very low
0.1992 - 0.87933i	67.6	0.076611	

Table 4.5: Parameters from ARMA(52,51) model for noisy data

Poles	ω_n (rad/sec)	ζ	Damping
0.9989 - 0.0050689i	0.25953	0.21028	Very high
0.9727 - 0.18721i	9.519	0.049855	
0.86721 - 0.44946i	23.937	0.049107	
0.74934 - 0.65516i	35.923	0.0064623	Very low
0.68749 - 0.6639i	38.464	0.05887	
0.43677 - 0.23343i	42.858	0.81983	Very high
0.46233 - 0.8502i	53.661	0.030523	
0.41077 - 0.91148i	57.37	0.00020252	Very low
0.27387 - 0.43575i	60.429	0.54959	Very high
0.2521 - 0.96754i	65.795	0.00011486	Very low
.22514 - 0.9476i	66.89	0.019712	
0.021334 - 0.87877i	77.594	0.083085	

Table 4.6: Parameters from ARMA(65,64) model for noisy data

Poles	ω_n (rad/sec)	ζ	Damping
0.99855 - 0.0051241i	0.2664	0.26912	Very high
0.9726 - 0.18702i	9.5104	0.0506	
0.93513 - 0.35393i	18.091	0.00036625	Very low
0.86649 - 0.44906i	23.938	0.050864	
0.77007 - 0.63186i	34.357	0.0056658	Very low
0.68765 - 0.65772i	38.238	0.064938	
0.70315 - 0.70179i	39.223	0.0083928	Very low
0.44004 - 0.6927i	51.206	0.193	
0.49422 - 0.86386i	52.558	0.004538	Very low
0.4107 - 0.91135i	57.37	0.00033218	Very low
0.28555 - 0.94402i	63.857	0.010831	
0.25225 - 0.96752i	65.788	0.00010289	Very low
0.21261 - 0.95466i	67.592	0.016423	
0.0068787 - 0.99387i	78.194	0.0039147	Very low

Table 4.7: Parameters from ARMA(78,77) model for noisy data

Poles	ω_n (rad/sec)	ζ	Damping
0.99813 - 0.0078772i	0.40513	0.22666	Very high
0.97282 - 0.18717i	9.5155	0.049309	
0.86706 - 0.4492i	23.93	0.049661	
0.79735 - 0.58037i	31.467	0.022071	
0.75571 - 0.64661i	35.389	0.0076745	Very low
0.6842 - 0.65938i	38.431	0.066437	
0.69487 - 0.71621i	40.026	0.0026266	Very low
0.50486 - 0.69479i	47.731	0.1594	
0.48818 - 0.86949i	52.96	0.0026822	Very low
0.38166 - 0.83041i	57.177	0.078718	
0.41078 - 0.91148i	57.369	0.00020707	Very low
0.17964 - 0.97543i	69.435	0.0059017	Very low
0.064619 - 0.78127i	75.403	0.16142	
0.0069393 - 0.99926i	78.193	0.00045728	Very low
0.0037247 - 0.44012i	88.238	0.46503	Very high

damping ratios, and a norm of mode shapes differences obtained for successively higher order models. The poles and zeros that do not give values that do not satisfy the a pre-selected criteria of acceptable difference in these quantities are not considered the true values. Here we plot a similar diagram, but only for the limits set on the frequencies and damping ratio values for increasing number of model order. Figure 4.5 shows a plot where we plot the frequency values calculated from the poles of increasing order models. For this figure, the ARMA models of order 13, 16, 18 ... 50 were fitted and the frequencies from the fitted models were calculated. The frequency values are shown by the scale on the horizontal axis and the model order is shown on the vertical axis. We clearly note a clumping of certain poles indicating that they are converging to those values. However, some of those clumping poles are also not the correct poles, and they can be identified by the range of their damping ratio values. The figure shows the damping ratio range for these clumping poles. The first four exact frequency values are also shown by dotted vertical lines. Convergence to the first and second natural frequency can be observed for model order 18 and higher. For the third frequency,

the values are slightly off the exact ones but they finally do converge to the exact values for the higher order models. Convergence to the fourth modal frequency though could not be achieved even with the highest model use. Perhaps thus frequency does not contribute to this floor response enough to be captured by the analysis. For model order 30 and above natural frequencies lower than the actual converged values can be seen, but these can again be disregarded based on the fact that their damping values are unrealistically high, and also by the large range of their damping values indicating that the damping ratios for increasing order models fluctuate too much to converge to a specific value; these fluctuations do not occur in the case of the true frequencies associated with the structural modes. This simple graphical representation can, therefore, be used to identify a first few structural frequencies, and therefore the poles corresponding to structural modes, in the presence of noise in the data. The identification of higher mode frequencies is however difficult by this method (or any other method), but it will be shown later that the knowledge of a first few modes is quite often adequate for the detection of structural damage.

4.6 Conclusions

This chapter describes the parametric identification approaches that are used for calculating the modal parameters of a structural system from recorded data. The focus was primarily on the use of the ARMA and ARX models. The ARMA model is used when the only frequency and damping ratios are required. The ARX model is needed when the mode shape values are also needed, and when the data on input is also available. The methods provide accurate values of the modal parameters if no noise is present. As was the case with the wavelet approach, the high damping and higher modes are not a problem with the ARX and ARMA models if the data is not polluted by the noise. However when noise is added to the data the use of the minimum permissible order model is not adequate, and it becomes necessary to use the higher order models. The use of a higher order model introduces spurious poles in the analysis, and the identification of the true poles from a large set of spurious poles can become a problem. This problem, however, can be resolved to a large extent, at least to identify a first few important modal parameters, by the use of a stabilization diagram where the convergence to the true poles can be visually identified.

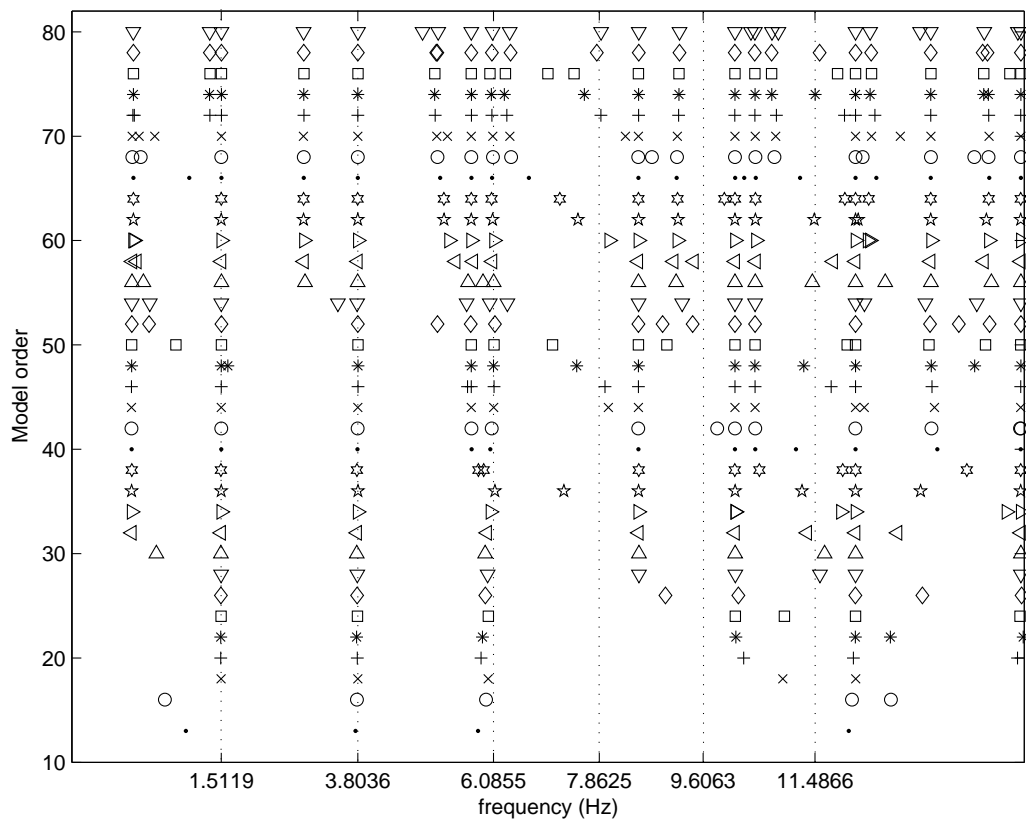


Figure 4.5: The identified natural frequencies as a function of model order for the case of 6-DOF, 5% nominal damping, with 20dB noise.

Chapter 5

Peak Picking Method

5.1 Introduction

In previous chapters the wavelet transform, Hilbert-Huang transform and parametric system identification methods for the estimation of natural frequency, damping and mode shapes from recorded structural response were presented. In this chapter one of the oldest methods that has been used to calculate the natural frequencies and modeshapes is described. This method is often called the peak picking method (PPM), and is based on the simple fact that absolute value of the Fourier transform of a structural response will usually have peaks at the modal frequencies and perhaps also at the input frequencies. This plot of the absolute value of the discrete Fourier transform (DFT) as a function of frequency is called a periodogram. To eliminate the presence of input frequencies, one can use the input free response quantities such as the impulse response function if it can be calculated. For the cases where the input information can not be measured and thus impulse response function can not be calculated, the response covariance function for the broad-band random excitation can also be used. In the following we give a simple analytical explanation for this methods, and use it to calculate the frequencies and mode shapes for the example problem considered earlier.

5.2 Fourier Transform and The Peak Picking Method

Consider a classically damped MDOF linear system with the following equation of motion:

$$\mathbf{M}\ddot{\mathbf{x}}(t) + \mathbf{D}\dot{\mathbf{x}}(t) + \mathbf{K}\mathbf{x}(t) = \mathbf{f}(t) \quad (5.1)$$

Using the modal analysis, the displacement response at p^{th} degree of freedom of this system can be expressed as:

$$x_p = \sum_{j=1}^n \phi_{pj} z_j \quad (5.2)$$

where n is the number of degrees of freedom, ϕ_{pj} is the mode shape value at the p^{th} DOF for the j^{th} mode, and z_j is the generalized coordinate, defined by the following equation

$$\ddot{z}_j + 2\omega_j \zeta_j \dot{z}_j + \omega_j^2 z_j = F_j(t) \quad (5.3)$$

where $F_j(t) = \phi_j^T \mathbf{f}(t)/m_j$ is the generalized force in the j^{th} mode, ϕ_j^T is the transpose of the j^{th} modeshape, $m_j = \phi_j^T \mathbf{M} \phi_j$, ω_j is the j^{th} natural frequency, and ζ_j is the j^{th} modal damping ratio. The Fourier transform of the response in Eq. 5.2 can be written as:

$$X_p(\omega) = \sum_{j=1}^n \phi_j Z_j(\omega) = \sum_{j=1}^n \phi_{pj} H_j(\omega) F_j(\omega) \quad (5.4)$$

where $F_j(\omega)$ is the Fourier transform of the generalized force in the j^{th} mode, and $H_j(\omega)$ is the frequency response function associated with Eq. 5.3 and is defined as:

$$H_j(\omega) = \frac{1}{\omega_j^2 - \omega^2 + 2i\zeta_j \omega \omega_j} \quad (5.5)$$

From Eq. 5.4 one can define the Fourier transform of the absolute acceleration response as:

$$\ddot{X}_p(\omega) = \sum_{j=1}^n \omega^2 \phi_{pj} H_j(\omega) F_j(\omega) = \sum_{j=1}^n \phi_{pj} \frac{\omega^2}{\omega_j^2 - \omega^2 + 2i\zeta_j \omega \omega_j} F_j(\omega) \quad (5.6)$$

The absolute value of this transform will show peaks at the structural frequencies and can also have peaks at the dominant frequencies of the input.

But in most cases the input frequencies are likely to be filtered out. To show this, we specialize this equation for the earthquake induced excitations applied at the base of the structure - the motion of main interest in this study. In such cases the right hand side of Eq. 5.1 will be defined by $f(t) = -\mathbf{M}^T \mathbf{r} \ddot{x}_g(t)$, where \mathbf{r} is the base motion influence coefficient vector, and $\ddot{x}_g(t)$ is the base acceleration due to earthquake induced ground motion. The displacement response vector in the equation of motion, Eq. 5.1, then defines the relative displacement of the system with respect to the base motion. In this case, to obtain absolute acceleration one needs to add the base acceleration to Eq. 5.6. Considering these changes, one can write the Fourier transform $\ddot{X}_{ap}(\omega)$ of the absolute acceleration response $\ddot{x}_{ap}(t)$ at p^{th} degree of freedom as follows:

$$\ddot{X}_{ap}(\omega) = - \sum_{j=1}^n \phi_{pj} \gamma_j \frac{\omega_j^2 + 2i\zeta_j \omega_j \omega}{\omega_j^2 - \omega^2 + 2i\zeta_j \omega_j \omega} \ddot{X}_g(\omega) \quad (5.7)$$

where $\ddot{X}_g(\omega)$ is the Fourier transform of the base acceleration, and $\gamma_j = \phi_j^T \mathbf{M} \mathbf{r} / m_j$ is the modal participation factor. Eq. 5.7 can also be used to calculate the frequency response function $H_{ap}(\omega)$ of the absolute acceleration by simply substituting $X_g(\omega) = 1$. This frequency response function can be written as:

$$H_{ap}(\omega) = - \sum_{j=1}^n \phi_{pj} \gamma_j \frac{\omega_j^2 + 2i\zeta_j \omega_j \omega}{\omega_j^2 - \omega^2 + 2i\zeta_j \omega_j \omega} \quad (5.8)$$

The inverse Fourier transform of this frequency response function provides the impulse response function. In Figure 5.1 the absolute acceleration at the first DOF for the 6-DOF structure is plotted along with its periodogram, when the structure is excited at the base by earthquake excitation. In the plot of the periodogram only three dominant frequencies can be clearly identified. Figure 5.2 shows the impulse response at the same (first) DOF and its corresponding periodogram. This impulse response function was obtained using the Fourier Transforms of the floor response and input motion time histories and not Eq. 5.8. In this case, however, since the response quantity is free of any input, the periodogram clearly identifies all the six structural frequencies present in the response.

To show how these peaks can be used to calculate the relative values of the mode shape, we re-write the expression of frequency response function at a modal frequency say ω_j where one observes a peak in the periodogram

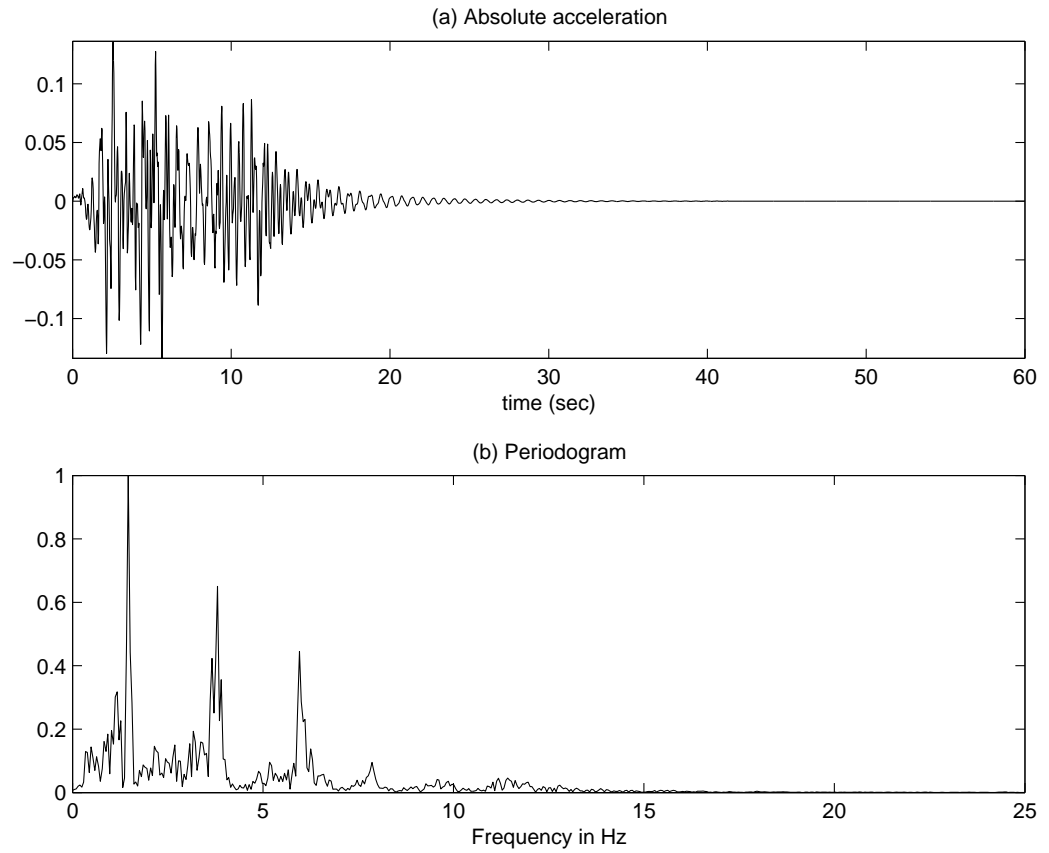


Figure 5.1: First floor absolute acceleration response and its periodogram for the 6-DOF, 2% nominal damping structure.

as follows:

$$\ddot{X}_{ap}(\omega_j) = -\frac{1 + 2i\zeta_j}{2i\zeta_j} \gamma_j \phi_{pj} - \sum_{k \neq j} \phi_{pk} \gamma_k \frac{\omega_k^2 + 2i\zeta_k \omega_j \omega_k}{\omega_k^2 - \omega_j^2 + 2i\zeta_k \omega_j \omega_k} \quad (5.9)$$

For the usual values of the modal damping ratios, the first term will dominate the remaining terms in the summation. The imaginary part of the transform at this peak is proportional to the mode shape value at the p^{th} degree of freedom. Thus, the ratio of the imaginary parts of the peak values at a modal frequency ω_j of the frequency response functions (and also the Fourier transform of the response) at two degrees of freedom defines the relative

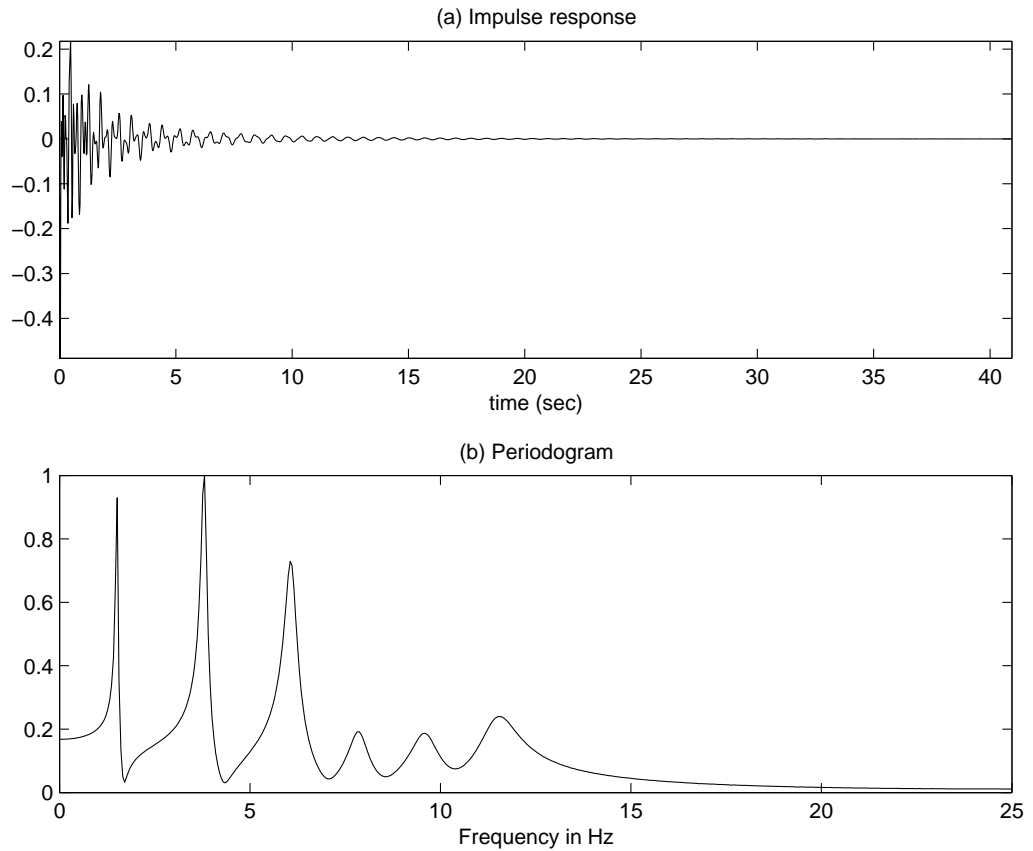


Figure 5.2: First floor impulse response and its periodogram for the 6-DOF, 2% nominal damping structure.

values of the mode shape at these degrees of freedom as follows:

$$\frac{|\phi_{jp}|}{|\phi_{jq}|} \approx \frac{\text{Imag}(\ddot{X}_{ap}(\omega_j))}{\text{Imag}(\ddot{X}_{aq}(\omega_j))} \quad (5.10)$$

The sign of the mode shape values are assigned based on the phase of the complex quantities $H_{ap}(\omega_j)$ and $H_{aq}(\omega_j)$. This simple technique utilizing the periodograms to estimate modal parameters has been commonly used to estimate the modal frequencies and mode shape values. The use of this approach to estimate the modal damping ratios has also been attempted with the help of the half power width approach. However, such calculations tend to provide large errors in the damping ratio values. In this chapter,

Table 5.1: Actual mode shapes for the 6-DOF structure

Mode 1	Mode 2	Mode 3	Mode 4	Mode 5	Mode 6
1.0000	1.0000	1.0000	1.0000	1.0000	1.0000
1.9481	1.6713	1.1585	0.5954	-0.0967	-0.9979
3.2707	1.8617	-0.1164	-1.3427	-1.4928	0.5540
4.3546	1.1918	-1.2537	-0.6298	1.5108	-0.2286
5.5793	-0.7595	-0.7013	2.4980	-0.8058	0.0604
6.2252	-2.2121	1.0299	-1.3832	0.2527	-0.0121

only the frequencies and mode shape values have been obtained from the recorded data. This approach also get into problem when there are closely spaced system modes. In such cases it becomes difficult to identify the peaks corresponding to the two or more close modes. In such cases the use of the singular value decomposition of the frequency response function values has been suggested (Peeters, 2000). This, however, is not further explore in this study.

5.3 Numerical Results

This simple method of PP was applied to the 6-DOF structure in order to evaluate its effectiveness. Figures 5.1 and 5.2 showed how the periodogram of the impulse response at the first DOF correctly identifies all the six structural frequencies. Using the base excitation and the absolute acceleration, impulse responses at all the DOF were calculated. The method outlined in the previous section was used to estimate the mode shapes. Figure 5.3 shows the actual and the identified mode shapes, and Table 5.1 and Table 5.2 list their respective values. Excellent agreement can be seen between the two sets of values.

Similar simulations were run for the 6-DOF structure but with 10% damping. Figure 5.4 shows the impulse response at the first DOF and its corresponding periodogram. The impulse response can be seen to be dying off quickly and the periodogram indicates just three dominant frequencies. However since the actual frequencies are known here, mode shapes were identified for all the six modes. For the first three modes, the imaginary part of the

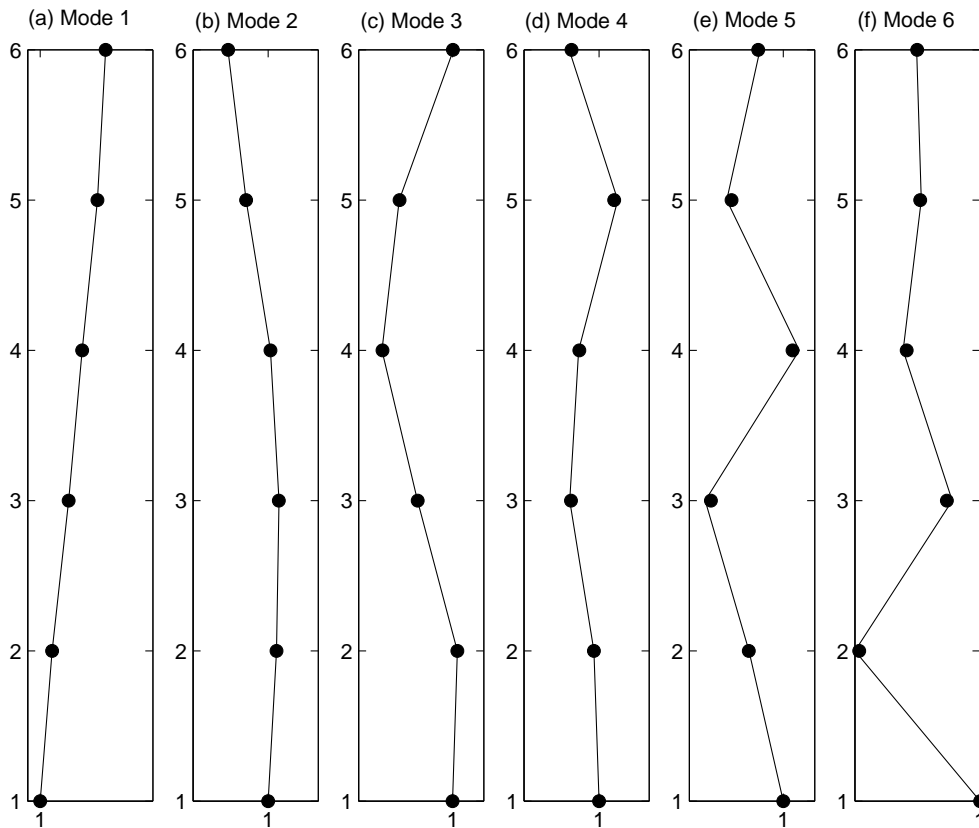


Figure 5.3: Actual and identified mode shapes for the 6-DOF 2% nominal damping structure, no-noise.

Fourier transform was evaluated at the three dominant frequencies indicated by the periodogram. For modes four to six, exact frequencies were used. In Figure 5.5 the actual and identified mode shapes using the PP method are plotted, and Table 5.3 lists the identified mode shape values. Good agreement between the actual and identified mode shapes can be seen for the first three modes, the other modes as indicated by the periodogram are not significant and cannot be even identified based on the periodogram plot.

To see the effect of noise on this method, the 6-DOF structure was excited at the base and the simulated acceleration responses were corrupted with 20dB of noise. These noise corrupted acceleration records were used to form the impulse response functions. Figure 5.6 shows the noisy impulse response

Table 5.2: Identified mode shapes for the 6-DOF structure, with 2% nominal damping, no-noise

Mode 1	Mode 2	Mode 3	Mode 4	Mode 5	Mode 6
1.0000	1.0000	1.0000	1.0000	1.0000	1.0000
1.9480	1.6702	1.1561	0.5952	-0.1042	-0.9310
3.2704	1.8592	-0.1120	-1.2376	-1.3128	0.4709
4.3540	1.1907	-1.2363	-0.5819	1.2940	-0.1718
5.5782	-0.7538	-0.6879	2.2131	-0.6511	0.0436
6.2237	-2.2004	1.0121	-1.2030	0.2013	-0.0042

Table 5.3: Identified mode shapes for the 6-DOF structure, with 10% nominal damping, no-noise

Mode 1	Mode 2	Mode 3	Mode 4	Mode 5	Mode 6
1.0000	1.0000	1.0000	1.0000	1.0000	1.0000
1.9456	1.6479	1.1219	0.6620	0.0880	-0.3130
3.2608	1.8082	-0.0064	-0.4951	-0.5111	-0.0839
4.3359	1.1699	-0.9171	-0.3655	0.2622	0.1381
5.5477	-0.6245	-0.4764	0.5300	0.0726	0.0015
6.1859	-1.9414	0.7144	-0.1095	-0.0023	0.0357

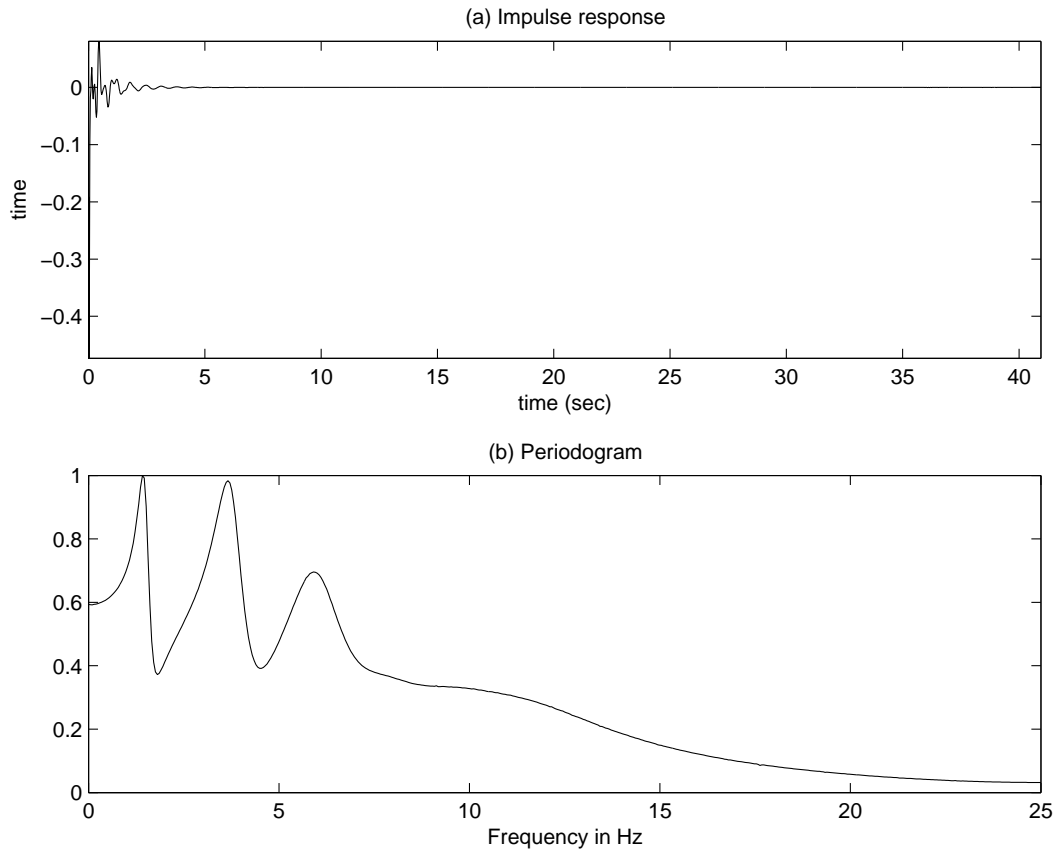


Figure 5.4: First floor impulse response and its periodogram for the 6-DOF, 10% nominal damping structure, no-noise.

for the first DOF and its periodogram. Several peaks can be seen in the periodogram plot. Higher frequencies can be attributed to noise, thus just the first four peaks were chosen as representing the structural frequencies, and mode shapes for the first four modes were formed. Figure 5.7 shows the four modes estimated using the noisy impulse response. The estimated mode shapes are close to the actual ones only for modes 1 to 3. Table 5.4 lists the identified mode shape values.

Another feature of the use of the PPM for modal analysis is averaging of the periodogram. The effect of noise can be reduced by averaging several periodograms of the response quantity. This will however need large time

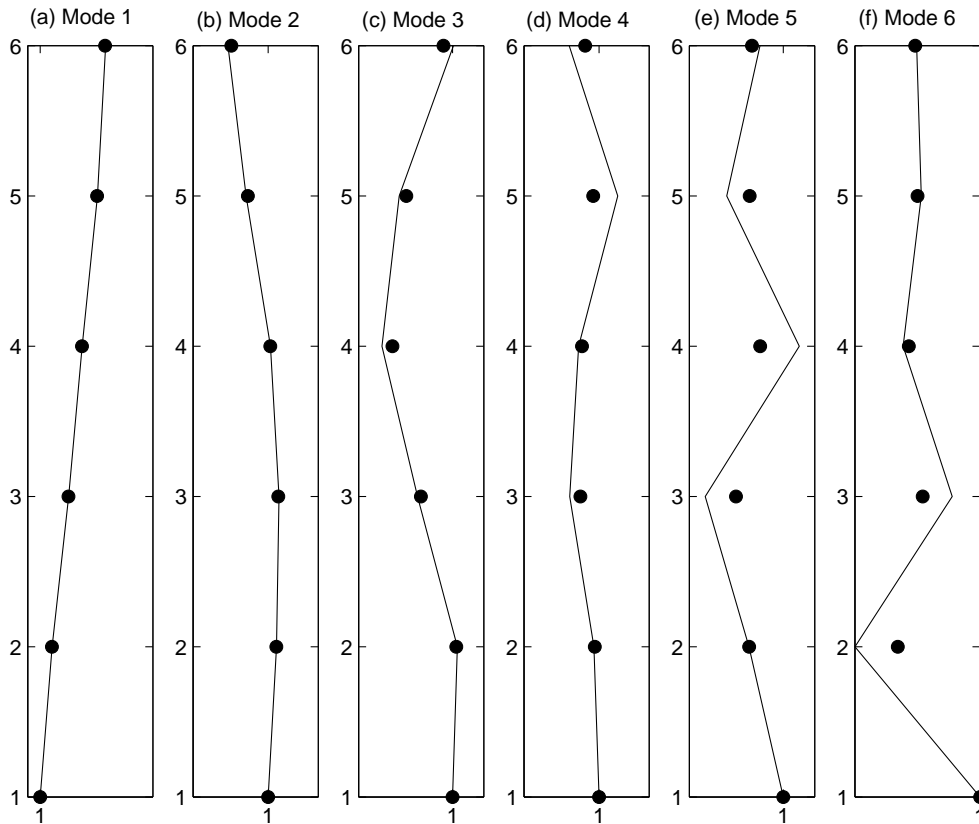


Figure 5.5: Actual and identified mode shapes for the 6-DOF 10% nominal damping structure, no-noise.

domain data. Which would then be divided into blocks, whose periodograms would be calculated and finally all the periodograms would be averaged. To illustrate the use of averaging, the ASCE SHM benchmark structure is considered. This structure was exposed to random excitation at all the floors in one of the horizontal direction. The acceleration response in that direction was simulated for 40 seconds at a sampling frequency of 1000Hz, and 10% RMS noise was added to it. Figure 5.8 shows the plot of the acceleration response at floor 1 and its periodogram, when just 1024 data points were used. The periodogram shows three peaks which can be taken to correspond to structural frequencies. The original acceleration record was next divided into blocks of length 1024x8. The DFT of each block was evaluated and then the averaged periodogram was formed. Figure 5.9 shows the 40sec of sim-

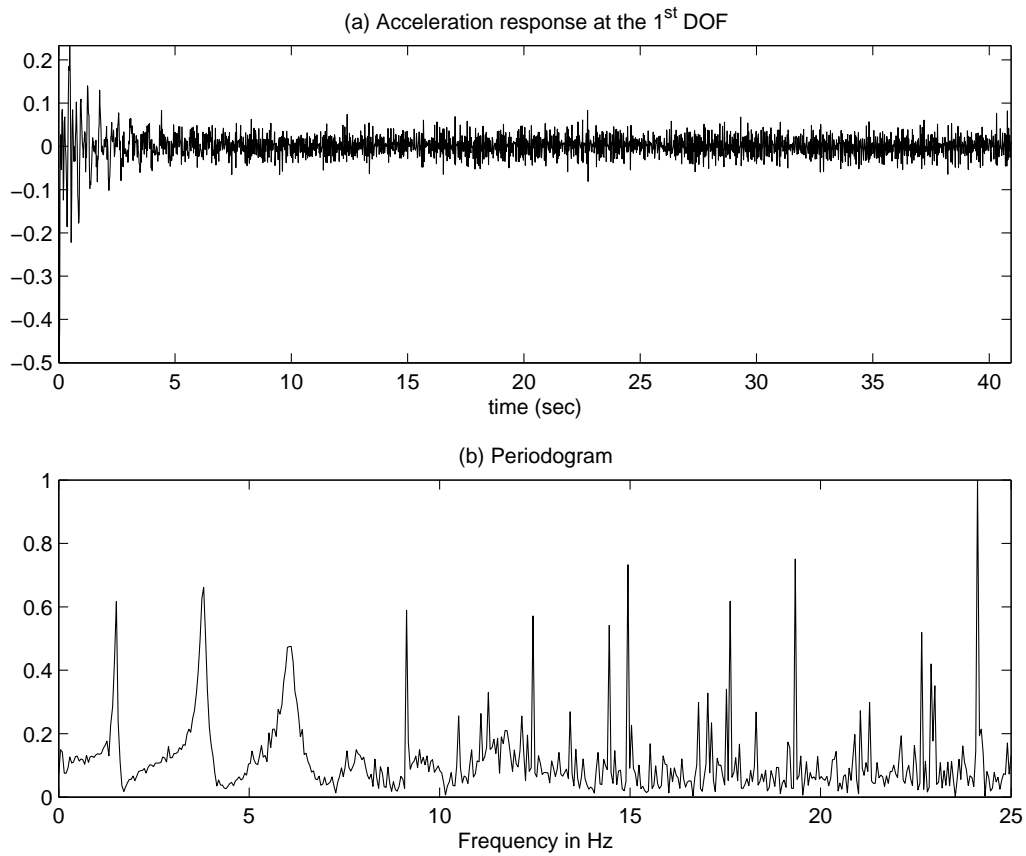


Figure 5.6: (a) First floor noisy impulse response for the 6-DOF structure, 2% nominal damping, 20dB noise and its (b) periodogram

ulated acceleration record and its averaged periodogram. In the plot of the periodogram the four structural frequencies can clearly be identified, unlike in Figure 5.8. This periodogram was used to identify the four modal frequencies, and they were used to calculate the mode shape values. The actual and the identified mode shapes are listed in Table 5.5 and Table 5.6 respectively. In Figure 5.10 the actual and identified translational mode shapes are plotted, where the averaged periodograms were used for all the floors. The estimated values match well with the actual ones. It must be noted that such averaging will require large amount of time data. Though there is no evident reduction in the magnitude of the periodogram corresponding to the noise, the averaging in this case, however, helps in identifying all the structural

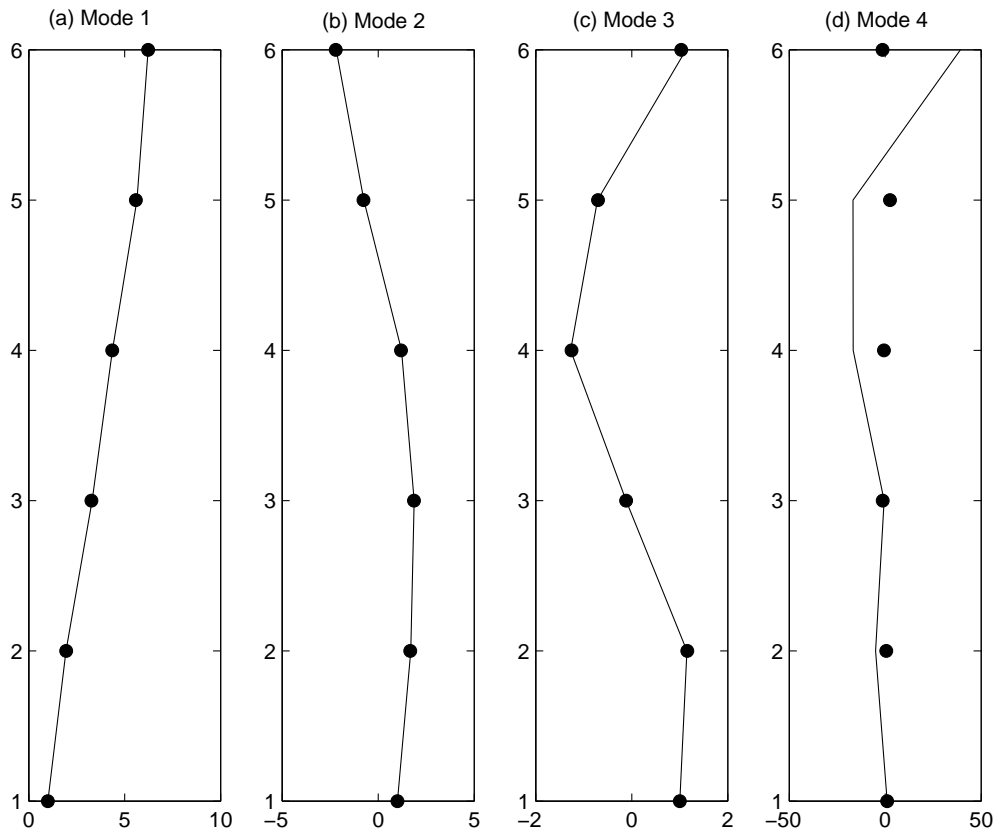


Figure 5.7: First four actual and identified mode shapes for the 6-DOF structure, 2% nominal damping, 20dB noise

frequencies.

5.4 Conclusions

The PP method is a simple method based on the Fourier transform of measured data. The plot of the absolute value of the Fourier coefficients can be used for estimating the natural frequency of a multi degree of freedom system. The theoretical basis of the use of these Fourier coefficients for the estimation of mode shapes is presented, and through numerical examples it is shown that this simple method provides the best results for all the cases that are considered in this study. Unlike the methods described in previous

Table 5.4: Identified mode shapes for the 6-DOF structure, with 2% nominal damping, 20dB noise

Mode 1	Mode 2	Mode 3	Mode 4
1.0000	1.0000	1.0000	1.0000
1.9229	1.6416	1.1687	0.4877
3.2485	1.8443	-0.1454	-1.4414
4.2706	1.1619	-1.1531	-0.7188
5.5711	-0.7757	-0.6252	2.3245
6.1456	-2.1990	0.9719	-1.2156

Table 5.5: Actual translational mode shapes for the ASCE SHM benchmark structure

Mode 1	Mode 2	Mode 3	Mode 4
1.0000	1.0000	1.0000	1.0000
1.8222	0.6902	-1.0005	-2.6260
2.3956	-0.3141	-0.6947	3.0809
2.6418	-1.0024	1.2125	-2.1619

Table 5.6: Identified mode shape for the ASCE SHM benchmark structure

Mode 1	Mode 2	Mode 3	Mode 4
1.0000	1.0000	1.0000	1.0000
1.8673	0.7296	-1.0508	-2.8016
2.5317	-0.2966	-0.7820	2.8577
2.7545	-1.0517	1.4156	-2.2214

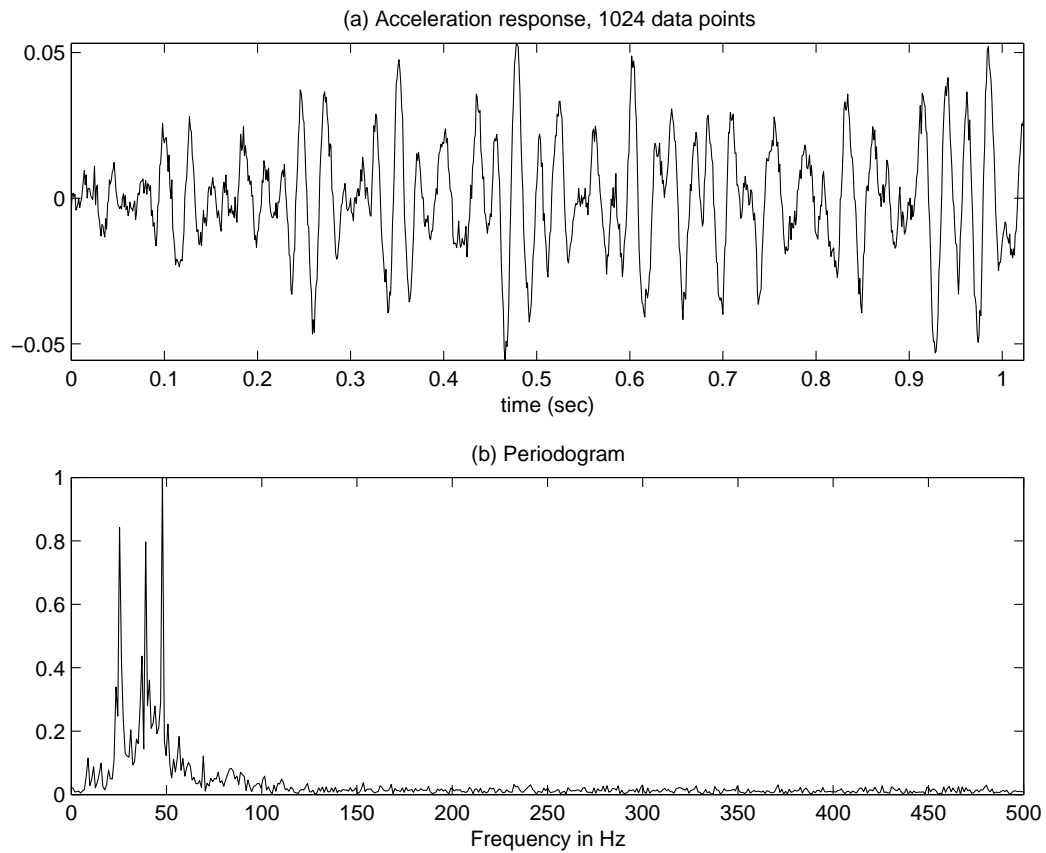


Figure 5.8: (a) 1024 data points of the first floor acceleration response for the ASCE SHM benchmark structure and its (b) periodogram

chapters the PP method is found to be least affected by measurement noise. Good estimates of the first few mode shapes were obtained even with noise corrupted data. This becomes important as various methods for damage localization rely on estimates of flexibility, rotational flexibility etc. for which accurate information of the first few modes is enough.

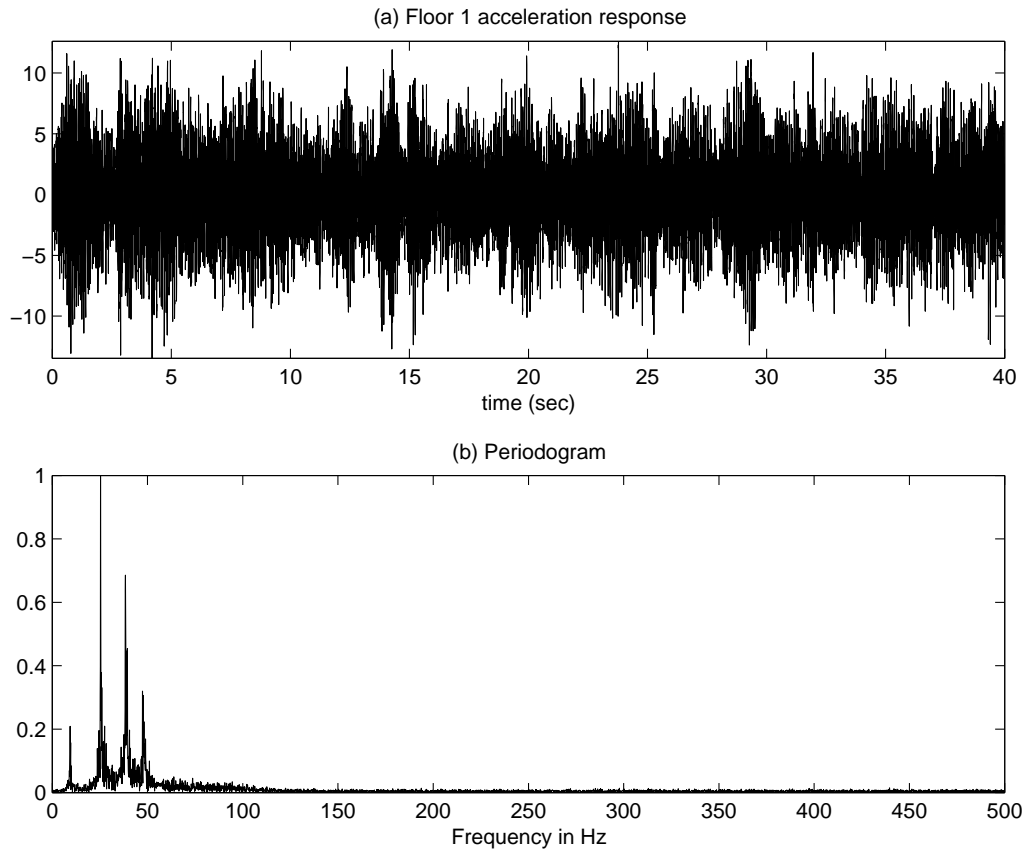


Figure 5.9: (a) First floor acceleration response for the ASCE SHM benchmark structure and its (b) averaged periodogram

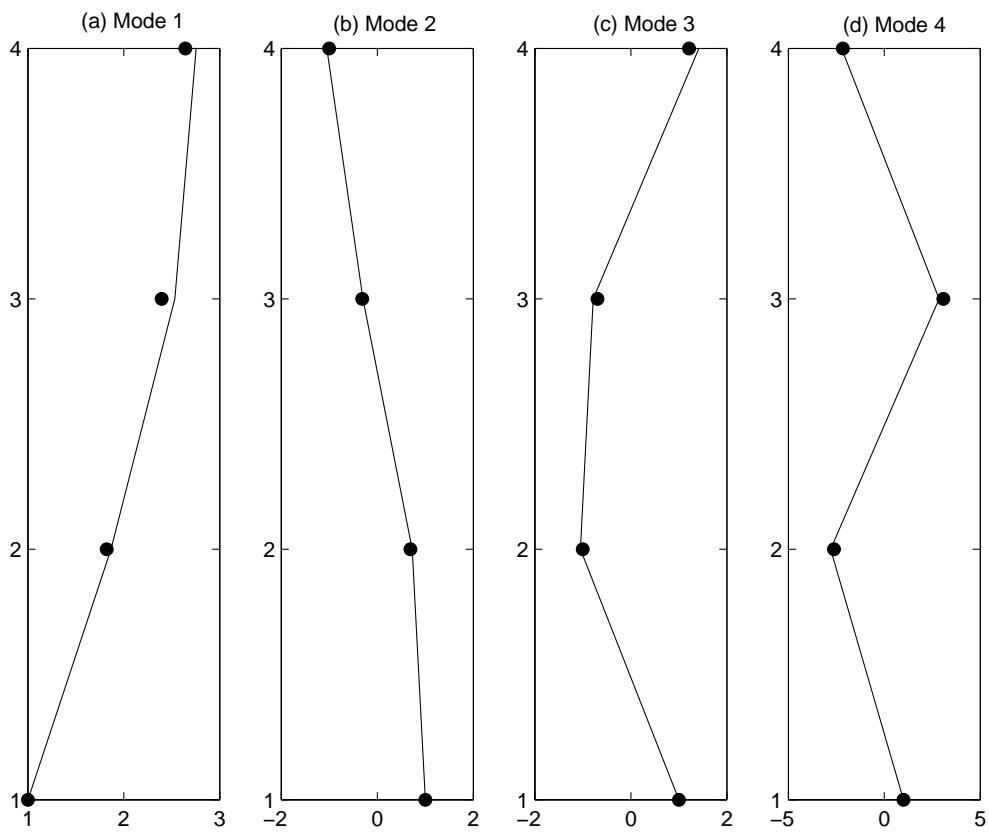


Figure 5.10: Actual and identified mode shapes for the benchmark structure with 10% noise

Chapter 6

Damage Detection

6.1 Introduction

One of the goals of Structural Health Monitoring (SHM) is detecting damages. Invariably all the techniques of damage detection follow a similar path. This being, estimating some parameter related to the structural condition from measured responses, and deciding on the state of the structure based on methods that use these parameters. The most common parameters of interest that are used to detect damages are modal parameters like the natural frequency and mode shapes. In previous chapters various methods for modal parameter estimation have been studied, namely the method of wavelet analysis, parametric system identification, Hilbert-Huang transform, and the peak-picking method. In this chapter using the estimated modal parameters the location of damage in multi-degree of freedom (MDOF) systems is studied.

To identify the location of damage in a structure various methods have been suggested in literature. Several methods rely on the most easily available parameter for a MDOF system i.e. its natural frequency, which can be estimated from available free or forced vibration response. An inspection of the change in various modal frequencies can help in figuring out if there has been any change in the structural properties or not. Various approaches have been suggested to help find the damage location based on natural frequencies. The newest among these being the technique of pattern recognition and support vector machines (Mita and Hagiwara, 2002); (Mita, 2004), and

techniques based on the multiple natural frequency shifts (Hamamoto, *et. al.*, 2002); (Morita *at. al.*, 2001). Besides this other common methods are those based on the change in mode shapes, change in mode shape curvature, change in flexibility, those using the stiffness matrix etc.

Both the stiffness and the flexibility matrix depend on the square of modal frequencies. However the stiffness matrix is directly proportional and the flexibility matrix is inversely proportional to the square of modal frequencies. Therefore the flexibility matrix can be estimated with a better accuracy using just a few lower modes than the stiffness matrix. Since estimating the modal parameters related to lower modes is easier than those of higher modes, the methods for damage detection based on flexibility matrix seem to be better options than those using the stiffness matrix. This feature of the flexibility matrix for damage detection has been explored for its use using only the first few modal frequencies and mode shapes (Pandey and Biswas, 1994); (Pandey and Biswas, 1995).

Recently a new concept of rotational flexibility (Duan, *et. al* 2004) has been introduced which seems to have certain advantages over the flexibility based damage detection methods. In this chapter the methods based on the change in flexibility and change in rotational flexibility are studied for damage detection for the case of MDOF structures. Through simulations it is shown that both these methods can be used for identifying multiple damages. However, it is found that the method on rotational flexibility is less affected by the mode shape normalization and it performs better than the flexibility matrix.

6.2 Flexibility approach

In this section the method for damage detection using the flexibility matrix approach is reviewed. For a multi-degree of freedom structure if the mode shape matrix Φ is normalized such that $\Phi^T \mathbf{M} \Phi = \mathbf{I}$ the stiffness matrix \mathbf{K} and the flexibility matrix \mathbf{F} can be expressed as (Pandey and Biswas, 1994)

$$\mathbf{K} = \mathbf{M} \Phi \Omega^2 \Phi^T \mathbf{M} \quad (6.1)$$

$$\mathbf{F} = \Phi \Omega^{-2} \Phi^T \quad (6.2)$$

where $\mathbf{\Omega}$ is a diagonal matrix with its elements being ω_i^2 . From these equations it can be seen that the stiffness matrix depends directly on the square of natural frequencies and therefore higher frequencies will contribute significantly to its value. On the other hand the flexibility matrix depends inversely on the natural frequencies and higher frequencies contribute less as compared to lower frequencies. Therefore in real life applications where lower modal frequencies are available with more accuracy, the use of flexibility matrix becomes a better choice over the use of stiffness matrix for damage detection and localization. The convergence of the flexibility matrix as more modes are used in estimating it is shown in Figure 6.1 for the ASCE SHM benchmark structure. The convergence is evaluated in terms of the Frobenius norm. The Frobenius norm of a matrix A is defined as

$$\sqrt{\text{trace}(A^*A)} \quad (6.3)$$

where A^* is the Hermitian conjugate matrix of A . The normalized Frobenius norm is defined as the ratio of the Frobenius norms of the difference of the actual and estimated matrix to the Frobenius norm of the actual matrix.

$$\frac{\|A - A_e\|}{\|A\|} \quad (6.4)$$

Using different number of modes the flexibility matrix was estimated. The vertical axis of Figure 6.1 is the normalized Frobenius norm which is calculated using Eq. 6.4, where A is the actual flexibility matrix and A_e is the estimated flexibility matrix using just a few modes. In the figure the numbers represent the range of modes used in the estimation. It can be seen that even if the flexibility matrix is estimated using just the first mode the norm is much less than 1. This figure shows that the flexibility matrix can indeed be estimated with a good accuracy with just a few lower modes.

Any damage in the structure leads to a decrease in the stiffness and consequently it would lead to an increase in the flexibility. It has been shown that by evaluating the difference in the flexibility matrix before and after the damage the location of the damage in a structure can be found (Pandey and Biswas, 1994); (Pandey and Biswas, 1995). For this firstly, the flexibility matrix of the healthy structure \mathbf{F}_H is calculated. At a later stage when the integrity of the structure is to be tested, the current flexibility matrix \mathbf{F}_C is evaluated and the difference $\mathbf{F}_D = \mathbf{F}_C - \mathbf{F}_H$ is calculated. The location of

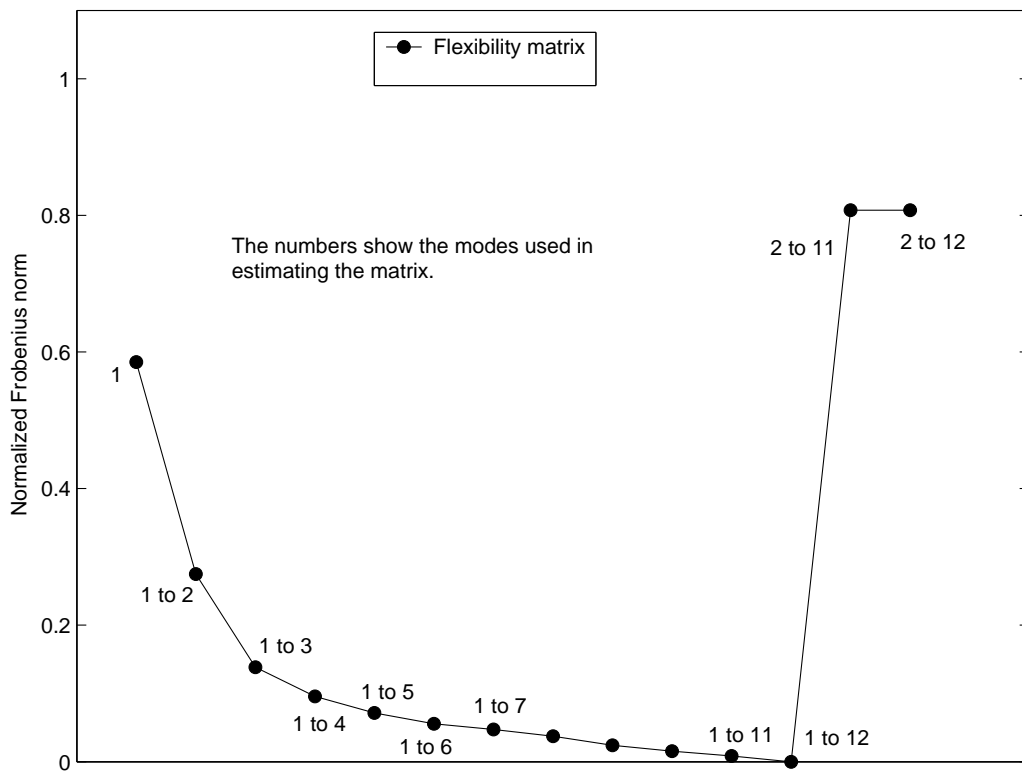


Figure 6.1: Frobenius norm for the flexibility matrix estimated using different number of modes for the 12-DOF ASCE SHM benchmark structure

the damage in the structure can be found based on either an inspection of the matrix \mathbf{F}_D or by an inspection of a damage index which is defined based on the elements of the matrix \mathbf{F}_D .

In this study, for a n -degree of freedom (DOF) system, a damage index for the identification of the location of damage is defined as in (Pandey and Biswas, 1994),

$$d_i = \max[|F_D(:, i)|] \quad (6.5)$$

where,

$$i = 1, 2, \dots, n$$

i.e. corresponding to the i^{th} DOF the damage index is the maximum absolute value in the i^{th} column of F_D . A comparison of the various d_i 's can provide the location of the damage, this is shown later in detail.

6.3 Rotational flexibility approach

Since it is difficult to measure the rotational degrees of freedom, and measurements of translational degrees of freedom are most easily available, the flexibility approach uses the flexibility matrix based on just the translational degrees of freedom. Recently it has been shown that this method may not be able to localize multiple damages in a structures (Duan, *et. al* 2004).

To better localize the identified damage and to identify multiple damage locations a new method based on rotational flexibility has been proposed (Duan, *et. al* 2004). In this method a rotational flexibility matrix, which takes into account the rotational effect between different degrees of freedom is shown to be more effective in locating and localizing multiple damages.

The flexibility matrix for a n -DOF system (a cantilever beam is considered in the original work (Duan, *et. al* 2004)) may be written as,

$$F = \begin{bmatrix} F_{11} & F_{21} & \dots & F_{1(n-1)} & F_{1n} \\ F_{21} & F_{22} & \dots & F_{2(n-1)} & F_{2n} \\ \vdots & \vdots & \vdots & \vdots & \vdots \\ F_{(n-1)1} & F_{(n-1)2} & \dots & F_{(n-1)(n-1)} & F_{(n-1)n} \\ F_{n1} & F_{n2} & \dots & F_{n(n-1)} & F_{nn} \end{bmatrix} \quad (6.6)$$

The individual elements of the flexibility matrix can be written as,

$$F_{ij} = \sum_{r=1}^n \frac{\phi_{ir}\phi_{jr}}{\omega_r^2} \quad (6.7)$$

All the elements of each column of this matrix are the translations or rotations at the DOF, when a unit force or moment is applied at a particular DOF. To form the rotational flexibility matrix the structure is divided into n elements of length h . Parallel to the flexibility matrix, the elements of each column of the rotational flexibility matrix are the translations or rotations caused when a couple is applied to the e^{th} element. Each column of this matrix has the following form (Duan, *et. al* 2004),

$$\begin{bmatrix} \theta_{1e} \\ \theta_{2e} \\ \vdots \\ \theta_{ee} \\ \theta_{(e+1)e} \\ \vdots \\ \theta_{ne} \end{bmatrix} = \frac{1}{h} \begin{bmatrix} F_{1j} - F_{1i} \\ (F_{2j} - F_{2i}) - (F_{1j} - F_{1i}) \\ \vdots \\ (F_{jj} - F_{ji}) - (F_{ij} - F_{ii}) \\ \vdots \\ (F_{nj} - F_{ni}) - (F_{(n-1)j} - F_{(n-1)i}) \end{bmatrix} \quad (6.8)$$

where a couple is applied to the e^{th} element.

Using equation 6.7 the elements of the rotational flexibility matrix can be expressed in terms of the mode shapes. However, it can be seen that the full rotational flexibility matrix can be written as the sum of four matrices each of which is a shifted version of the flexibility matrix. It is this approach which is used in the numerical simulations. From the extracted mode shape the flexibility matrix is formed which is then used to form the rotational flexibility matrix taking into account the length or height factor h .

Similar to the flexibility based method for damage detection, detecting the location of damage using the rotational flexibility involves the knowledge of the rotational flexibility of the healthy structure, F_{rotH} and that of the current structure F_{rotC} . Forming the difference $F_{rotD} = F_{rotH} - F_{rotC}$ a damage index similar to Eq. 6.5 is defined,

$$d_{roti} = \max[|F_{rotD}(:, i)|] \quad (6.9)$$

where,

$$i = 1, 2, \dots, n$$

as in the case of flexibility matrix, corresponding to the i^{th} DOF the damage index is the maximum absolute value in the i^{th} column of F_{rotD} . A comparison of the various d_{roti} 's can provide the location of the damage. Figure 6.2 shows the normalized Frobenius norm for the rotational flexibility matrix estimated using different number of modes for the ASCE SHM benchmark structure, calculated using Eq.6.4 with A being the actual rotational flexibility matrix and A_e the estimated rotational flexibility matrix using different modes. Similar to Figure 6.1 the vertical axis is the normalized Frobenius norm and the numbers represent the range of modes used in estimating the rotational flexibility matrix. It can be seen that just like the flexibility matrix the rotational flexibility matrix can be estimated to with good accuracy using just a few lower modes.

6.4 Numerical results

The methods based on the change in the flexibility matrix and rotational flexibility matrix were applied on MDOF systems for comparison. For detecting the damage, damage indexes as defined in Eqs 6.5 and 6.9 were used for the flexibility and the rotational flexibility methods respectively.

Figure 6.3 shows the plot of the damage index calculated using the flexibility matrix, for the case of the 6-DOF structure when the mode shapes are normalized such that $\Phi^T \mathbf{M} \Phi = 1$. Damage at a story can be pointed out if the value of the damage index at that story shows a sudden increase with respect to the previous value. Figure 6.4 shows the damage indexes for the same cases, but when the flexibility matrix is obtained from arbitrarily normalized mode shapes. Comparing the two figures it can be seen that a uniform method for detecting the damage from these plots cannot be established, and it depends whether the mode shapes are mass normalized or not.

Figures 6.5 shows the corresponding damage index figure using the rotational flexibility matrix approach when the mode shapes are mass-normalized. In this case however damages are indicated not by sudden increase in damage index values but simply by large damage index values. Figure 6.6 shows the results for similar cases but when the mode shapes are not mass-normalized.

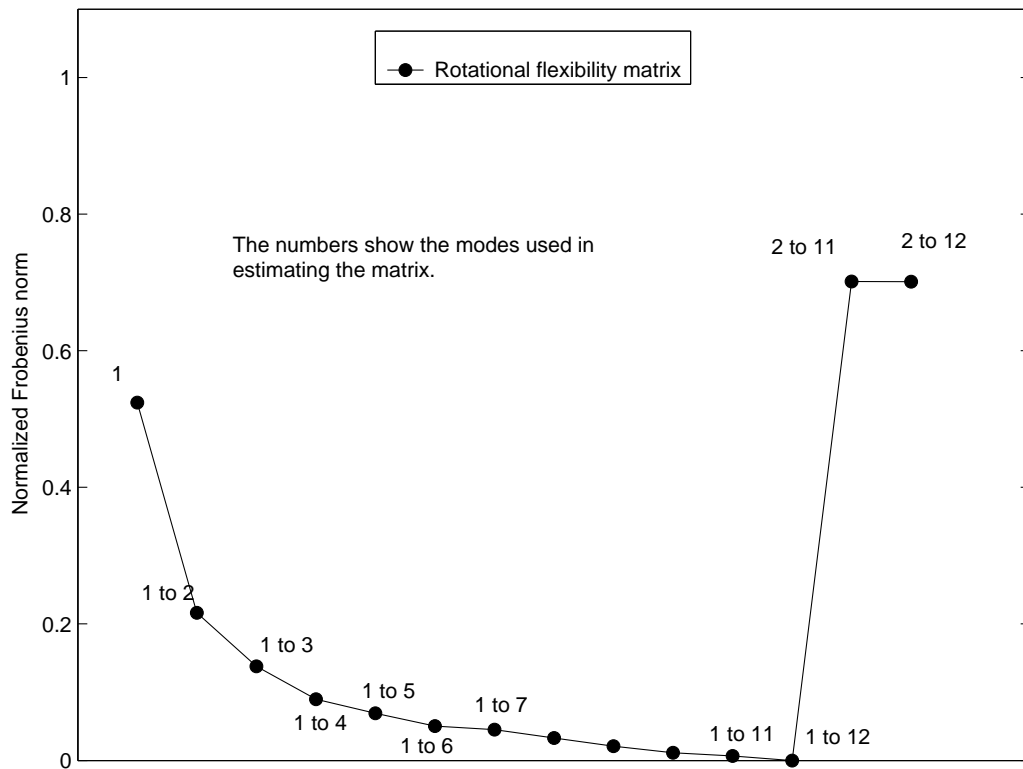


Figure 6.2: Frobenius norm for the rotational flexibility matrix estimated using different number of modes for the 12-DOF ASCE SHM benchmark structure

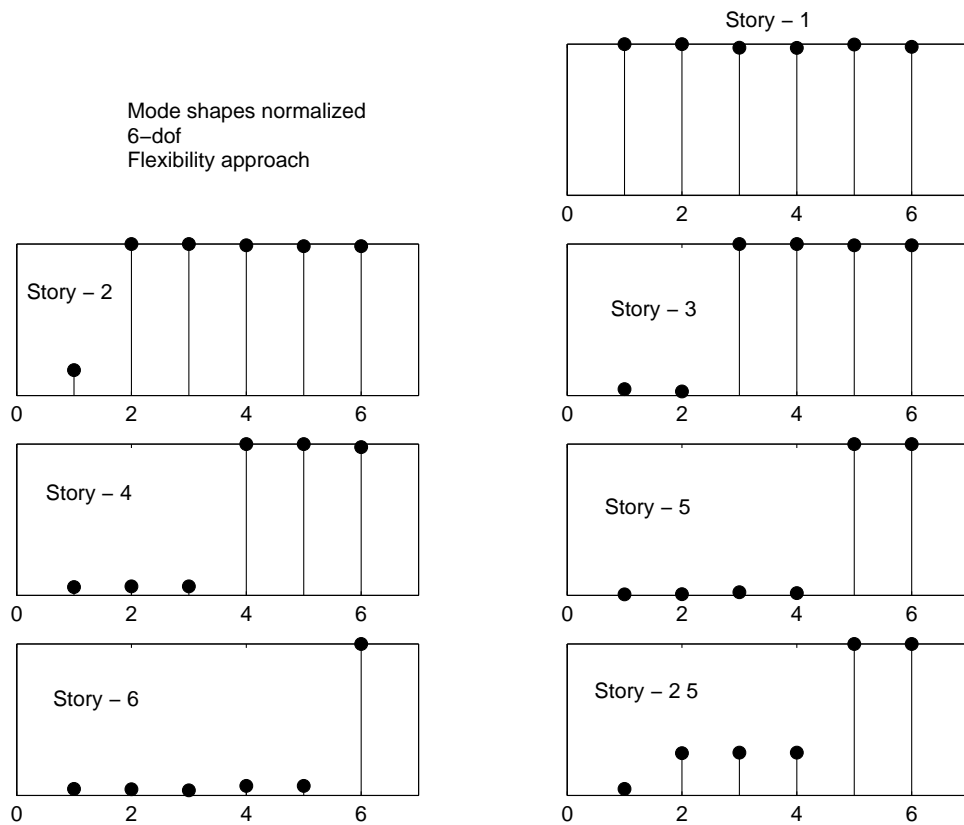


Figure 6.3: Damage detection using the flexibility matrix approach with normalized mode shapes for the 6-DOF structure

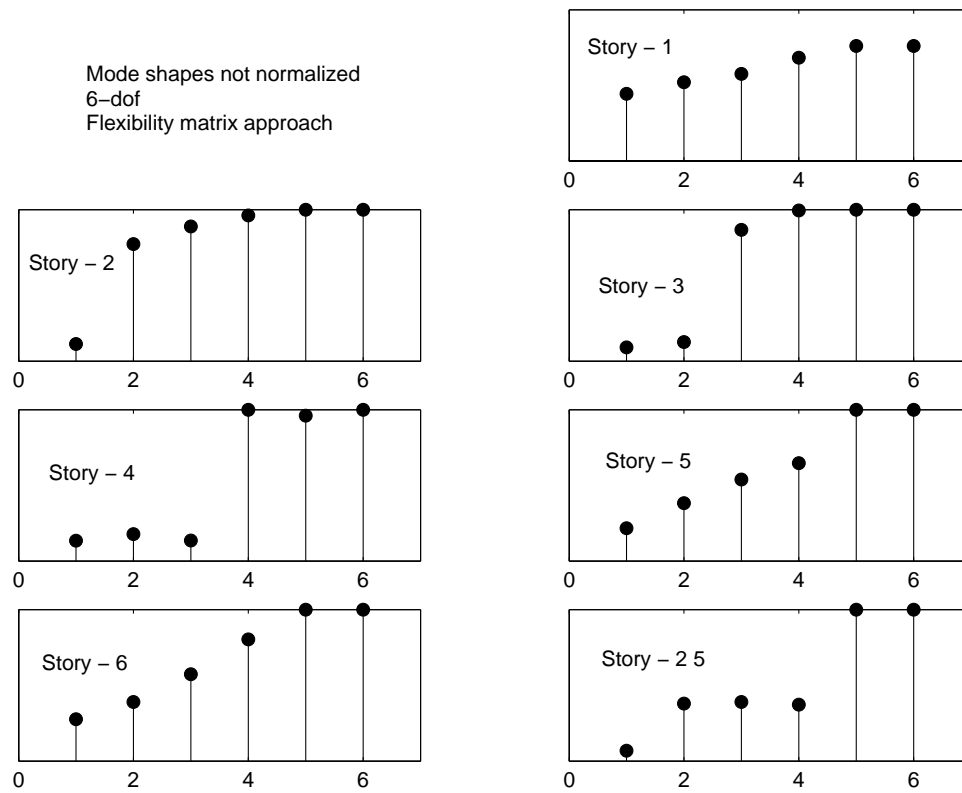


Figure 6.4: Damage detection using the flexibility matrix approach with non-normalized mode shapes for the 6-DOF structure

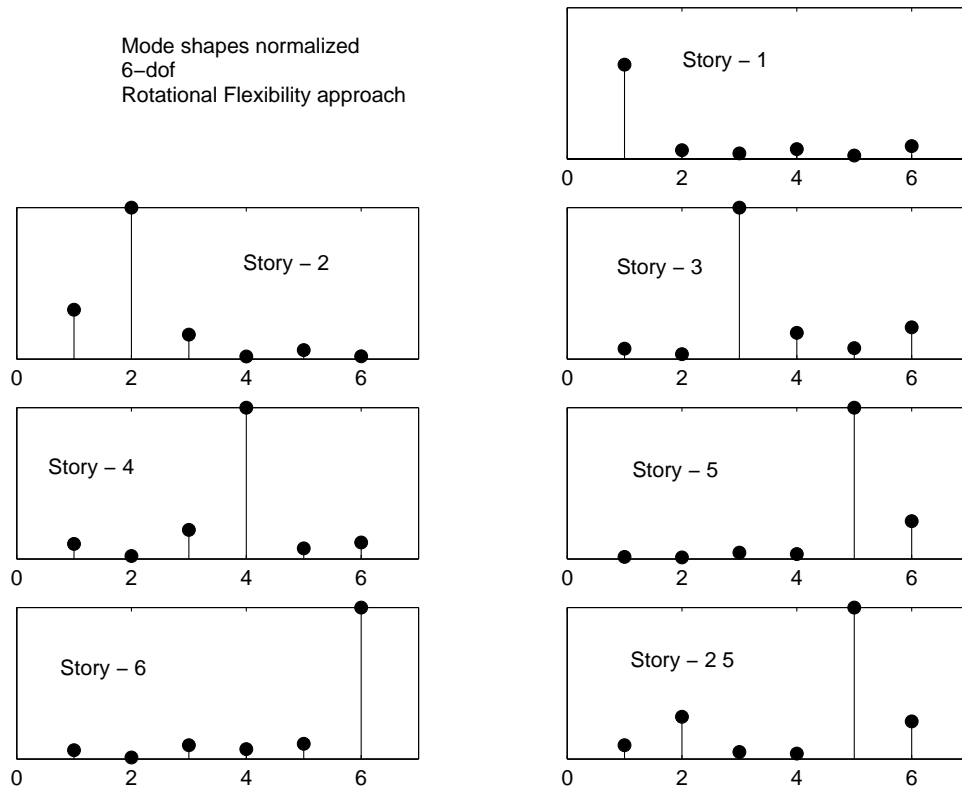


Figure 6.5: Damage detection using the rotational flexibility matrix approach with normalized mode shapes for the 6-DOF structure

It can be seen the normalization of mode shapes has less effect on the relative values of the damage indexes defined on the rotational flexibility matrix.

Finally Figure 6.7 and 6.8 show the damage indexes for damage detection in the ASCE SHM benchmark structure for the case of damage in one story and in multiple stories respectively, (the damage was simulated by removing the braces). Damage in the case of single story is clearly identified by the maximum value of the damage index corresponding to that floor. In the case of multiple damage (Figure 6.8) the two damaged floors can be identified by the two largest values of the damage index. However to bring out the difference between the values of the damage index corresponding to damaged floors and those corresponding to undamaged floors, a different damage index needs to be defined. The mode shapes for all the cases were identified using

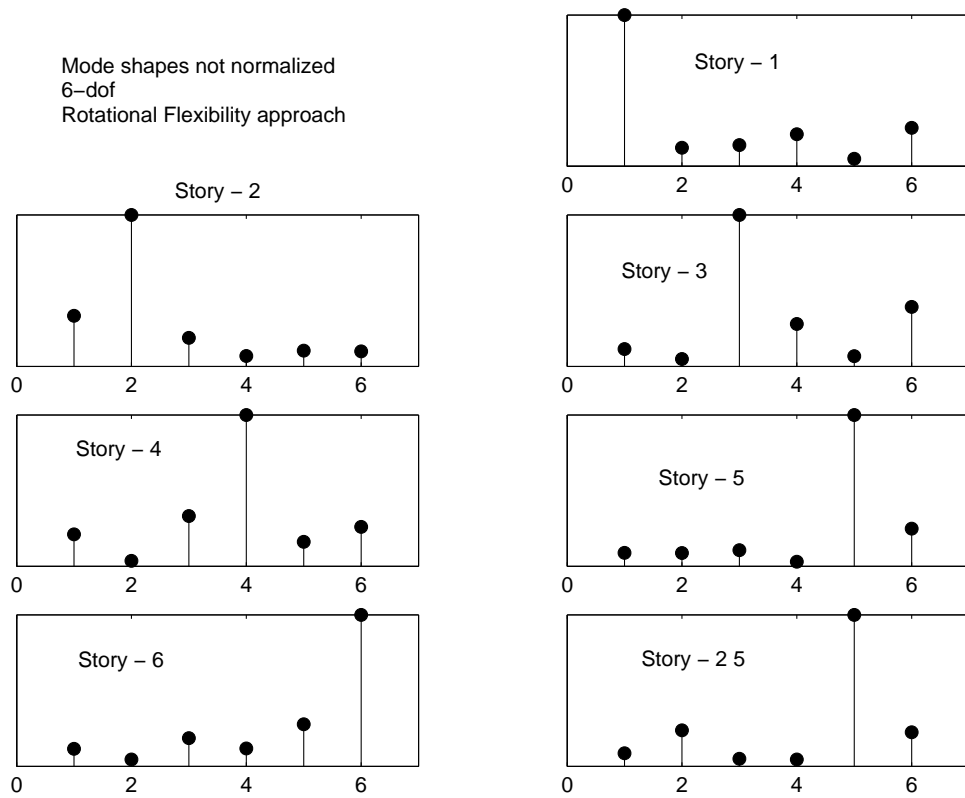


Figure 6.6: Damage detection using the rotational flexibility matrix approach with non-normalized mode shapes for the 6-DOF structure

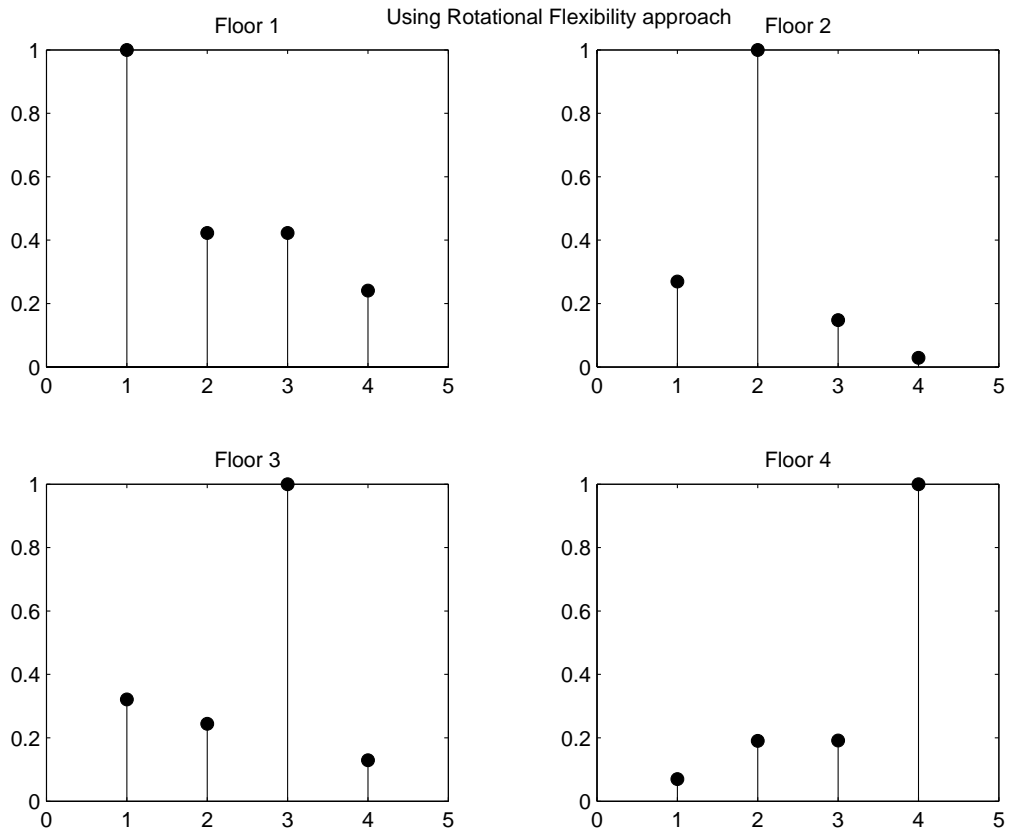


Figure 6.7: Damage detection using the rotational flexibility matrix approach for the ASCE benchmark structure, damage in one story.

the peak-picking method, and the floor accelerations were corrupted with 10% noise.

6.5 Conclusions

In this chapter the methods based on the flexibility matrix and the rotational flexibility matrix are compared for their effectiveness in locating damages in MDOF structures. Damage indices which correspond to the maximum absolute value of each column of the difference of the matrices corresponding to the healthy and damaged structure were used. It was found that both these methods can correctly identify the location of single or multiple damages.

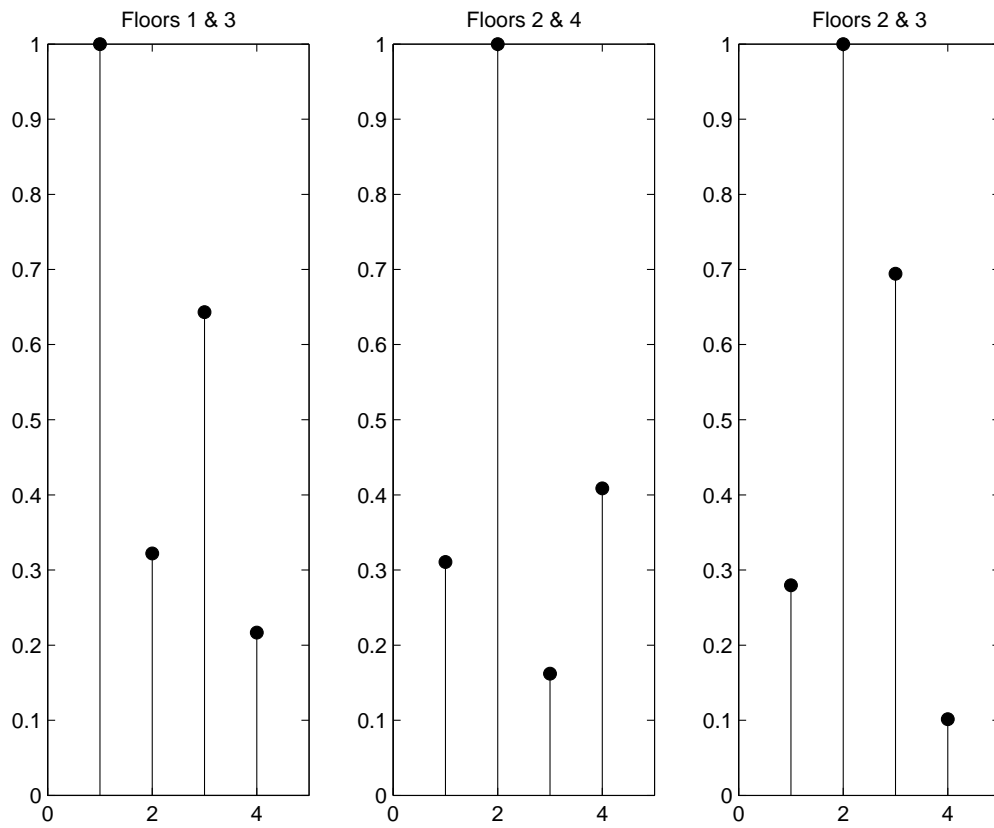


Figure 6.8: Damage detection using the rotational flexibility matrix approach for the ASCE benchmark structure, damage in two stories.

However, the normalization of mode shapes seemed to affect the flexibility method more than the rotational flexibility method. In the case of rotational flexibility matrix, damage is indicated by the large values of the damage indices. This approach is however less discriminant when multiple damages are present. To clearly identify multiple damages a different damage index needs to be defined.

Chapter 7

Summary and Concluding Remarks

7.1 Summary

The damage in a structural element is directly related to its stiffness or flexibility characteristics. However, the direct estimation of these parameters from the measured response data is rather difficult. On the other hand, methods are available for estimation of the modal parameters from measured dynamic response. This study examines the use of four different methods that have been suggested for calculating the modal parameters from the measured response. These modal parameters are then used to identify the presence and location of the damage. The study also examines the methods that can be used for the identification of the time of occurrence of the damage. Based on the numerical study conducted, the main conclusions that can be drawn about modal parameter estimation, detection of damage instant and damage location are presented in this chapter.

In chapters 2 through 5, basic details of four different modal parameter estimation methods with numerical results associated with each method were presented. The effectiveness and problems associated with each of these methods were examined for several structures excited at their base by earthquake motions. Different cases of measured structural responses with and without measurement noise were considered. The conclusions specific to a particular method are provided in the chapter where it is discussed. In the

following, the summary of the main conclusions for each of these four methods is presented.

Concluding Remarks on Modal Parameter Estimation Methods

1. Wavelet analysis for modal parameter estimation

Based on the study conducted on this method it was observed that the continuous wavelet transform can be used for the estimation of modal parameters from the measured response. However, if the contribution of a particular mode in the response is not significant, either because of the type of response being measured or because of high modal damping, then the mode shape parameter corresponding to that mode cannot be extracted. The high damping and the presence of noise in the data make it difficult to extract modal parameters. Some mother wavelets also have parameters that can be adjusted with advantage to separate different modal components from a measured response.

2. Empirical mode decomposition and Hilbert Huang transform (EMD and HHT) method for modal parameter estimation

The method of EMD and HHT can also be used for modal parameter estimation. But for separating the modal components special filtering is required, which largely affects the numerical results. The basic formulas required for calculating the modal parameters in this approach are very similar to those used in the wavelet approach. In this study, it was found difficult to use the method in several cases. The method was found to be more sensitive to the presence of noise than the wavelet approach.

3. Parametric models for modal parameter estimation

In absence of noise in the data, the method provides the most accurate results even for large systems and high damping. The efficiency of the method, however, deteriorates if any noise is present, but one can still use this method more effectively than other methods. The noise

corrupted data require that a higher order model be used for the parameter estimation. The higher order models introduce spurious poles, but methods are available for identifying at least the first few modes even in the presence of spurious poles. This method can be more easily programmed than other methods with least intervention from an analyst.

4. The peak-picking method

This method is perhaps the oldest of all mode identification methods. It is primarily based on the fact that the frequency response function of a structure will usually have peaks at the frequency of the dominant modes contributing to the response. The locations of these peaks identify the modal frequencies, and their values can be used for calculating the mode shapes. The modal damping estimations are, however, not very reliable. For the example problems considered in this study, this method was able to identify the frequencies and mode shapes in all cases considered.

The time of Occurrence of a Damage

The numerical studies were also conducted to identify the time of occurrence of a damage in a structural element. It was observed that both the discrete wavelet transform (also continuous wavelet transform) and the EMD-HHT method can be effectively used for detecting the time of occurrence of damage. But in the case of EMD, prior knowledge of the intermittency frequency seems necessary which is used as a cutoff frequency for the high-pass filter. With that knowledge, in some cases, the filtering can be applied directly on the signal instead of first calculating the IMF. In comparison to DWT, once a wavelet is selected it was found to work for all cases of damage considered.

Identification of Damage Location

After calculating the modal parameters, they were then used for damage location. Since only a first few modes can usually be calculated by any of the above methods, it was noted that a direct calculation of stiffness for damage identification and location is not possible, and one must rather use the flex-

ibility matrix which can be more accurately defined in terms of only a first few modes. To identify the location of a damage, the two flexibility-based methods, one based on the flexibility matrix approach and the other based on the rotational flexibility matrix approach were studied. It was observed that the location of the damage can be identified by either the use of the flexibility or the rotational flexibility matrix. However, the flexibility-based method requires the mode shape matrix to be mass normalized, whereas rotational flexibility-based method does not need such normalization. However, to make better use of the rotational flexibility method it was found that proper damage index needs to be defined.

7.2 Future Studies

The development of methods for accurate identification of modal parameters is quite important as they are, indeed, very good indicators of the structural condition. A large number of research studies have been conducted to develop accurate modal identification methods, but the perfect reliable approach is yet to be developed. The methods studied in this study do seem to give satisfactory results but they have been observed to have their own limitations even in simulated numerical studies. Accurate estimation of parameters from noisy data still seems to be an unsolved problem, especially from real recorded data on structures. It is, therefore, quite necessary that the applicability of various methods be examined on real data recorded in laboratory experiments as well as in the field on real structures; that is, an experimental verification of any proposed identification approach is an absolute necessity before it can be applied in practice. Such a study will also bring out any practical considerations that one might face in the real life implementation of these methods.

Bibliography

- [Addison and Addison, 2002] Addison, P. S., and Addison, N. (2002), The Illustrated Wavelet Transform Handbook, *Institute of Physics Publishing*
- [Bendat and Piersol, 1993] Bendat, J. S., and Piersol, A. G. (1993), Engineering Applications of correlation and spectral analysis, *John Wiley & Sons, Inc.*
- [Bisht and Singh, 2004] Bisht, S. S. and Singh, M. P. (2004), “Wavelet transform and Hilbert Huang transform methods for system identification: Similarities and Differences” *Proc. of Int. Sym. on Network and Center-Based Res. for Smart Structures Tech. and Earthquake Eng.*
- [Braun and Feldman, 1997] Braun, S. and Feldman M. (1997), “Time-frequency characteristics of non-linear system”, *Mechanical Systems and Signal Processing*, 11, 4, 611-620.
- [Chang and Chen, 2003] Chang, C. C., and Chen, L. W. (2003), “Vibration damage detection of a Timoshenko beam by spatial wavelet based approach”, *Applied Acoustics*, 64, 1217-1240.
- [Chang and Chen, 2005] Chang, C. C., and Chen, L. W. (2005), “Detection of the location and size of cracks in the multiple cracked beam by spatial wavelet based approach”, *Mechanical Systems and Signal Processing*, 19, 139-155.
- [Demarchi and Craig, 2003] Demarchi, J. A. and Craig, K. C. (2003), “Comments on ‘Natural frequencies and Damping Identification using wavelet transform: Application to real data’ ”, *Mechanical Systems and Signal Processing*, 17, 2, 483-488.

- [Daubechies, 1992] Daubechies, I. (1992), Ten Lectures on Wavelets, *Soc. for Industrial and Applied Math.*
- [Demetriou and Hou, 2003] Demetriou, M. A. and Hou, Z. (2003), “On-line fault/damage detection schemes for mechanical and structural systems”, *Journal of Structural control*, 10, 1-23.
- [Duan, et. al 2004] Duan, Z., Yan, G., and Ou, J. (2004) “Structural damage localization based on rotational flexibility matrix”, *Proc. of the Third Int. Conf. on Earthquake Eng., Nanjing, China* 846-850
- [Feldman, 1994a] Feldman, M. (1994), “Non-linear system vibration analysis using Hilbert transform-I Free vibration analysis method ‘FREEVIB’ ”, *Mechanical Systems and Signal Processing*, 8, 2, 119-127.
- [Feldman, 1994b] Feldman, M. (1994), “Non-linear system vibration analysis using Hilbert transform-II Forced vibration analysis method ‘FORCE-VIB’ ”, *Mechanical Systems and Signal Processing*, 8, 2, 309-318.
- [Feldman, 1997] Feldman, M. (1997), “Non-linear free vibration identification via the Hilbert transform”, *Journal of Sound and Vibration*, 208, 3, 475-489.
- [Haase and Widjajakusuma, 2003] Haase, M., and Widjajakusuma, J., (2003), “Damage identification based on ridges and maximum lines of the wavelet transform”, *International Journal of Engineering Science*, 41, 1423-1443.
- [Hamamoto, et. al., 2002] Hamamoto, T., Morita, K., and Teshigawara, M. (2002) “Story damage detection of multistory buildings using natural frequency shifts of multiple modes”, *Workshop for smart structural systems for US-Japan cooperative research programs on smart structural systems and Urban Earthquake Disaster Mitigation, Tsukuba, Japan* 221-234.
- [Hera and Hou, 2001] Hera, A., and Hou, Z. K. (2001). “Wavelet-based approach for ASCE structural health monitoring benchmark studies” *Proc., 3rd Int. Workshop on Structural Health Monitoring*, Stanford Univ., Stanford, Calif.

- [Hera and Hou, 2004] Hera, A., and Hou, Z. (2004), “Application of wavelet approach for ASCE structural health monitoring benchmark studies”, *Journal of Engineering Mechanics*, 130, 1, 96-104.
- [Huang, *et. al.*, 1998] Huang, N. E., Shen, Z., Long, S. R., Wu, M. C., Shih, H. H., Zheng, Q., Yen, N. C., Tung, C. C., and Liu, H. H. (1998), “The empirical model decomposition and the Hilbert spectrum for nonlinear and non-stationary time series analysis”, *Proc. R. Soc. Lond. A*, 454, 903-995.
- [Johnson, *et. al.*, 2000] Johnson, E. A., Lam, H. F., Katafygiotis, L. S., and Beck J. L. (2000) “A Benchmark problem for Structural Health Monitoring and Damage Detection”, *Proc., 14th ASCE Engineering Mechanics Conference*
- [Lardies and Gouttebroze, 2002] Lardies, J. and Gouttebroze, S. (2002), “Identification of modal parameters using the wavelet transform”, *International Journal of Mechanical Sciences*, 44, 2263-2283.
- [Le and Argoul, 2004] Le, T., and Argoul, P. (2004) “Continuous wavelet transform for modal identification using free decay response” *Journal of Sound and Vibration*, 127,1-2,73-100.
- [Ljung, 1987] Ljung, L., (1987) *System Identification: Theory for User*, Prentics-Hall Information And System Sciences Series, Prentics-Hall.
- [Ljung, 1994] Ljung, L., and Glad, T. (1994) *Modeling of Dynamic Systems*, Prentics-Hall Information And System Sciences Series, Prentics-Hall.
- [Ljung, 2002] Ljung, L. *System Identification Toolbox User’s Guide, Version 5*, The MathWorks, Inc.
- [Lu, *et. al.* 2002] Lu, Q., Ren G., and Zhao Y. (2002) “Multiple damage location with flexibility curvature and relative frequency change for beam structures”, *Journal of Sound and Vibrations* 253(5),1101-1114
- [Lu and Hsu, 2002] Lu, Chung-Jen, and Hsu, Yu-Tsun (2002), “Vibration analysis of an inhomogeneous string for damage detection by wavelet transform”, *International Journal of Mechanical Sciences*, 44, 745-754.

- [Masuda, *et. al.* 2002] Masuda A., Noori M., Sone A., and Hashimoto, Y. (2002), “Wavelet-bases health monitoring of randomly excited structures”, *15th ASCE Engineering Mechanics Conference*.
- [Melhem and Kim, 2003] Melhem, H. and Kim, H. (2003), “Damage detection in concrete by Fourier and wavelet analyses”, *Journal of Engineering Mechanics*, 129, 5, 571-577.
- [Misiti] Misiti, M., Misiti, Y., Oppenheim, G., and Poggi, J. M., Wavelet Toolbox Users Guide, Version 2, The MathWorks, Inc.
- [Mita and Hagiwara, 2002] Mita, A., and Hagiwara H. (2002) “Damage detection using support vector machine on modal frequency patterns for a building structure”, *Workshop for smart structural systems for US-Japan cooperative research programs on smart structural systems and Urban Earthquake Disaster Mitigation, Tsukuba, Japan* 333-340
- [Mita, 2004] Mita, A. (2004) “Support vector machine for structural health monitoring”, *Third China-Japan-US Sym. on Str. Health Monitoring and Control and Fourth Chinese National Conference on Structural Control, Dalian, China* 63-67
- [mlab] www.mathworks.com
- [Morita *at. al.*, 2001] Morita, K., Teshigawara, M., Isoda, H., Hamamoto, T., and Mita, A. (2001), “Damage detection of five-story steel frame with simulated damages”, *Advanced Nondestructive Evaluation for Structural and Biological Health Monitoring, Proceedings of SPIE*, 4335, 106-114.
- [Okafor and Dutta, 2000] Okafor, A.C. and Dutta, A. (2000), “Structural damage detection in beams by wavelet transforms”, *Smart Mater. Struct.*, 9, 906-917.
- [Ovanesova and Suarez 2004] Ovanesova, A. V. and Suarez, L. E. (2004), “Application of wavelet transform to damage detection in frame structures”, *Engineering Structures*, 26, 39-49.
- [Pandey and Biswas, 1994] Pandey, A. K., and Biswas M. (1994) “Damage detection in structures using changes in flexibility”, *Journal of Sound and Vibrations* 169, 1, 3-17.

- [Pandey and Biswas, 1995] Pandey, A. K., and Biswas M. (1995) “Experimental verification of flexibility difference method for locating damage in structures”, *Journal of Sound and Vibrations* 184, 2, 311-328.
- [Patsias and Staszewski, 2002] Patsias, S. and Staszewski, W. J. (2002), “Damage detection using optical measurements and wavelets”, *Structural Health Monitoring*, 1, 1.
- [Peeters, 2000] Peeters, B. (2000) “System identification and damage detection in civil engineering”, Ph.D. dissertation, Structural Mechanics, Civil Engineering Department, K.U.Leuven, Belgium.
- [Percival and Walden 2000] Percival, D. B., and Walden, A. T. (2000), Wavelet methods for time series analysis, *Cambridge University Press*
- [Pi and Mickleborough, 1989a] Pi, Y. L. and Mickleborough, N. C. (1989), “Modal identification of vibrating structures using ARMA model”, *Journal of Engineering Mechanics*, 115, 10, 2232-2249.
- [Pi and Mickleborough, 1989b] Pi, Y. L. and Mickleborough, N. C. (1989), “Modal identification of a vibrating structure in the time domain”, *Computer and Structures*, 32, 5, 1105-1115.
- [Pi and Mickleborough, 1989c] Mickleborough, N. C., and Pi, Y. L. (1989), “Modal identification using Z-transform”, *International Journal for Numerical Methods in Engineering*, 28, 2307-2321.
- [Poularikas, 1996] Poularikas, A. D. ed. (1996), The transform and application handbook, *CRC Press*
- [Ruzzene, 1997] Ruzzene, M., Fasana, A., Garibaldi, L., and Piombo, B. (1997), “Natural frequency and damping identification using wavelet transform: Application to real data”, *Mechanical Systems and Signal Processing*, 11, 2, 207-218.
- [Singh and Bisht, 2004] Singh, M. P. and Bisht, S. S. (2004), “A review of system identification methods for civil structures”, *Proc. of Third Int. Conf. on Earthquake Eng.*
- [Staszewski, 1997] Staszewski, W. J. (1997) “Identification of damping in MDOF systems using time-scale decomposition”, *Journal of Sound and Vibration*, 203, 2, 283-305

- [Steiglitz and McBride, 1965] Steiglitz, K., and McBride, L. E., (1965) “A technique for the identification of linear systems”, *IEEE Transaction on Automatic Control*, 461-464
- [Strang and Nguyen, 1996] Strang, G., and Nguyen, T. (1996), Wavelets and filter banks, *Wellesley-Cambridge Press*
- [Wang and Deng, 1999] Wang, Q., and Deng, X. (1999), “Damage detection with spatial wavelets”, *International Journal of Solids and Structures*, 36, 3443-3468.
- [Xu and Chen, 2004] Xu, Y. L., and Chen, J. (2004), “Structural damage detection using empirical mode decomposition: Experimental investigation”, *Journal of Engineering Mechanics*, 130, 11, 1279-1288.
- [Xu, et. al., 2003] Xu, Y. L., Chen, S. W., and Zhang, R. C. (2003), “Modal identification of Di Wang building under typhoon York using the Hilbert-Huang transform method”, *The structural design of tall and special buildings*, 12, 21-47.
- [Yang, et. al., 2003a] Yang, J. N., Lei, Y., Pan, S., and Huang, N. (2003), “System identification of linear structures based on Hilbert-Huang spectral analysis. Part 1: normal modes”, *Earthquake Eng. and Structural Dyanamics*, 32, 1443-1467.
- [Yang, et. al., 2003b] Yang, J. N., Lei, Y., Pan, S., and Huang, N. (2003), “System identification of linear structures based on Hilbert-Huang spectral analysis. Part 2: complex modes”, *Earthquake Eng. and Structural Dyanamics*, 32, 1533-1554.
- [Yang, et. al., 2004a] Yang, J. N., Lei, Y., Lin, S., and Huang, N. (2004), “Identification of natural frequencies and damping of in situ tall buildings using ambient wind vibration data”, *Journal of Engineering Mechanics*, 130, 5, 570-577.
- [Yang, et. al., 2004b] Yang, J. N., Lei, Y., Lin, S., and Huang, N. (2004), “Hilbert-Huang based approach for structural damage detection”, *Journal of Engineering Mechanics*, 130, 1, 85-95.

- [Zhang, *et. al.*, 2001] Zhang, R. R., Ma, S., Safak, E., and Hartzell, S. (2001), "Hilbert-Huang transform analysis of dynamic and earthquake motion recordings", *Journal of Engineering Mechanics*, 129, 8, 861-875.